AN ABSTRACT OF THE DISSERTATION OF

Yunteng He for the degree of Doctor of Philosophy in Chemistry presented on May 30, 2017.

Title: Electron Diffraction of Molecules in Superfluid Helium Droplets

Abstract approved:

_____

Wei Kong

In this dissertation, I describe the experimental investigation in electron diffraction of molecules in superfluid helium droplets. The project is part of an overall scheme called ‘single molecule serial electron diffraction imaging’ (SS-EDI), with the ultimate goal of building an apparatus to determine atomic structures from oriented macromolecules. In SS-EDI, protein ions are doped in helium droplets and the doped droplets are then oriented by an elliptically polarized laser and exposed to a coherent electron beam for diffraction. The specific goal of my project is to explore the feasibility for electron diffraction of molecules in helium droplets. I started by installing several diagnostic components and systematically characterizing the behavior of the helium droplet beam, including its timing profile, size distribution, and doping statistics. I then moved on to electron diffraction of molecules in helium droplets. In the work on CBr_4, the background issue from helium atoms was solved by increasing the doping path length or pressure of gaseous CBr_4. In the experiment of ferrocene, the velocity slip of our pulsed droplet beam has been utilized to separate

different sized droplets and to achieve efficient single doping in one droplet. The resulting success testifies to the capability of size control of our experiment. In the work of I_2, the investigation was further expanded to different sized droplets containing different sized iodine clusters. From this study, we observed for the first time halogen bonded iodine clusters and bi-layer iodine nanocrystals.

The work in this dissertation represents a major step in demonstrating the working principle of the overall idea of SS-EDI. The successes of these efforts imply that by embedding the sample in a superfluid helium droplet, the structurally relevant diffraction information of the sample can still be retrieved, as long as one can control the amount of helium surrounding the sample.

Electron Diffraction of Molecules in Superfluid Helium Droplets

by
Yunteng He

A DISSERTATION

submitted to

Oregon State University

in partial fulfillment of
the requirements for the
degree of

Doctor of Philosophy

Presented May 30, 2017
Commencement June 2017

Doctor of Philosophy dissertation of Yunteng He presented on May 30, 2017

APPROVED:

Major Professor, representing Chemistry

Chair of the Department of Chemistry

Dean of the Graduate School

I understand that my dissertation will become part of the permanent collection of Oregon State University libraries. My signature below authorizes release of my dissertation to any reader upon request.

Yunteng He, Author

ACKNOWLEDGEMENTS

During the past six years in my pursuit of a Ph.D. in chemistry, many people have helped me in this difficult and yet rewarding journey.

Firstly, I would like to express my sincere appreciation to my advisor Professor Wei Kong. I have achieved incredible self-improvement during the six years learning from her, in the aspects of not only the knowledge, but also her integrity and industriousness. She has given me numerous valuable suggestions in the project and in the write-up of this thesis. Her advice on my research and my life has been invaluable.

I also would like to thank Dr. Jie Zhang. She has helped me in familiarizing with the lab, and in guiding me for research and problem solving. My special thanks also go to my lab-mates: Dr. Collin Harthcock, Dr. Lei Chen and Mr. Andrew Oswalt. They have always been willing to help. My special thanks are to Mr. Bill Freund, who have helped me in designing complicated components and in making functional electronic circuits. I would also like to thank Mr. Larry Nelson who have supported my project with many exquisite homemade parts.

I would also like to thank my thesis committee: Dr. Joseph Beckman, Dr. Valery Voinov, Dr. Michelle Dolgos and Dr. John Simonsen for their insightful comments and advice.

Finally, I would like to acknowledge the support of my family. Without their encouragement, it is impossible for me to finish my Ph.D. project.

CONTRIBUTION OF AUTHORS

Dr. Jie Zhang and Ms. Lei Lei assisted with data collection and analysis. Mr. Bill Freund helped design parts of the experimental setup.

TABLE OF CONTENTS

TABLE OF CONTENTS (Continued)

Page

TABLE OF CONTENTS (Continued)

TABLE OF CONTENTS (Continued)

TABLE OF CONTENTS (Continued)

LIST OF FIGURES

Figure Page

LIST OF FIGURES (Continued)

Figure Page

LIST OF FIGURES (Continued)

Figure Page

LIST OF FIGURES (Continued)

Figure Page

LIST OF TABLES

Chapter 1 Introduction

1.1 Motivation

Knowing the structures of proteins is the first step in understanding biological reactions and in designing efficient drugs. For more than half a century, X-ray crystallography has been the most prolific method, contributing to nearly 90% of the structures deposited in the protein databank (PDB). However, the entire PDB with ~77,000 structures only amounts to ~10% of the sequenced proteins. Moreover, a portion of the remaining proteins are membrane proteins, and they are notoriously difficult to crystallize and are therefore extremely challenging for structure determination. Yet these proteins amount to 70% of today's drug targets.

New structural tools are in demand to overcome limitations of existing methods. While purification and crystallization are the major bottlenecks in crystallography,[1] other methods suffer significant limitations to fill in the gap. The spectroscopic technique nuclear magnetic resonance (NMR) offers structural information in near physiological conditions, but it has limited sensitivity and suffers from spectral congestion.[2] Cryoelectron microscopy (cryo-EM) has been gaining popularity in structural biology over the past decade,[3] but major problems in cryo-EM are radiation damage and angular assignment of images from individual particles.[4] In addition, cryo-EM obtains three-dimensional (3D) structures from sampling 2D projections, and for anisotropic proteins where preferred orientations are common on a TEM grid, incomplete sampling of all orientations and effect of supporting substrates can both pose problems.

1.2 Possible solutions

The need for a fundamentally new approach in solving the atomic structures of proteins has prompted many ingenious ideas in the field of structure biology.[5,6] In 2004, Spence and Doak proposed a new method named ‘single molecule diffraction’, with the ultimate promise of solving the crystallization problem in crystallography.[5] The overall idea is shown in Fig. 1.1. First, protein molecules surrounded with a thin water layer are injected into vacuum and rapidly cooled by evaporation. The surrounding water freezes to form a vitreous ice jacket, entrapping the conformation of the proteins. Then a polarized laser beam aligns the molecules due to induced dipole moment. Diffraction signals are accumulated for many such aligned molecules until a good signal-to-noise ratio (S/N) is achieved. Then the polarization of the laser is rotated and diffraction is recorded from a different angle. A 3D molecular image is obtained by phase retrieval from many different 2D projections via the oversampling method. Although some aspects of this proposal such as laser alignment of cooled molecules in vacuum[7], electrospray ionization of proteins[8], and electron diffraction of molecules[9], have been demonstrated separately, an experimental demonstration of the combined approach is still yet to come.

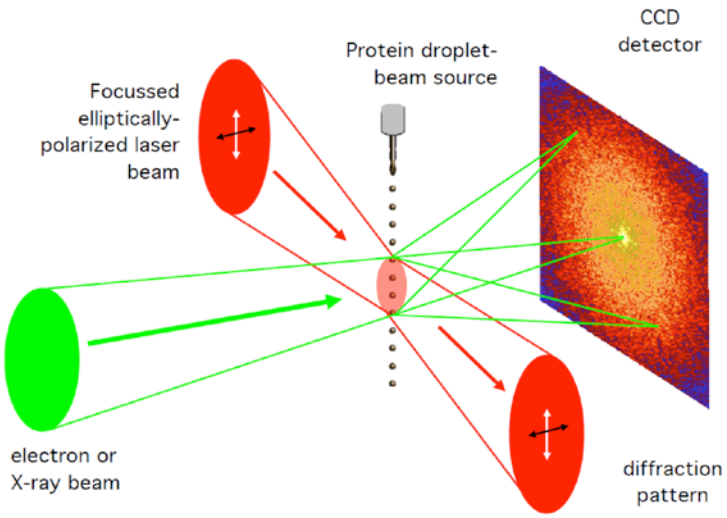

Fig. 1.1 Single molecule diffraction proposed by Spence and Doak, adapted from Phys. Rev. Lett. 92, 198102 (2004).

Another relevant approach is called ‘diffract and destroy’, which is also known as ‘Serial Femtosecond Crystallography (SFX)’.[10] Fig. 1.2 is a schematic depiction of this approach. At the centre of this method is an intense ultrashort x-ray pulse, available from new generation free electron lasers. The basic hypothesis of this approach is that sufficient diffraction data can be obtained from one single molecule in one radiation pulse before radiation damage takes effect. As shown in Fig. 1.2, many individual diffraction patterns are recorded from single particles traveling from top to bottom. Different diffraction images from random and unknown oriented molecules are then sorted and combined in a process similar to that in cryo-EM.

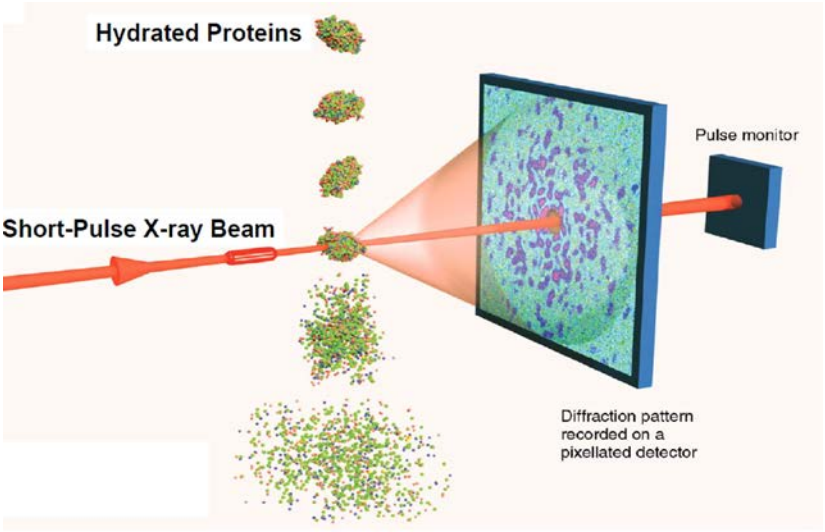

Fig. 1.2 The Diffract and Destroy method, adapted from Science 316(5830):1444-1448

The above method requires extremely strong diffraction light sources and extremely low noise detectors, and the latter condition is still yet to be fulfilled in reality. A moderation of the above experimental conditions can be achieved using single nanocrystals instead of single molecules, and experimental success in using a series of single nanocrystals in intense ultrashort x-ray pulses from free-electron lasers have been reported. In December 2009, the first SFX experiment was carried out utilizing the X-ray pulses at the Linac Coherent Light Source (LCLS) by the Chapman group, with nanocrystals of photosystem I (PSI). Tens of thousands of diffraction patterns were collected, which allowed for the assignment of the Bragg peaks and determination of the PSI structure. This experiment offers the proof of concept for SFX[11]. In a more recent study, the structure of Trypanosoma brucei Cathepsin B together with its inhibitory propeptide was determined at LCLS,[12] and this represents the first time that an XFEL was used to solve an unknown protein structure. Fig. 1.3 is a gallery illustrating the selected protein structures solved with XFELs to date,[13] including photosystem I (3PCQ), FABP3 (3WXQ), purple bacterial reaction center

(4CAS), lysozyme (4ET8), cathepsin B (4HWY), 5-HT2B (4NC3), photosystem II (4PBU), δ-opiod receptor (4RWD), smoothened receptor (4O9R), Cry3A (4QX0), CPV17 polyhedron (4S1K), diacylglycerol kinase (4UYO), xylose isomerase (4W4Q), photoactive yellow protein (4WL9), SR Ca2+-ATPase (4XOU), angiotensin II receptor (4YAY), phycocyanin (4Z8K), luciferin-regenerating enzyme (5D9B), C-phycocyanin (4ZIZ), rhodopsin-arrestin complex (4ZWJ).

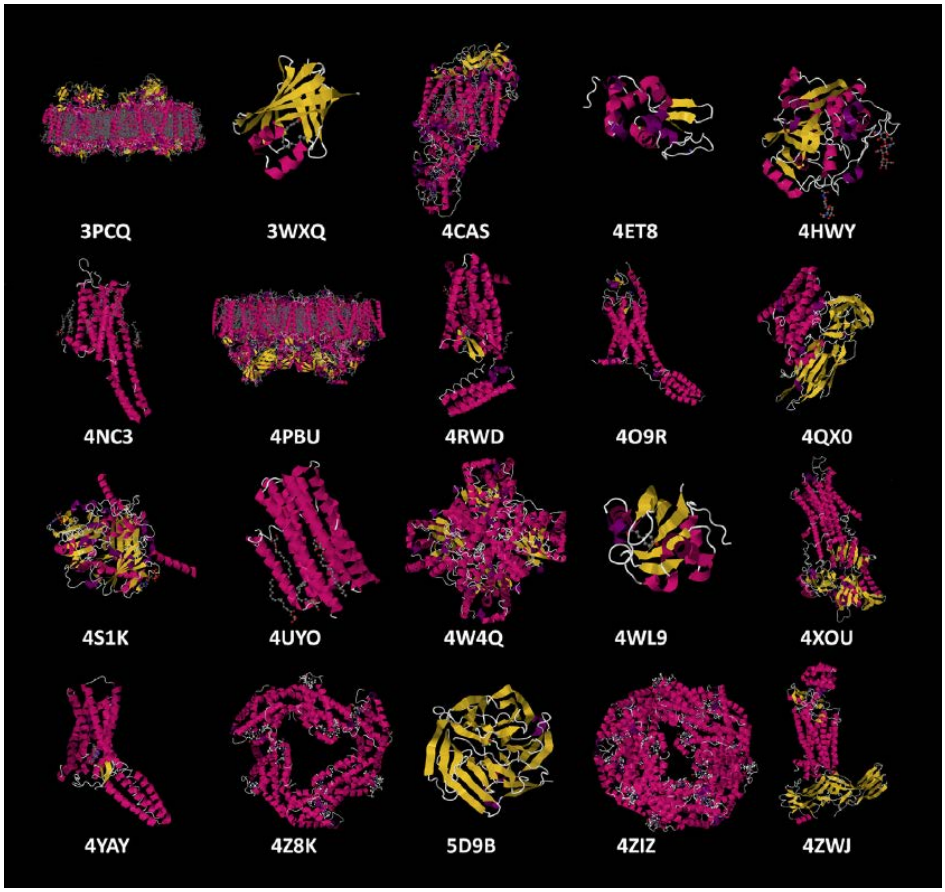

Fig. 1.3. Selected structures solved using XFELs, adapted from Arch. Biochem. Biophys. 602 (2016) 32

Nevertheless, several problems still remain with SFX. Orientation assignment of a noisy 2D projection is still a challenge. In addition, with the photon flux of current XFELs, the ultimate goal of structural elucidation of macromolecules without the need of crystallization, meaning single molecules, is still out of reach. Moreover, to "out-run" radiation damage, the duration of the X-ray pulse has to be further shortened by more than one order of magnitude, to less than 10 fs or preferably 1 fs.

Our group has developed an approach called 'single molecule serial electron diffraction imaging' (SS-EDI)[14]. Although our basic idea is similar to the single molecule diffraction method proposed by Spence and Doak,[5] several major differences exist. Instead of using a hydrated droplet beam, we rely on electrospray ionization for sample delivery. The chosen ions are then embedded in superfluid helium droplets for rapid cooling to 0.37 K before alignment by a laser field. Electron diffraction patterns from individual protein doped droplets all oriented in the same direction are accumulated. High quality diffraction patterns from different orientations are obtained under different polarization settings of the alignment laser. Using the oversampling method for iterative phase retrieval, electron density maps of the diffraction molecules can then be generated for structure determination.

Substrate free sample orientation and reorientation, i. e., a molecular goniometer, is of key importance and challenge to SS-EDI. Our solution to this problem involves embedding the protein ions in superfluid helium droplets and using a polarized laser for orientation. To a large degree, experimental development of SS-EDI starts with

the molecular goniometer, and the success of the molecular goniometer can be directly transferred to SFX and even to cryo-EM.

1.3 Molecular goniometer - field alignment and orientation

The idea to the sample orientation problem comes from the community of gas phase chemical physics. In 1987, Herschbach proposed the idea of orienting polar molecules from a molecular beam using a strong static electric field[15], and shortly after, the same group expanded the idea to laser fields and magnetic fields.[16,17] As shown in Fig. 1.4 using diatomic molecules as an example, alignment can be achieved using a fast oscillating laser field, with the molecular axes parallel to each other but without any preference for the head over tail. Alternatively, orientation can be achieved with a static electric field by controlling both the molecular axis and one polar end of the molecule, with “all heads up”.

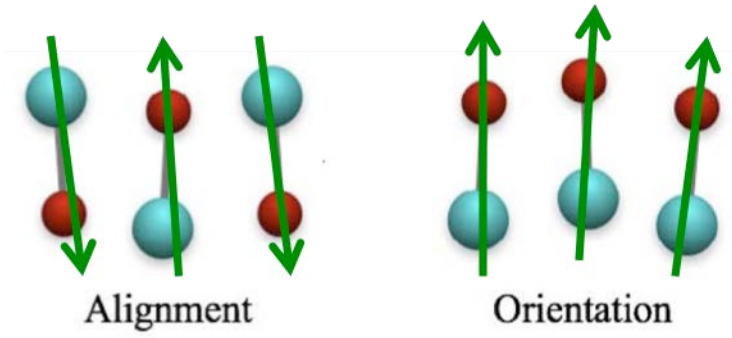

Fig. 1.4 Alignment and orientation of molecules.

1.3.1 Orientation via static electric fields

Orientation with static electric fields requires a large permanent dipole moment. The net effect is determined by the ratio between the interaction energy and the thermal rotational energy of the molecule: $\mu E / k_B T$, where μ is the permanent dipole moment, E is the electric field, and T is the rotational temperature of the molecular sample. For

typical room temperature molecules with permanent dipoles less than a few Debyes, the required field strength is over the breaking point of air, on the order of 100 kV/cm. With the advent of supersonic molecular beams, however, the rotational temperature of gaseous molecules can be lowered down to a few Kelvin, and the required field strength becomes practical. Herschbach et al first came to this realization and nicknamed this method 'brute force orientation'.[15]

Since the proposal,[15] "brute force orientation" has been adopted by several groups around the world for spectroscopic and reaction dynamics studies in the gas phase. Loesch et al have used this method for orienting CH_3I to examine steric effects in the reaction $K + CH_3I \rightarrow KI + CH_3$.[18] Herschbach et al have reported laser induced fluorescence of ICI in fields up to 20 kV/cm.[19] They have confirmed that the lowest rotational states are becoming pendular at such field strengths. One of the first experimental demonstrations of pendular states was performed by Miller's group from infrared spectroscopy of $(HCN)_3$: the spectrum undergoes a dramatic evolution from that of a free rotor at zero electric field to that indicative of a pendulum bound by a large electric field.[20] Our group has quantified the effect of the static orientation method through the $\pi^* \leftarrow$ n transition in pyrimidine and pyridazine, and used it for studies of photodissociation of molecules such as ICN[21,22], BrCN[23,24], t-butyl nitrite[25], a series of nitroaromatics[26-28], and derivatives of nucleic acid bases[29]. We have further developed the gas phase linear dichorism technique capable of measuring directions of transition dipoles and determination of molecular conformations.[30,31]

The advantages of this technique include its simplicity and its orientational ability, as compared with only alignment with laser fields. However, its requirements on the size of the permanent dipole and the rotational temperature make it of limited application. Many chemically interesting molecules have limited vapor pressures, and even when they can be vaporized using heat or laser desorption, the resulting rotational temperature from a supersonic molecular beam is typically over 10 K, too high for effective orientation. The method is also problematic when dealing with charged species.

1.3.2 Laser alignment/orientation

Optical field induced alignment is based on the anisotropic polarizability of a molecular system through the induced dipole moment. The electromagnetic field of a non-resonant laser field oscillates at the optical frequency, driving the electronic cloud and thereby the entire molecular frame along the direction of the electric field. While the head and tail of a molecule cannot flip fast enough to keep up with the fast oscillation of the electric field, the electronic cloud – the induced dipole – can at least align the predominant polarization axis parallel to the field. Hence a laser field in its second order interaction with the electronic cloud of a molecule can only achieve molecular alignment.

The spatial orientation of a molecule is determined by three Euler angles (θ, φ, and χ), as shown in Fig. 1.5. For example, a linearly polarized laser field along the space-fixed z-axis leads to 1 dimensional alignment where only θ is confined around the z-axis, while φ and χ still can wiggle around. The control of all three Euler angles can

be achieved by using an elliptically polarized laser, because of the existence of two perpendicular oscillating electric fields.

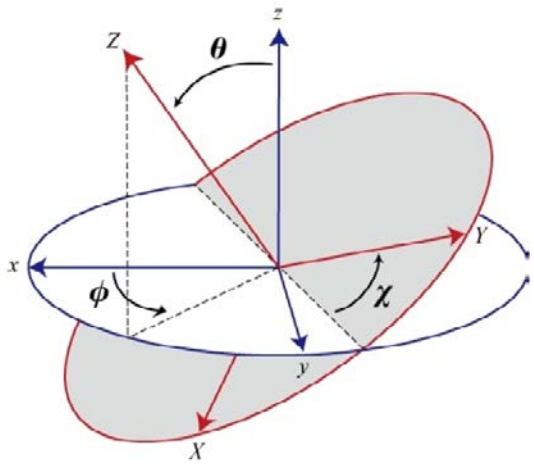

Fig. 1.5 The relative orientation between the body-fixed (X, Y, Z) and space-fixed (x, y, z) coordinate systems is specified by a set of three Euler angles (θ, φ, χ).

There are two regimes in modeling the alignment of a laser field[7]. When the rise edge of a laser pulse is much longer than the rotational period of a molecule, alignment is gradually achieved during the laser pulse and molecules return to free rotational states after the laser pulse ceases. This regime is called adiabatic alignment. In the other case, molecules are subject to an ultrashort (usually femtosecond) laser pulse, and the alignment process it is called nonadiabatic. In this case, alignment can re-occur periodically after the laser pulse ceases through the rotational echo effect.[7]

The field of laser induced molecular alignment has progressed remarkably over the past decade. Sakai et al. demonstrated controlling the alignment of I_2 molecules by a nanosecond linearly polarized infrared laser field.[32] They determined the degree of alignment by imaging the fragment ions from Coulomb explosion of the aligned

molecules with a femtosecond laser. The same group has demonstrated molecular alignment of other molecules such as ICl, CS_2, C_6H_5I, and CH_3I[33]. Larsen et al. have further demonstrated 3D alignment of 3,4-dibromothiophene molecules with a nonresonant elliptically polarized laser field.[34]

The advantages of laser induced alignment are multifold. It is applicable to all molecules with anisotropic polarizabilities, and the degree of alignment can be much larger than what is achievable with static fields. The polarizability of a polyatomic molecule typically scales with the overall size of the molecule, hence laser induced alignment is more effective for larger sized macromolecules such as proteins than for smaller molecules.

Unfortunately, the control of molecular orientation, not just alignment, is much more difficult with a laser field than with a static field. One solution is to combine a static field with a laser field, as suggested by Friedrich and Herschbach and demonstrated by Sakai et al with OCS and 3,4- dibromothiophene.[35] Another solution is to use two different lasers and rely on the third order nonlinear polarizability. Ohmura and Nakanaga demonstrated the orientation of three iodine-containing molecules (IBr, CH_3I, and C_3H_5I) by using phase-controlled two-color laser pulses.[36]

1.3.3 Alignment and orientation in helium droplets

In either static or laser fields, the degree of alignment or orientation is determined by the ratio of the interaction energy of the field and the thermal rotational energy of the molecule. The key for effective orientational control is therefore a low rotational temperature. With the invention of superfluid helium droplets, field induced

orientation and alignment has gained tremendous advantage due to the extreme cooling effect (0.37 K) of the droplets. Furthermore, the superfluidity of the droplets and the near unity electric permittivity of helium ensure minimal interference from the droplet environment to the embedded dopant molecule. Helium droplets have a low polarizability and a high ionization potential, and hence they are transparent to the laser filed.

Stapelfeldt group has demonstrated both adiabatic and nonadiabatic alignment of molecules in helium droplets. Using a nanosecond laser, they demonstrated 1D adiabatic alignment of 1,4 diiodobenzene ($C_6H_4I_2$), iodobenzene (C_6H_5I), and methyliodide (CH_3I) doped in helium droplets[37]. The degree of alignment increases as the laser intensity is increased, similar to the results in the gas phase. Using a 450 fs laser, Stapelfeldt group have also reported nonadiabatic alignment of methyliodide in helium droplets[38]. The molecules reach a maximum alignment 17 – 37 ps later and return to random orientation in another ~70 ps. The time scale of the dynamics is much slower in helium droplets than that of gas phase molecules (0.1 – 3.5 ps): with a factor of ~10–170 for the time to reach the first alignment maximum. Theorists are still working on the origin of this unexpected effect of the droplet environment. With 1,4-diiodobenzene, Christiansen et al. have also shown that field-free 1D alignment in helium droplets can be significantly enhanced by using a sequence of synchronized short laser pulses.[39]

Different from alignment of isolated gas phase molecules, alignment in helium droplets is not fully captured by any existing theories. Overall, according to Stapelfeldt: (1) in the adiabatic regime, similar to the case of isolated molecules,

molecules doped in helium droplets are capable of following the slow rise of the laser field and can achieve a very high degree of alignment; (2) in the nonadiabatic regime, alignment is much slower than that of isolated molecules.

1.3.4 Other alignment/orientation methods

Several other methods of achieving molecular alignment have also been reported in the literature. [40,41] Most of these methods are specific to the molecular species and lack general applicability to other systems, and none has offered the capability of 3D alignment. For example, photodissociation selectively removes a group of molecules aligned with their transition dipoles parallel to the polarization direction of the excitation laser[40]. Greeley et al ionized NO with resonantly enhanced multiphoton ionization (REMPI) and prepared an aligned distribution of NO^+.[42]

1.3.5 Concluding remarks

Based on the advantages and limitations of different field induced alignment and orientation methods, we have decided that the best approach is to use an elliptically polarized laser for alignment, a static electric field for orientation, and superfluid helium droplets for cooling of the sample molecules. The extremely low temperature of superfluid helium droplets results in more effective orientation, by almost three orders of magnitude than that of a room temperature sample, and two orders of magnitude than that of a supersonic molecular beam. In addition, the low temperature significantly reduces the vibrational movement of the scattering atoms, thereby enhancing the scattering intensity and spatial resolution. Superfluid helium does not interact with the embedded macromolecules, and it cools the embedded macromolecule ions in microseconds or less. The fast cooling rate and the

maintenance of the low temperature both help protect ions from denaturation and radiation damage. Although the introduction of a helium jacket surrounding the sample molecules will inevitably introduce a scattering background, with sufficient care of the droplet size, we might be able to overcome this issue.

1.4 Strategic approach

The overall experimental setup of SS-EDI is shown in Fig 1.6. Protein ions (red balls) are introduced into the vacuum system from solution using electrospray ionization, and are then doped in superfluid helium droplets (blue balls) for rapid cooling. After passing through the controlling electrodes, the doped droplets are directed into the diffraction chamber where they encounter a pulsed electric field and an elliptically polarized infrared laser for orientation and alignment, and a pulsed coherent high-energy electron beam for diffraction. Electron diffraction patterns from individual protein doped droplets all oriented in the same direction are accumulated as the experiment runs at 10 Hz. The shown diffraction image in Fig. 1.6 is calculated from Cu,Zn SOD1 in one orientation at an electron wavelength of 0.06 Å (40 keV). From a succession of images obtained under different polarization settings of the alignment laser, sufficient information for phase retrieval and structure determination can be obtained.

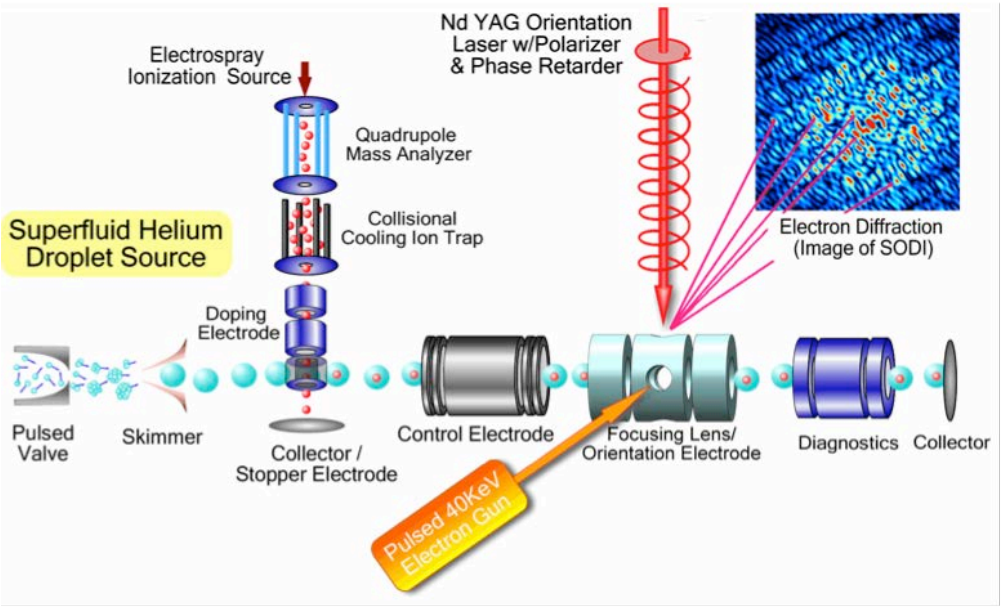

Fig. 1.6 Overall experimental setup for SS-EDI.

Different from Spence and Doak's method using continuous light sources and sample beams[5], we choose to use three pulsed beams for SS-EDI. First, a pulsed helium droplet source can have a factor of 100 higher flux and can have one order of magnitude larger droplets in size than those from a continuous droplet beam at the same source pressure and temperature.[43] Second, a pulsed alignment laser can achieve a significantly higher field density than a continuous laser, which is tremendously helpful for field induced alignment. Our decision to use coherent electron beams instead of X-rays is because of the larger elastic and smaller inelastic scattering cross sections of electrons, by up to four orders of magnitude, and the easy accessibility of pulsed electron guns.

Given the overwhelming scope of this project, we have divided the task into two parallel halves, a diffraction half and a protein source half. The diffraction path aims to achieve electron diffraction of neutral molecules doped in superfluid helium droplets, and alignment of neutral molecules using a laser field. protein source path

aims to achieve doping of protein ions from an ESI source into superfluid helium droplets, and further characterization of the ion doped droplets.

This thesis work is concentrated on the diffraction half, and a more detailed experimental setup is shown in Fig. 1.8. The vacuum system has three differentially pumped chambers: the source chamber is for generating the helium droplets, the pickup chamber is for doping molecules into the droplets, and the diffraction chamber is for collecting diffraction patterns. The electron gun emits high-energy electrons at 40 keV, and the main electron beam is blocked by the Faraday cup on top of the phosphor screen. The diffracted electrons are collected on the phosphor screen, and the diffraction patterns are recorded by a camera. At this stage, no sample alignment and orientation will be attempted during diffraction.

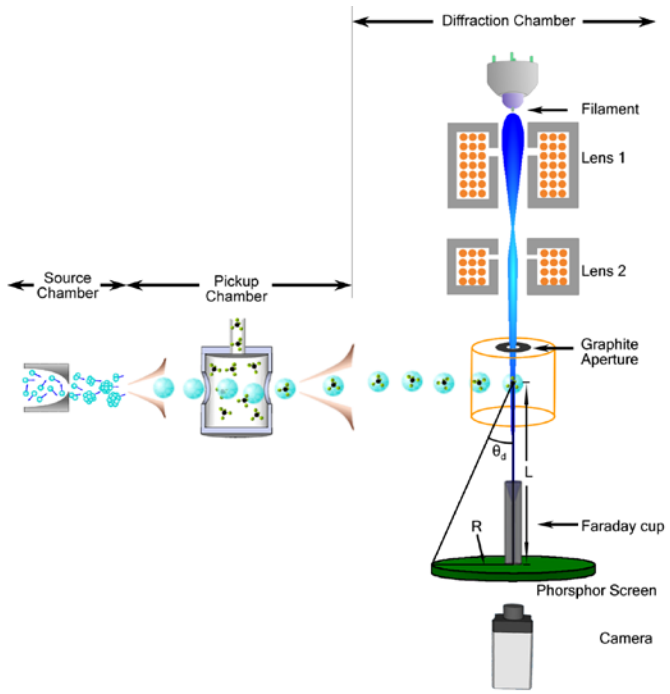

Fig 1.8 The diffraction half of the overall experiment.

1.5 Scope of this thesis

Since the publication by Spence and Doak on single molecule diffraction,[5] several major experimental successes have been reported, including entrapment of protein ions in superfluid helium droplets and field induced orientation of molecules embedded in superfluid helium droplets[38,44]. In particular, a member of our own research group, Dr. Lei Chen, has studied the doping mechanism of charged particles into superfluid helium droplets and offered a relatively straightforward method for effective doping of ions from an electrospray ionization source.[45,46] However, electron diffraction of molecules embedded in helium droplets has not been reported, and my Ph.D. project is intended to fill in this gap.

In this thesis, I will start with a detailed explanation of the experimental setup, including details on the superfluid helium droplet source (Chapter 2) and the electron gun (Chapter 3). The remaining of the thesis showcases the publications related to characterization of the experimental apparatus and results of electron diffraction. We first installed several diagnostic components in the apparatus to systematically characterize the behavior of our helium droplet beam, including its timing profile, size distribution, and doping statistics (Chapter 4, published in *Rev. Sci. Instrum.* and Chapter 5, published in *J. Chem. Phys.*). This detailed understanding of the helium droplet beam has translated into an understanding of the bottleneck in electron diffraction of molecules doped in helium droplets: undoped droplets could overwhelm the detector and prevent recording of diffraction signal from the doped sample, so a key issue is how to minimize the diffraction background from undoped droplets. In the work of electron diffraction of CBr_4, we have solved this background issue by

increasing the doping path length or pressure of dopant molecules. Although we have inadvertently doped multiple CBr_4 molecules per droplet, with the intermolecular diffraction from clusters treated appropriately, the monomer structure can still be retrieved (Chapter 6, published in *J. Chem. Phys.*). In the experiment of ferrocene, the velocity slip of our pulsed droplet beam has been utilized to separate different sized droplets and to achieve efficient single doping in one droplet, and the resulting success testifies to the capability of size control of our experiment (Chapter 7, published in *J. Chem. Phys., Cover article).* In the work of I_2, we have further expanded our investigation to different sized droplets containing different sized iodine clusters. From the diffraction images, we have for the first time observed halogen bonded iodine clusters and bi-layer structures of iodine nanocrystals (Chapter 8, published in *Angew. Chem.*).

The work in this thesis represents a major step in demonstrating the working principle of the overall idea of SS-EDI. The successes of these efforts imply that by embedding the sample in a superfluid helium droplet, one can still retrieve the structurally relevant diffraction signal of the sample, as long as one can control the amount of helium surrounding the sample. Future generations of graduate students will tackle the problem of diffraction of ions from an electrospray ionization source, and ultimately diffraction of ions aligned in a laser field.

1.6 References

1 A. Doerr, Nat Meth **3**, 961 (2006).

2 D. P. Frueh, A. C. Goodrich, S. H. Mishra, and S. R. Nichols, Curr. Opin. Struct. Biol. **23**, 734 (2013).

3 D. Elmlund and H. Elmlund, Annu. Rev. Biochem. **84**, 499 (2015).

4 R. Henderson, Proc. Natl. Acad. Sci. U. S. A. **110**, 18037 (2013).

5 J. C. H. Spence and R. B. Doak, Phys. Rev. Lett. **92**, 198102 (2004).

6 S. Boutet, L. Lomb, G. J. Williams, T. R. M. Barends, A. Aquila, R. B. Doak, U. Weierstall, D. P. Deponte, J. Steinbrener, R. L. Shoeman, M. Messerschmidt, A. Barty, T. A. White, S. Kassemeyer, R. A. Kirian, M. M. Seibert, P. A. Montanez, C. Kenney, R. Herbst, P. Hart, J. Pines, G. Haller, S. M. Gruner, H. T. Philipp, M. W. Tate, M. Hromalik, L. J. Koerner, B. N. van, J. Morse, W. Ghonsalves, D. Arnlund, M. J. Bogan, C. Caleman, R. Fromme, C. Y. Hampton, M. S. Hunter, L. Johansson, G. Katona, C. Kupitz, M. Liang, A. V. Martin, K. Nass, L. Redecke, F. Stellato, N. Timneanu, D. Wang, N. A. Zatsepin, D. Schafer, J. Defever, R. Neutze, P. Fromme, J. C. H. Spence, H. N. Chapman, and I. Schlichting, Science, 1217737 (2012).

7 H. Stapelfeldt and T. Seideman, Rev. Mod. Phys. **75**, 543 (2003).

8 N. B. Cech and C. G. Enke, Mass Spectrometry Reviews **20**, 362 (2001).

9 L. O. Brockway, Rev. Mod. Phys. **8**, 231 (1936).

10 K. J. Gaffney and H. N. Chapman, Science **316**, 1444 (2007).

11 H. N. Chapman, P. Fromme, A. Barty, T. A. White, R. A. Kirian, A. Aquila, M. S. Hunter, J. Schulz, D. P. DePonte, U. Weierstall, R. B. Doak, F. R. N. C. Maia, A. V. Martin, I. Schlichting, L. Lomb, N. Coppola, R. L. Shoeman, S. W. Epp, R. Hartmann, D. Rolles, A. Rudenko, L. Foucar, N. Kimmel, G. Weidenspointner, P. Holl, M. Liang, M. Barthelmess, C. Caleman, S. Boutet, M. J. Bogan, J. Krzywinski, C. Bostedt, S. Bajt, L. Gumprecht, B. Rudek, B. Erk, C. Schmidt, A. Hoemke, C. Reich, D. Pietschner, L. Strueder, G. Hauser, H. Gorke, J. Ullrich, S. Herrmann, G. Schaller, F. Schopper, H. Soltau, K.-U. Kuehnel, M. Messerschmidt, J. D. Bozek, S. P. Hau-Riege, M. Frank, C. Y. Hampton, R. G. Sierra, D. Starodub, G. J. Williams, J. Hajdu, N. Timneanu, M. M. Seibert, J. Andreasson, A. Rocker, O. Joensson, M. Svenda, S. Stern, K. Nass, R. Andritschke, C.-D. Schroeter, F. Krasniqi, M. Bott, K. E. Schmidt, X. Wang, I. Grotjohann, J. M. Holton, T. R. M. Barends, R. Neutze, S. Marchesini, R. Fromme, S. Schorb, D. Rupp, M. Adolph, T. Gorkhover, I. Andersson, H. Hirsemann, G. Potdevin, H. Graafsma, B. Nilsson, and J. C. H. Spence, Nature **470**, 73 (2011).

12 L. Redecke, K. Nass, D. P. DePonte, T. A. White, D. Rehders, A. Barty, F. Stellato, M. Liang, T. R. M. Barends, S. Boutet, G. J. Williams, M. Messerschmidt, M. M. Seibert, A. Aquila, D. Arnlund, S. Bajt, T. Barth, M. J. Bogan, C. Caleman, T.-C. Chao, R. B. Doak, H. Fleckenstein, M. Frank, R. Fromme, L. Galli, I. Grotjohann, M. S. Hunter, L. C. Johansson, S. Kassemeyer, G. Katona, R. A. Kirian, R. Koopmann, C. Kupitz, L. Lomb, A. V. Martin, S. Mogk, R. Neutze, R. L. Shoeman, J. Steinbrener, N. Timneanu, D. Wang, U. Weierstall, N. A. Zatsepin, J. C. H. Spence, P. Fromme, I. Schlichting, M. Duszenko, C. Betzel, and H. N. Chapman, Science **339**, 227 (2013).

13 J. M. Martin-Garcia, C. E. Conrad, J. Coe, S. Roy-Chowdhury, and P. Fromme, Arch. Biochem. Biophys. **602**, 32 (2016).

14 J. Beckman, W. Kong, V. G. Voinov, and W. M. Freund, Patent No. US20150168318A1 (2015).

15 R. B. Bernstein, D. R. Herschbach, and R. D. Levine, The Journal of Physical Chemistry **91**, 5365 (1987).

[16] B. Friedrich, D. P. Pullman, and D. R. Herschbach, The Journal of Physical Chemistry **95**, 8118 (1991).

[17] A. Slenczka, B. Friedrich, and D. Herschbach, Phys. Rev. Lett. **72**, 1806 (1994).

[18] H. J. Loesch and A. Remscheid, The Journal of Chemical Physics **93**, 4779 (1990).

[19] B. Friedrich and D. R. Herschbach, Nature **353**, 412 (1991).

[20] P. A. Block, E. J. Bohac, and R. E. Miller, Physical Review Letters **68**, 1303 (1992).

[21] K. J. Franks, H. Li, R. J. Hanson, and W. Kong, J. Phys. Chem. A **102**, 7881 (1998).

[22] H. Li, K. J. Franks, and W. Kong, Chem. Phys. Lett. **300**, 247 (1999).

[23] K. J. Franks, H. Li, S. Kuy, and W. Kong, Chem. Phys. Lett. **302**, 151 (1999).

[24] K. J. Franks, H. Li, and W. Kong, J. Chem. Phys. **111**, 1884 (1999).

[25] K. J. Castle and W. Kong, J. Chem. Phys. **112**, 10156 (2000).

[26] K. J. Castle, J. Abbott, X. Peng, and W. Kong, J. Chem. Phys. **113**, 1415 (2000).

[27] K. J. Castle, J. E. Abbott, X. Peng, and W. Kong, J. Phys. Chem. A **104**, 10419 (2000).

[28] J. E. Abbott, X. Peng, and W. Kong, J. Chem. Phys. **117**, 8670 (2002).

[29] Y. He, C. Wu, and W. Kong, J. Phys. Chem. A **107**, 5145 (2003).

[30] F. Dong and R. E. Miller, Science **298**, 1227 (2002).

[31] W. Kong, L. Pei, and J. Zhang, Int. Rev. Phys. Chem. **28**, 33 (2009).

[32] H. Sakai, C. P. Safvan, J. J. Larsen, K. M. Hilligso/e, K. Hald, and H. Stapelfeldt, The Journal of Chemical Physics **110**, 10235 (1999).

[33] J. J. Larsen, H. Sakai, C. P. Safvan, I. Wendt-Larsen, and H. Stapelfeldt, J. Chem. Phys. **111**, 7774 (1999).

[34] J. J. Larsen, K. Hald, N. Bjerre, H. Stapelfeldt, and T. Seideman, Phys. Rev. Lett. **85**, 2470 (2000).

[35] A. Goban, S. Minemoto, and H. Sakai, Phys. Rev. Lett. **101**, 013001/1 (2008).

[36] H. Ohmura and T. Nakanaga, The Journal of Chemical Physics **120**, 5176 (2004).

[37] D. Pentlehner, J. H. Nielsen, L. Christiansen, A. Slenczka, and H. Stapelfeldt, Physical Review A **87**, 063401 (2013).

[38] D. Pentlehner, J. H. Nielsen, A. Slenczka, K. Molmer, and H. Stapelfeldt, Phys. Rev. Lett. **110**, 093002 (2013).

[39] L. Christiansen, J. H. Nielsen, D. Pentlehner, J. G. Underwood, and H. Stapelfeldt, Physical Review A **92**, 053415 (2015).

[40] M. S. d. Vries, V. I. Srdanov, C. P. Hanrahan, and R. M. Martin, The Journal of Chemical Physics **78**, 5582 (1983).

[41] T. D. Hain, R. M. Moision, and T. J. Curtiss, The Journal of Chemical Physics **111**, 6797 (1999).

[42] J. N. Greeley, J. S. Martin, J. R. Morris, and D. C. Jacobs, The Journal of Chemical Physics **102**, 4996 (1995).

[43] D. Pentlehner, R. Riechers, B. Dick, A. Slenczka, U. Even, N. Lavie, R. Brown, and K. Luria, Rev. Sci. Instrum. **80**, 043302 (2009).

[44] F. Bierau, P. Kupser, G. Meijer, and G. von Helden, Phys. Rev. Lett. **105**, 133402 (2010).
[45] L. Chen, J. Zhang, W. M. Freund, and W. Kong, J. Chem. Phys. **143**, 044310 (2015).
[46] J. Zhang, L. Chen, W. M. Freund, and W. Kong, J. Chem. Phys. **143**, 074201 (2015).

Chapter 2 Experimental setup I:

Superfluid Helium Droplets

2.1 Understanding Superfluid Helium

2.1.1 Phase Diagram of ^{4}He

Helium is the second lightest element after hydrogen. It is the only element/substance that remains liquid at absolute zero temperature (0 K) under one atmospheric pressure (1 atm).[1] Liquid helium only solidifies when the pressure reaches 25 atm at temperatures of lower than 2 K. Helium has two stable isotopes: ^{4}He (99.9998%) and ^{3}He (0.0002%). Since ^{4}He is the predominant isotope, in the following, only properties of ^{4}He will be discussed.

Fig. 2.1 shows the phase diagram of helium at low temperatures[2]. Liquid helium is considered a quantum liquid because of its large zero-point energy at 0 K of -59.4 kJ/mol, as compared with a value of about -627.6 kJ/mol for a classical crystal.[1] Helium has two liquid phases. In the temperature range of 2.17 K and 5.2 K (critical temperature), it is a normal fluid labeled He I in Fig 2.1. Only when its temperature drops below 2.17 K can the superfluid phase form (He-II in Fig 2.1)

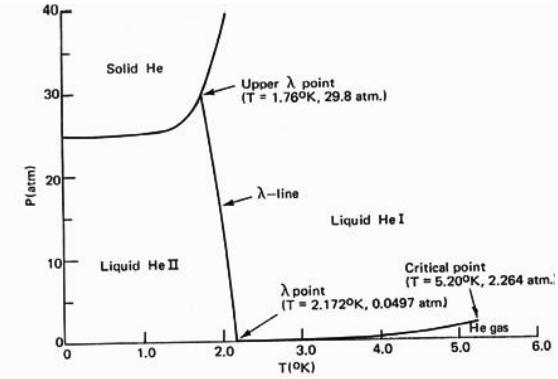

Fig. 2.1 Phase diagram of helium.[2]

2.1.2 History of Superfluid Helium

The history of superfluid helium dates back to over a century ago.[3] Helium was first liquefied by H. Kamerlingh Onnes in 1908 using several precooling stages (liquid air then liquid hydrogen) and the Hampson-Linde cycle based on the Joule-Thomson effect.[4] After reaching the boiling point of 4.2 K at 1 atm, Onnes further cooled the liquid to near 1.5 K by reducing the pressure with a vacuum pump.[4] He received the Nobel Prize in physics in 1913 for 'his investigations on the properties of matter at low temperatures which led, inter alia, to the production of liquid helium'. Superfluid helium was discovered in 1938 when Pyotr Kapitsa[5] and, independently, John Allen and Don Misener[6], measured the flow rate of helium below the temperature of 2.17 K. The researchers recorded a remarkable discontinuity in the heat capacity, as shown in Fig. 2.2. The heat capacity first decreases with lowering temperature, but the trend takes on a dramatic reverse as the temperature reaches 2.17 K, after which, the heat capacity asymptotically reaches zero at even lower temperatures. The shape of the heat capacity near the transition temperature looks like a Greek letter λ, so it is called the 'λ transition'. Moreover, the viscosity of the fluid was also observed to decrease dramatically, to a point so low that Kapitsa coined the term "superfluid". Kapitsa was later awarded the Nobel Prize in Physics for his 'basic inventions and discoveries in the area of low-temperature physics'.

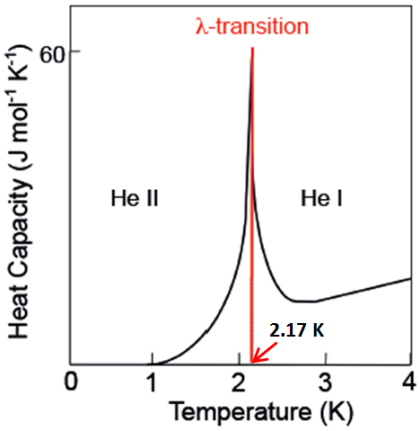

Fig. 2.2 The heat capacity of liquid ^{4}He including the λ transition[7].

Shortly after, London and Tisza suggested a two-fluid model to describe superfluid helium: a normal fluid and a superfluid.[8] As the temperature decreases, the fraction of superfluid increases. The ratio of the two components can be measured by placing the liquid in a cylindrical metal container suspended by a wire. When a twist was imparted to the wire, the cylinder would rotate, but only the normal helium would rotate with the cylinder. A larger fraction of the superfluid component would result in a faster rotating cylinder, due to diminished friction. When the temperature is lowered substantially below 2.17 K, the entire liquid is converted into superfluid.

2.1.3 Landau's Theory

In 1941, Landau suggested that superfluidity can be understood in terms of the excitation spectrum of the liquid: the phonons and rotons.[8] Fig. 2.3 shows the dispersion relation of superfluid helium obtained by inelastic neutron scattering.[9] The vertical axis is the energy $\varepsilon = \hbar\omega(k)$, the horizontal axis is the wavevector k of the phonon wave, and the profile is determined by the distribution of elementary modes existing in liquid helium. The ratio of the vertical and horizontal values on the profile

corresponds to the velocity of the phonon wave. The excitation spectrum of liquid helium contains two different regions: one is the phonon region associated with low linear momentum, while the other is a quadratic function with a local minimum at a finite value (1.92 $Å^{-1}$, 8.65 K). The resulting maximum in the dispersion relation is called “maxon”, and the minimum is called “roton”.

This dispersion curve of helium is unique because of the existence of the roton minimum -- the roton gap E_{gap} = 8.65 K, while in a normal liquid, the roton minimum is zero. Correspondingly, a critical velocity can be defined by v_{Landau} = $E_{gap}/p \approx 58$ m/s (green dotted line in Fig 2.3), as the minimal velocity required to excite any quantum state of the liquid. Consequently, particles moving at velocities below the Landau velocity experiences no “mechanical” friction, as shown by the red dotted line in Fig 3.3. The Landau velocity is crucial for dopant pick-up by superfluid helium droplets, because a particle should be at least moving at 58 m/s relative to a helium droplet for friction to kick in and to slow down the particle.

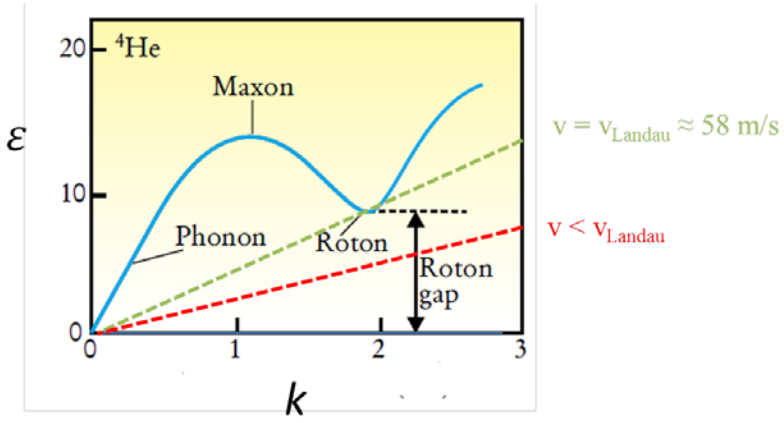

Fig. 2.3. The dispersion relation of liquid helium.[9]

2.2 Overview of superfluid helium droplets

2.2.1 History of helium droplets

Helium droplets are large helium clusters typically ranging from a few hundred up to a few billion helium atoms per droplet. Due to its finite radius, a helium droplet does not exhibit a continuum of phonon and roton excitations, which is different from bulk superfluid helium.

The formation of helium droplet beams using cryogenic free jet gas expansions was first reported by Becker et al. in 1961.[10] Gspann et al. continued the research with scattering and deflection experiments[11]. In the late 1980s, Toennies group showed that one or more gas phase molecules could readily be doped into helium droplets.[12] By combining doped droplets with spectroscopic techniques, Scoles et al. were able to detect infrared absorption of sulfur hexafluoride (SF_6).[13] They assigned two central absorption features located at 945.8 and 946.4 cm^{-1} to a single isolated SF_6 molecule on the surface of a helium droplet, and they also admitted that the results represented only a first step towards a deeper understanding the doping of helium droplets.[13] In 1994, Vilesov et al. performed high-resolution infrared spectroscopy of embedded SF_6.[14] From the sharp spectral lines, the authors suspected that SF_6 can freely rotate inside helium droplets.

The first experimental evidence that helium droplets are superfluidic came in 1996 by Hartmann et al. from electronic excitation of embedded glyoxal ($C_2H_2O_2$).[15] The gap between the zero phonon line (ZPL) and a phonon wing (PW), and the structure of the PW, are both considered indications of superfluidity. Thereafter, Grebenev et al. reported free rotation of carbonyl sulfide (OCS) inside helium droplets[16], and the

appearance of a sharp rovibrational spectrum further established the superfluidity of helium droplets. Since then, helium droplets have become a fascinating subject of study, spurring a tremendous growth of research activities in recent years.[17-19]

Helium droplets are produced by expansion of high pressure helium ($P \geq 20$ bar) through a cooled nozzle ($T \leq 20$ K) into vacuum.[17] Depending on the stagnation pressure and the nozzle temperature, there are three distinct helium expansion regimes to generate droplets of different sizes:

Regime I (Sub-critical expansion): droplets are formed by condensation of helium gas upon expansion from the nozzle. Further cooling to 0.37 K is achieved via evaporation of helium atoms from the surface. Typical droplet sizes produced in this regime are 10^2 to 10^4 helium atoms, and the size distribution follows a log-normal function:

$$P(N) = \frac{1}{\sqrt{2\pi}} \exp\left[-\frac{(lnN-\mu^2)}{2\delta^2}\right], \quad (2.1)$$

where $P(N)$ is the probability of a droplet consisting of N helium atoms, μ is the mean of the distribution of ln N, and δ is standard deviation of the distribution of ln N. From Eq. 2.1, the average droplet size $< N > = \exp(\mu + \frac{\delta^2}{2})$, which has been confirmed from deflection experiments with a secondary beam of Kr or Ar.[20]

Regime II (Critical expansion): droplets are formed through a combination of gas condensation and liquid fragmentation. Average droplet sizes produced are estimated to be $>10^4$ helium atoms. However, a quantitative expression of droplet size distribution has not been developed.

Regime III (Super-critical expansion): droplets are formed from fragmentation of liquid, with a much larger average size, from 10^5 to 10^{11} helium atoms. The size distribution is an exponential function;

$$P(N) = \frac{1}{N}\exp(-\frac{N}{<N>}) \qquad (2.2)$$

The size distribution from super-critical expansion has also been measured by deflection of charged droplets in an electric field[21] in the size range of 10^5 <N< 10^7. The sizes of much larger droplets in a continuous droplet beam were characterized by Vilesov's group by titrating the beam with argon and helium atoms at room temperature. The authors found that droplets produced in this regime could be as large as 10^{11} helium atoms.[22]

2.2.2 Literature review

2.2.2.1 The pickup process and metastable clusters in helium droplets

Intentional doping of helium droplets with the species of interest is accomplished by the 'pickup' process. This process is achieved by collisions between droplets with the desired gas phase molecules. It involves passing the helium droplet beam through a pickup chamber that is maintained at a sufficient vapor pressure. If the droplet is large enough in size, the pickup process follows Poisson statistics,[19] which means that for a droplet of N helium atoms, the probability of capturing a given number of dopant molecules k from a pick up cell of length L is P_k,

$$\mathrm{P_k} = \frac{(\rho\sigma L)^k}{k!}\exp(-\rho\sigma L) \qquad (2.3)$$

where ρ is the number density of the dopant gas in the pickup cell, and σ is the cross section of the droplet: $\sigma = \pi r_0^2$ with $r_0 = 2.22\sqrt[3]{N}$ $(\AA)$. After pickup, the thermal energy of the dopant species is dissipated into the helium droplet, resulting in isotropic evaporation of helium atoms. If the droplet is sufficiently large, the final temperature of the doped droplet reaches 0.37 K in 10^{-7} - 10^{-9} s.[23]

The invention of the superfluid helium droplet technique and the possibility of doping with foreign species have captured the interest of a wide range of physical chemists.[17,19] While impurities in bulk superfluid helium precipitates and drops out of the liquid, molecules embedded in superfluid helium droplets are cooled to ~0.4 K and are free to exhibit gas phase behaviors. Moreover, the rapid cooling rate upon doping can prevent the newly doped molecules from overcoming small local potential barriers to find the global minimum; molecules can be trapped in a certain configuration, or aggregates can be stuck in shallow local minima[24-26]. Nauta et al. reported the formation of linear-chain $(HCN)_n$ (n = 2 – 7) where successively captured HCN molecules are oriented by the long-range dipole–dipole forces.[25] This structure is different from that formed in a conventional supersonic expansion where cyclic trimers are the global minimum. In another example, cyclic water hexamers are detected in superfluid helium droplets instead of the more stable cage structure in supersonic molecular beams.[24] We have observed the formation of halogen bonds in iodine clusters formed in superfluid helium droplets based on electron diffraction[27] (see chapter 8 for details).

Another interesting consequence of the fast cooling rate of superfluid helium droplets has been shown in the formation of mixed clusters, such as Mg_3–HCN[28], HF–$Ar_{1–5}$[29], OCS-$(H_2)_{1-16}$[30,31] and tetracene–Ar_{1-5}[32]. These clusters are typically synthesized with two or more successive pickup cells. The resulting clusters, in some case, are structurally sensitive to the pickup sequence. For example, if Ar_n is first formed in the initial pickup cell, it remains intact after the addition of tetracene[33] in a second pickup cell. On the other hand, if the pickup sequence is reversed, then Ar atoms are found to attach with equal probabilities to both sides of the flat molecule.

A more recent development in the field of superfluid helium droplets is to use the droplets as reactors for synthesis of nanoparticles.[34,35] The doped droplet beam is directed to a grid of a transmission electron microscope, and dopant particles are deposited after helium evaporation. The low impact velocity and the cushioning effect of helium during impact are both beneficial in preventing fragmentation or coagulation of the dopant clusters.[35] Although still in its infancy, this field has reported synthesis of a number of metallic nanoparticles, including pure Ag nanoparticles composed of 300 - 6000 atoms[36], Mg nanoclusters[37], poly-crystalline Ag nanoparticles[38], Cu clusters[39] and Ni/Au core–shell nanoparticles[34].

2.2.2.2 Location of dopant molecules

An interesting issue of doped droplets is the location of the dopant: inside or on the surface of the helium droplet. So far most close-shell molecules have been found to locate in the interior of helium droplets, while permanent residence at the surface only occurs for alkali and alkaline earth metal atoms.[19] The weak dispersion forces cannot

overcome the short-range Pauli repulsion (due to Pauli principle) of the *s* electrons in helium atoms and the surface tension of the droplet to migrate into the droplet and experience the interatomic attractive potential inside a droplet.

The first conclusive evidence of surface-bound atoms came from spectroscopic studies of helium droplets doped with alkali atoms (Li, Na, K).[40] The excitation of these alkali atoms occurs at frequencies close to their gas phase values. In addition, the binding energies of these atoms to the surface of a droplet are also calculated to be low[41], on the order of ~10 cm^{-1}. Consequently, only triplet alkali dimers have been observed on the surface of helium droplets, since the formation of singlet dimers releases more than 4000 cm^{-1} of energy, resulting in selective desorption of singlet dimers/[42] Only when the alkali clusters reach a sufficiently large size can the van der Waals attraction between the alkali cluster and the helium matrix overcome the repulsive energies on a droplet surface. Ultimately, for Na_n with $n \geq 21$ while for K_n with $n \geq 80$, the alkali clusters become submerged inside helium droplets.[43,44]

2.2.2.3 Vortices in helium droplets

Rotational excitation inside superfluid helium generates quantized vortices. The vortex core does not decay due to lack of viscous diffusion. Quantized vortices of superfluid helium are therefore more stable and definite than classical vortices. In 2006, Bewley et al. observed the geometry and interactions of these vortices in bulk liquid helium using small solid hydrogen particles: arrays of hydrogen particles are pinned to the vortex line with diameters of about an angstrom.[45] The existence of quantum vortices in helium droplets has been proved only recently. Geomez et al. reported observation of track shaped deposits when multiple Ag atoms were doped in

droplets with diameters larger than 300 nm.[46] They believe that the tracks are due to Ag atoms pinned to quantized vortices across the helium droplets. The overall lengths of these traces are generally consistent with the diameters of the helium droplets, on the order of ~300 nm. In 2014, vortices in superfluid helium droplets have been directly confirmed for the first time via coherent x-ray scattering from a free electron laser.[47] Xeon clusters trapped in the vortex cores of droplets containing 10^8 - 10^{11} helium atoms (200 - 2000 nm in diameter) are observed to show Bragg diffraction patterns, corresponding to a two-dimensional matrix of vertices.

Quantized vortices in superfluid liquids have recently attracted attentions from physicists and chemists alike.[48,49] Modern optical techniques have enabled direct visualization of quantized vortices, and multi-component Bose–Einstein condensates have further enriched the world of quantized vortices. A primary interest is to understand the relationship between classical and quantum turbulence. The presence of quantized vortices also provides guidance for the growth of one-dimensional nanowires, such as Ni, Cr, Au and Si nanowires.[50] The sequential pickup scheme enables the formation of Au/Ag core-shell nanowires along vortices in helium droplets, where the center of the nanowire is rich in the first element and the outer region is rich in the subsequent element along the doping path.[49]

2.3 Experimental setup: Pulsed superfluid helium droplet source

There are two types of commonly used sources for generating superfluid helium droplets: a continuous and a pulsed source.[17] Continuous droplet sources have been well established in many laboratories. This type of sources requires large pumping

speeds in order to maintain appropriate vacuum levels. Thus the nozzle diameter of a continuous source is typically on the order of a few microns and clogging is an issue for operation. The resulting droplet density is also limited. However, since there is no moving part in the source, a continuous source is stable and suitable for most spectroscopic experiments. In contrast, orders of magnitude higher fluxes have been reached in pulsed droplet sources, and with a low duty cycle in most experiments (< 1 kHz repetition rate), the gas load is significantly reduced. Unfortunately, pulsed sources do have an intrinsic heat load due to the mechanical movement of the pulsed valve, which could limit the achievable low temperature of the source and the stability of droplet beam, both in temporal profiles and in density. A typical feature of pulsed sources is velocity slip among different sized droplets: the temporal profiles of different sized droplets within one pulse are different, with smaller droplets moving at a faster speed at the front of the droplet beam.[51,52] Several groups including our own have taken advantage of this feature and achieved size selection of helium droplets.[27,51]

The design and operation of pulsed droplet sources have gone through several iterations in the community. Slipchenko *et al.* first succeeded in producing repetitive pulses of helium droplets by modifying a commercially available solenoid valve for molecular beams.[53] The sealing component of the valve is made of copper, which can operate at cryogenic temperatures. However, in their initial study, it was difficult to control the droplet size in any systematic and predictable fashion. Subsequently Yang *et al.* modified the nozzle geometry, which allowed easier control of droplet sizes[54]. Currently a preferred pulsed valve is the Even-Lavie valve [55](E-L), as shown in Fig

2.4. This solenoid valve operates by energizing a low resistance coil (0.1 Ω) with a pulsed current source (10-150 A). A low mass magnetic plunger is pulled by the magnetic field of the solenoid and is returned to its sealing position by a pusher spring. The amplitude of the driving electrical pulse is 24 V and the duration is 24.9 μs in our setup. The valve can be operated from 8 K - 400 K, limited by the cooling capacity of the cryostat and the heat load of the solenoid.

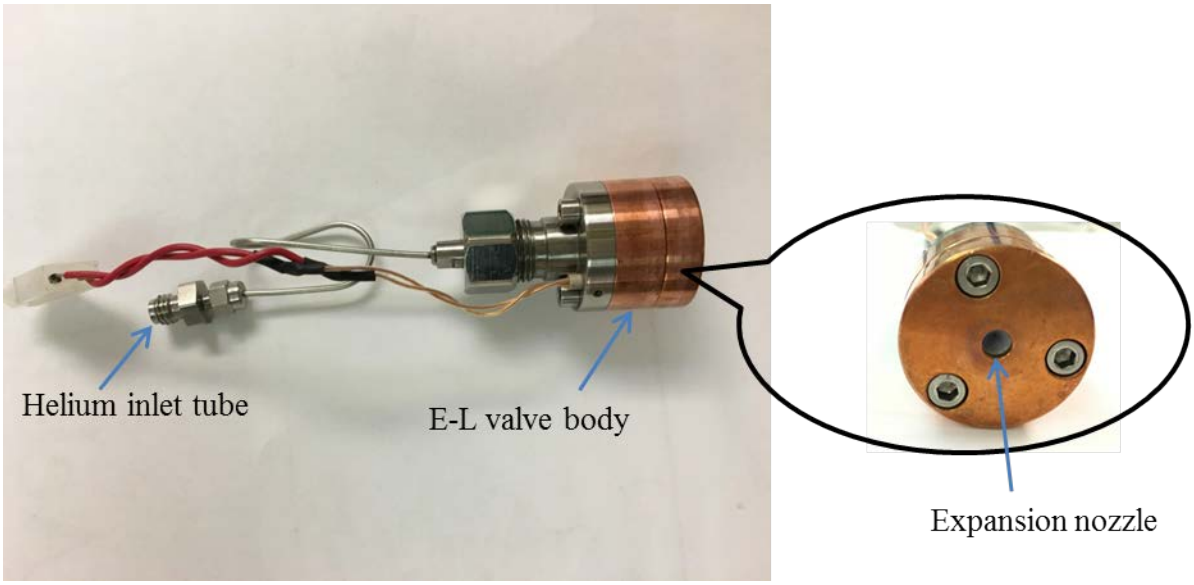

Fig. 2.4 E-L pulsed valve in the experimental setup (unmounted from a cryostat).

The cross section of an E-L valve and its internal parts are detailed in Fig. 2.5. The front housing of the valve is a cylindrical copper body (coated with titanium nitride to prevent oxidation) to ensure good thermal conductivity, and it is mounted onto a closed-cycle helium refrigerator with a regulated 50 Watt heater for control of the source temperature. High pressure (50 bar) ultra high purity (99.9995%) helium gas is filtered and then pre-cooled before being introduced from the gas inlet tube (1). The gas then enters a thin-walled pressure vessel (6) formed by a tube sealed between two thin Kapton gaskets (3 and 11). Both gaskets are pressed to the tube by a strong

spring (2) that also compensates for thermal contraction during cooling. Movement of the plunger (7) is limited to less than 0.05 mm during operation. The return spring (5) pushes the plunger back to complete the cycle. The nozzle on the front plate for gas expansion (13) is conical in shape with an opening of 50 μm in diameter.

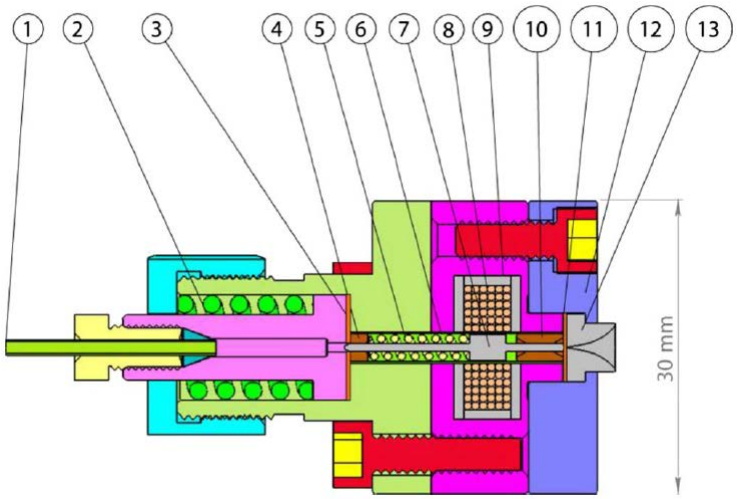

Fig. 2.5 Cross section drawing of the E-L valve

1. Stainless gas inlet tube (1/16"); 2. Tightening spring and pressure relief valve.

3. Rear kapton foil gasket (0.125 mm. thickness); 4. Ruby rear guiding ferrule.

5. Return spring; 6. Thin walled pressure vessel.

7. Plunger; 8. Kapton insulated copper coil.

9. Magnetic shield and field concentrator; 10.Ruby front guiding ferrule.

11.Front kapton foil gasket (0.125 mm. thickness); 12.Front flange (TiN coated copper).

13.Expansion nozzle

Downstream from the pulsed valve, a 2 mm dia. skimmer was used to create a collimated helium droplet beam before the pickup chamber. Fig. 2.6 shows the inside view of the source chamber, with the skimmer magnified. The vacuum in the source

chamber is kept below 2 x10 $^{-7}$ Torr by a diffusion pump (Varian VHS-6) below the copper cooling plate (E-L valve off). When the E-L valve is running at 5 Hz, the vacuum in the source chamber is around 5 ×10^{-6} Torr, and consequently, the pressure in the downstream pickup chamber increases by 0.2-0.4 × 10^{-7} Torr, and further downstream in the main chamber by 0.1-0.5 × 10^{-9} Torr.

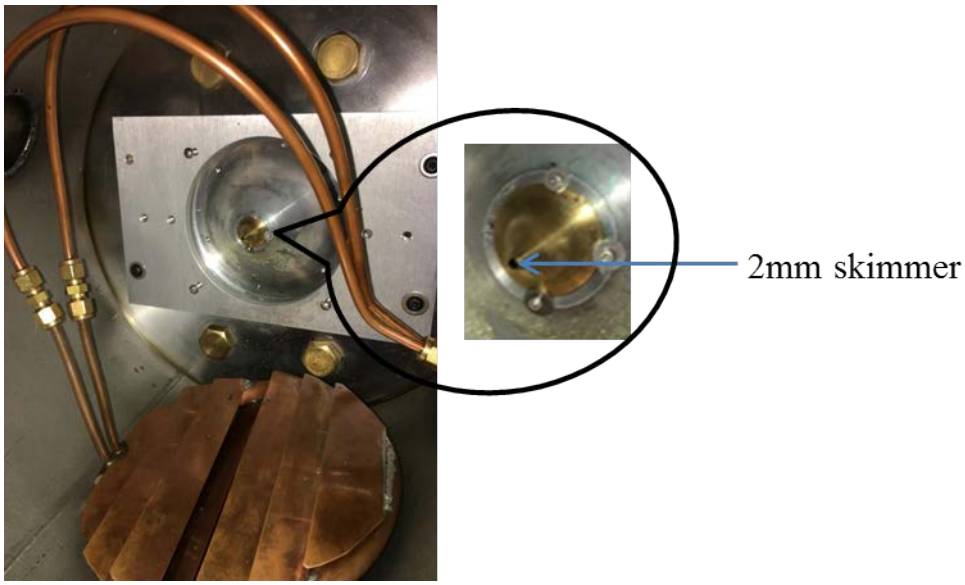

Fig. 2.6 Inside view of the source chamber downstream from the pulsed valve.

2.4 Doping neutral molecules into helium droplets

We developed two different doping methods into helium droplets: a continuous doping cell and a pulsed valve – named sample PV in the following. The continuous doping cell introduces the sample either from outside the doping chamber via a feed-through tubing, or by heating the sample in the cell (oven). The former is for gaseous samples, while the latter is for non-volatile species. A problem with this doping cell is that the sample is constantly fed into the doping chamber, hence a great portion of the sample can be deposited on the chamber wall. A pulsed valve for doping can be synchronized with the droplet source, thereby significantly reducing sample diffusion

into the diffraction region. However, a pulsed valve can only be heated up to a certain temperature, 200 °C in our case, thus limiting the scope of applicable samples, particularly for samples with extremely low vapor pressures such as salts and metallic compounds. Of course for any pulsed experiment, timing is also an unavoidable complication.

2.4.1 Doping cell

The continuous doping cell is shown in Fig. 2.7. Gaseous sample such CCl_4 and CBr_4 was introduced into the doping cell through a vacuum feed-through into a flexible gas line (6 mm in outside diameter), which was then routed to the bottom of a pickup cell. The cell is 4 cm in diameter with two circular apertures of 5 mm in diameter on the wall along the path of the droplet beam. Room temperature vapor of CCl_4 was controlled by a leak valve, and it was sufficient to just open the leak valve to produce a stable doping pressure. The doping cell can also be replaced by a similarly designed oven and heated to high temperatures for low vapor pressure species, such as metals or large rigid organic molecules: in this case, the sample is directly deposited in the doping oven. Several versions of the doping oven have been used over the years, and with the newest design, temperatures as high as 2000°C can be reached, although a problem of sample deposition and clogging of the droplet path – the 5 mm clearance holes on the oven – occasionally poses a problem.

The pickup chamber was separated from the main diffraction chamber through a home-made conical cone with a 5 mm dia. opening, also shown in Fig. 2.7. The pressure in the pickup chamber was measured from an ionization gauge ~12 cm away from the droplet beam. The base pressure in the pickup chamber was below 10^{-6}

Torr, and the pressure range for doping is from 1×10^{-6} Torr to 5×10^{-5} Torr. A shielding plate was mounted upstream from the doping cell to prevent backflow of the sample vapor into the source chamber, which could contaminate the droplet PV.

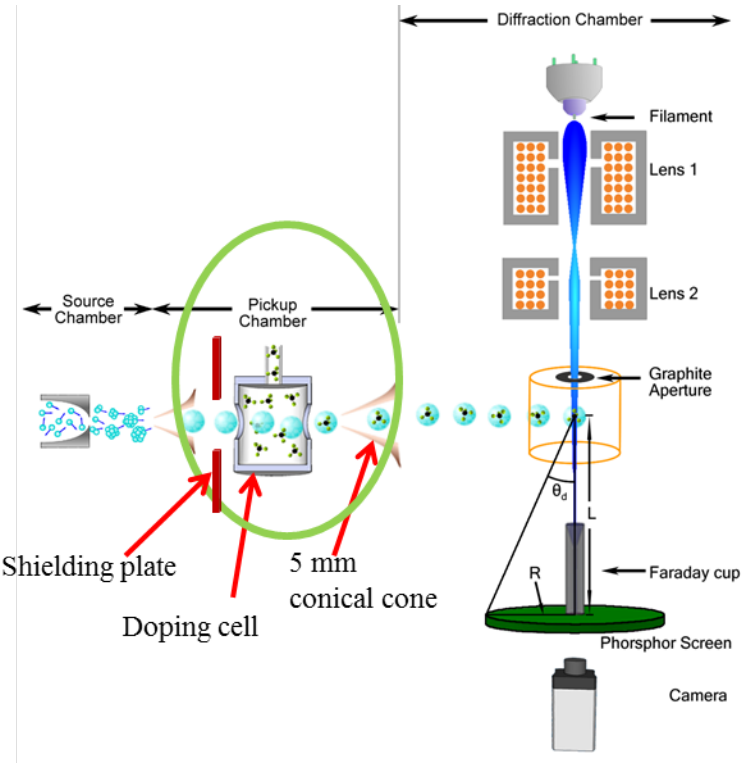

Fig. 2.7 Schematic diagram of the experimental setup (pickup chamber highlighted in green circle)

2.4.2 Pulsed valve doping

We have also succeeded in using a pulsed value for doping. The purpose of this approach is not limited to lowering the gas load of the doping chamber. More importantly, we would like to be able to record the difference signal with and without dopant molecules, or with and without the droplet beam. Pulsed doping offers the ability to effectively remove slow drifts of the experimental conditions, and remove contributions of diffused sample into the diffraction region. For semi-volatile species directly enclosed in the pulsed valve, the sample PV has to be heated, but in the

meantime, this setup also eliminates a heated doping gas line into the diffraction chamber.

Fig. 2.8 shows the arrangement of the pulsed valves in the experiment. The assembly of the sample PV (Parker, series 9) replaces the doping cell in the doping chamber, and the non-volatile sample such as ferrocene was housed in the pulsed valve and heated to 73ºC. The sample PV was located 10 cm downstream from the opening side of the skimmer and 5 mm away from the center of the traversing droplet beam. Without any carrier gas, the sample PV produced diffusive ferrocene molecules permeating the pickup chamber.

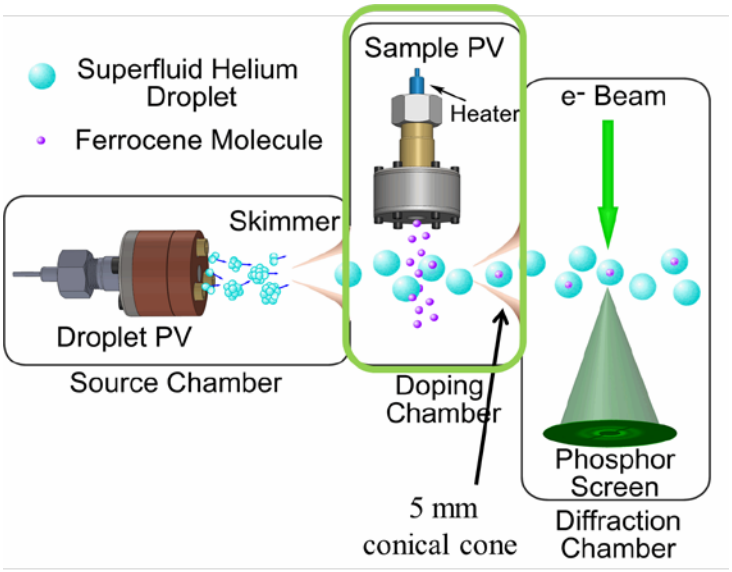

Fig. 2.8 Pulsed valve delivery for sample doping, highlighted in green rectangle.

To achieve effective doping, we need to determine the relative timing of the sample PV to the droplet PV, and the duration of the sample PV. Our diagnostic tool is the MPI mass spectrometer (details in section 2.5). Since the ionization source of the mass spectrometer is also a pulsed laser, the search for the best timing of the experiment is multi-dimensional, including two timing pulses (laser and sample PV,

in reference to the droplet PV) and one pulse width (sample PV). At a fixed nozzle temperature of the droplet PV, the size and velocity distribution of the helium droplet are fixed. With the sample PV set at sufficient duration, we can observe MPI signal from the doped droplets in a time range relative to the timing of the droplet PV. Scanning the timing of the laser relative to the droplet PV can yield the best timing for the laser. With the laser at the optimal timing, we can optimize the timing of the sample PV.

A condition for optimal doping is that the sample PV has to supply sufficient dopant molecules in the vicinity of the droplet beam prior to the arrival of the droplet beam. This is achieved by releasing the sample gas early enough for pressure to build up, and by increasing the duration of opening time of the sample PV. At a relatively short duration, with changing delay between the two PVs, an optimal timing can be obtained from the ionization yield, as shown by the black trace in Fig. 2.9. Increase in the duration of the sample PV can result in over-saturation of the doping process, as shown by the two maxima in the ion yield (the red and blue traces). The first peak corresponds to the necessary buildup time of the dopant molecule in the doping region. Once the pressure builds up, more sample molecules end up destroying the droplets due to excessive collisions, and the ionization yield decreases. This drop in ionization signal is therefore an indicator that the sample doping pressure is too high. As the delay between the two PV further increases, some dopant molecules released earlier are pumped out of the doping region prior to the arrival of the droplet beam, and the right doping condition is achieved again. The long tail of the blue trace shows the slow pumping speed of the system after the sample pulsed valve is shut down. It

is worth noting that with the change in the duration of the sample PV, the timing of the laser beam and timing of the sample PV can also be affected. Iteration of the optimization process is necessary.

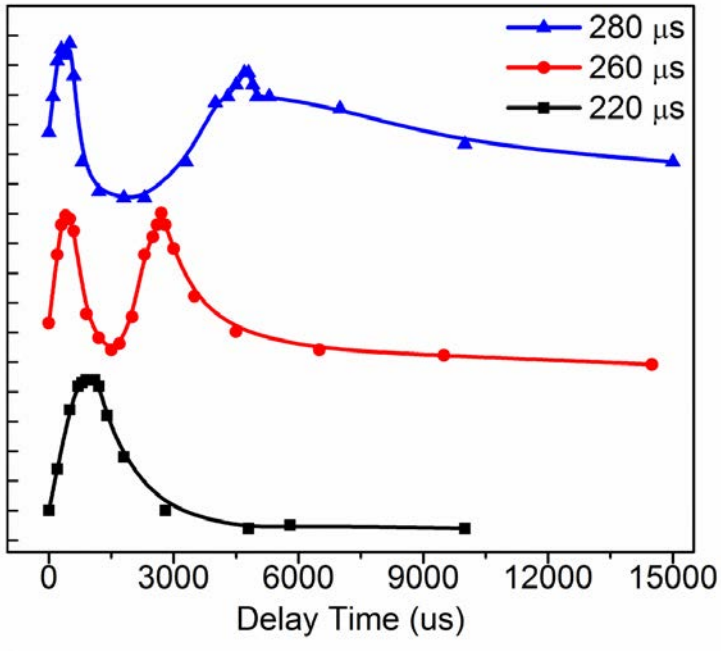

Fig. 2.9 Fe^+ signal from MPI varies with the delay time between the droplet and sample PV.

The doping process is Poission in nature[19], hence it is impossible to achieve 100% doping of all droplets with just one dopant molecule in one droplet. In diffraction experiments, undoped droplets pose a severe problem in generating a strong background, hence we tried to minimize the existence of undoped droplets by choosing a longer than necessary width for the sample PV as indicated by the red and blue traces, and by setting the sample PV at a timing passed the first peak of the red or blue trace. Under this condition, we lose some small droplets because of too many collisions with the sample molecules, but in the meantime, we also increase the

fraction of droplets containing dopant molecules. Since the uptake of each dopant molecule requires evaporation of a fixed number of helium droplets, this method can selectively eliminate small droplets and only leave large droplets with multiple dopant molecules for diffraction. In the presence of a velocity slip and with pulsed sampling, this method offers a path to size select the dopant cluster. We have successfully employed this method for diffraction of monomeric ferrocene and two different sized iodine clusters embedded in helium droplets. [27,56]

2.5 Characterization of the helium droplet beam

We used two homemade Wiley-McLaren type time-of-flight mass spectrometers for characterization of the droplet beam, and details of the experimental setup and results will be presented in Chapter 4. One mass spectrometer uses electron impact ionization (EI-TOF) downstream from the diffraction region. It can ionize helium atoms and all dopant species, and it is used to check the performance of the undoped droplet beam and the doped droplet beam. The other relies on laser ionization (MPI-TOF) in the region of diffraction. The laser can only ionize dopant molecules, but since it is located right at the diffraction region, it can also provide the precise timing of the doped droplet beam.

For EI-TOF, the electron source was a commercial fast ion gauge (Beam Dynamics, Inc, Model FIG-1), as shown in Fig. 2.10. Under its default setting, electrons from the heated tungsten filament are accelerated towards the grid by a potential of 160 V. In the region of the grid, ionization of gas molecules takes place. The ions travel to the central collector wire which is not intentionally biased, and the resulting current is amplified by an operational amplifier which has a voltage gain of approximately 50.

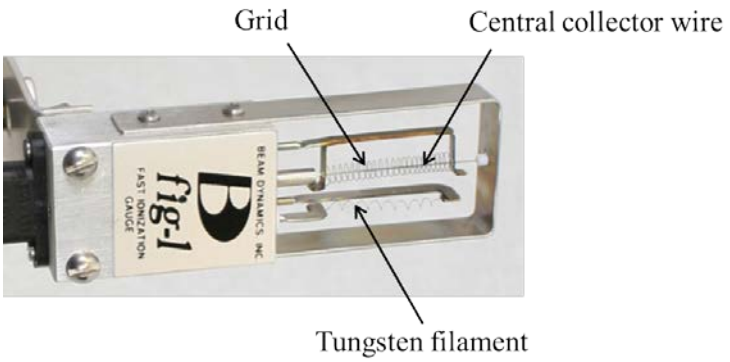

Fig. 2.10 The structure of a fast ion gauge (FIG).

In the EI experiment, the FIG was rewired as an electron source. Fig. 2.11 shows the arrangement of the FIG and details of the electrodes of the EI-TOF. The tungsten filament of the FIG supplied electrons by running at a constant current of 2.4 A, and the collector grid facing the filament was biased at 51 V to contain the thermal electrons. The droplet beam passed through the space between the filament and the grid. About 12 mm downstream from the electron source were three electrodes A – C separated by 19 mm, as shown in Fig 2.11(c), and the flight tube further downstream was about 43.2 cm long. Electrodes A and C were pulsed from -70 V to 300 V for 4 μs using a DEI PVX-4140 pulse generator, while electrode B was grounded. The negative voltage on electrode A was to prevent electrons from entering the interior of the mass spectrometer. Once the electrons were energized by the positive pulse, ionization was confined to the vicinity of electrode A, and ionized cations were pushed to electrode B. The duration of 4 μs of the ionization pulse was necessary for accumulation of ions around electrode B. As soon as the voltage on electrode C was dropped back to -70 V, all cations accumulated between B and C were attracted to the flight tube, which was biased at a constant voltage of -180 V. Hence the time-of-flight

of the detected ions started at the falling edge of the positive pulse. Ion signals were detected on a chevron-type microchannel plate detector (MCP).

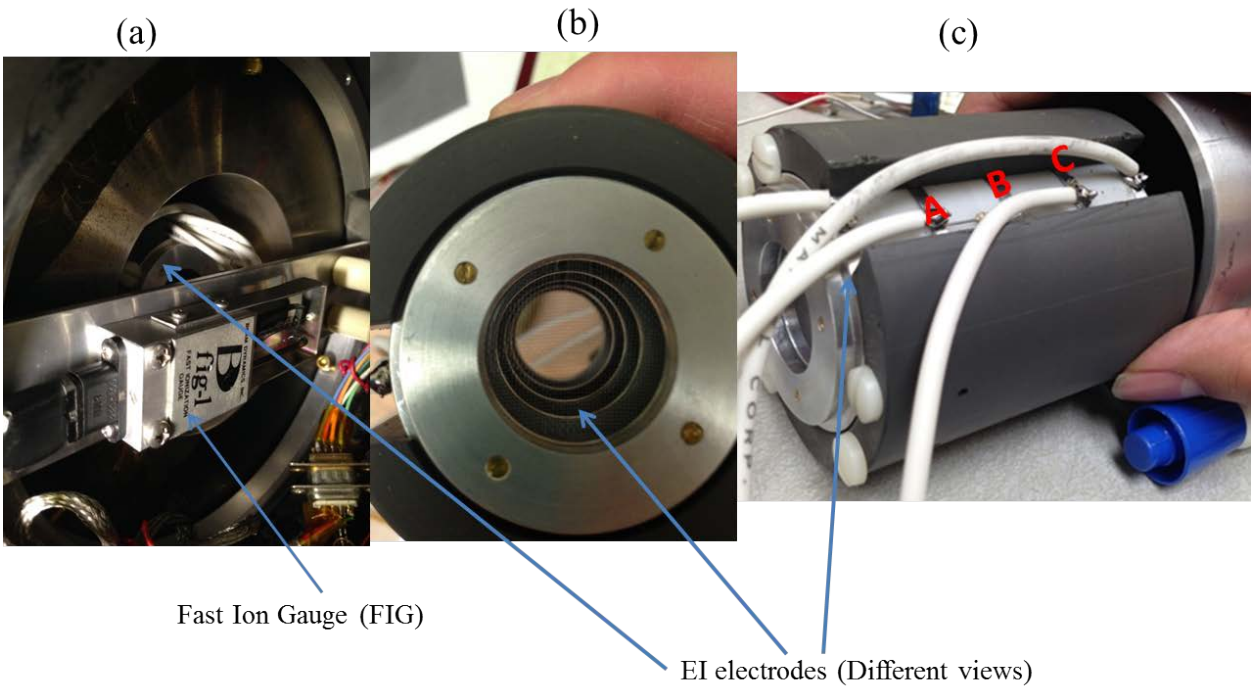

Fig. 2.11 (a) EI-TOF setup in the main chamber showing the FIG as the ionizer. (b) Front view of the EI electrodes without the FIG, (c) Side view of the EI electrodes, with labels and no FIG.

Fig. 2.12 shows details of the MPI-TOF. The MPI station was mounted with two pins inserted into the holes on the rotatable wheel. Although the opening meshed area on the electrodes is ½", a ¼" hole on the rotatable wheel ultimately limits the acceptance aperture for the passing ions. The MCP detector and the bottom half of the TOF tube were mounted on a slide movable rail system, and it could be retracted to a corner of the chamber using a cajon feedthrough.

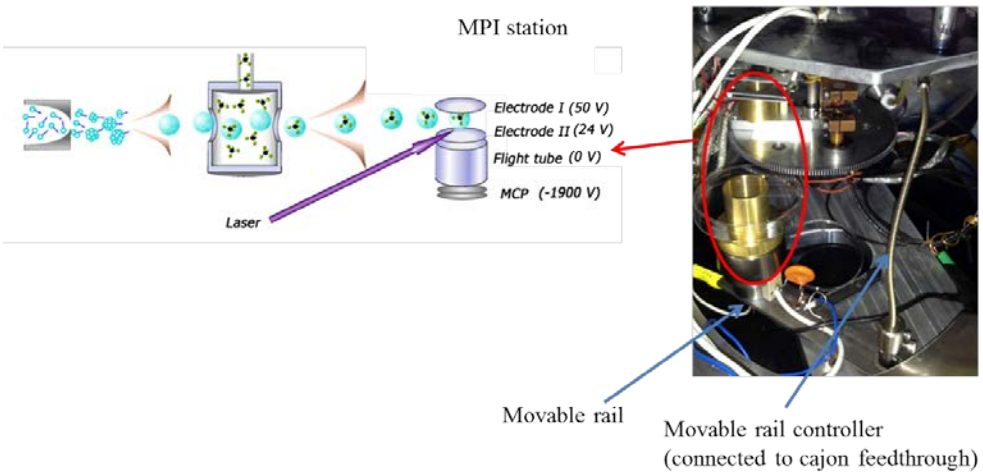

Fig. 2.12 MPI-TOF setup in the main chamber

The two mass spectrometers serve complementary purposes. With only a heated filament and pulsed electrodes, the EI-TOF mass spectrometer can resolve ionized helium clusters such as He_2^+ and He_4^+, which are signatures of superfluid helium droplets. Without ionizing any helium atoms, MPI of CCl_4 doped in superfluid helium droplets generates complex cluster ions of dopant fragments with helium atoms, including $(He)_nC^+$, $(He)_nCl^+$ and $(He)_nCCl^+$. Using both methods, we have characterized our cryogenic pulsed valve – the Even-Lavie valve. As will be discussed in Chapter 4, we have observed a primary pulse with larger helium droplets traveling at a slower speed, and a rebound pulse with smaller droplets at a faster speed. These results stress the importance of fast and easy characterization of the droplet beam for sensitive measurements such as electron diffraction of doped droplets.

2.6 References

1 C. L. Pekeris, Physical Review **79**, 884 (1950).

2 J. S. Brooks and R. J. Donnelly, Journal of Physical and Chemical Reference Data **6**, 51 (1977).

[3] D. van Delft and P. Kes, Europhysics News **42**, 21 (2011).
[4] H. K. Onnes, presented at the Proceedings of the KNAW, 1911 (unpublished).
[5] P. Kapitza, Nature **141**, 74 (1938).
[6] J. F. Allen and A. D. Misener, Nature **141**, 75 (1938).
[7] M. J. Buckingham and W. M. Fairbank, Progress in Low Temperature Physics **3**, 80 (1961).
[8] L. Landau, Physical Review **60**, 356 (1941).
[9] R. A. Cowley and A. D. B. Woods, Canadian Journal of Physics **49**, 177 (1971).
[10] B. E. W, K. R, and Z. Lohse P, Naturforsch. A **16** (1961).
[11] J. Gspann, Physica B+C **108**, 1309 (1981).
[12] A. Scheidemann, B. Schilling, J. P. Toennies, and J. A. Northby, Physica B: Condensed Matter **165**, 135 (1990).
[13] S. Goyal, D. L. Schutt, and G. Scoles, Physical Review Letters **69**, 933 (1992).
[14] R. Froechtenicht, J. P. Toennies, and A. Vilesov, Chem. Phys. Lett. **229**, 1 (1994).
[15] M. Hartmann, F. Mielke, J. P. Toennies, A. F. Vilesov, and G. Benedek, Phys. Rev. Lett. **76**, 4560 (1996).
[16] S. Grebenev, J. P. Toennies, and A. F. Vilesov, Science **279**, 2083 (1998).
[17] J. P. Toennies and A. F. Vilesov, Angew. Chem., Int. Ed. **43**, 2622 (2004).
[18] J. A. Northby, J. Chem. Phys. **115**, 10065 (2001).
[19] S. Yang and A. M. Ellis, Chem. Soc. Rev. **42**, 472 (2013).
[20] J. Harms, J. P. Toennies, and F. Dalfovo, Phys. Rev. B **58**, 3341 (1998).
[21] U. Henne and J. P. Toennies, J. Chem. Phys. **108**, 9327 (1998).
[22] L. F. Gomez, E. Loginov, R. Sliter, and A. F. Vilesov, J. Chem. Phys. **135**, 154201 (2011).
[23] A. Lindinger, J. P. Toennies, and A. F. Vilesov, J. Chem. Phys. **110**, 1429 (1999).
[24] K. Nauta and R. E. Miller, Science **287**, 293 (2000).
[25] K. Nauta and R. E. Miller, Science **283**, 1895 (1999).
[26] K. Nauta, D. T. Moore, and R. E. Miller, Faraday Discussions **113**, 261 (1999).
[27] Y. He, J. Zhang, L. Lei, and W. Kong, Angew. Chem., Int. Ed. **56**, 3541 (2017).
[28] K. Nauta, D. T. Moore, P. L. Stiles, and R. E. Miller, Science **292**, 481 (2001).
[29] K. Nauta and R. E. Miller, The Journal of Chemical Physics **115**, 10138 (2001).
[30] S. Grebenev, B. G. Sartakov, J. P. Toennies, and A. F. Vilesov, The Journal of Chemical Physics **118**, 8656 (2003).
[31] S. Grebenev, B. Sartakov, J. P. Toennies, and A. F. Vilesov, Science **289**, 1532 (2000).
[32] M. Hartmann, A. Lindinger, J. P. Toennies, and A. F. Vilesov, Chemical Physics **239**, 139 (1998).
[33] N. Pörtner, A. F. Vilesov, and M. Havenith, Chemical Physics Letters **343**, 281 (2001).

[34] A. Boatwright, C. Feng, D. Spence, E. Latimer, C. Binns, A. M. Ellis, and S. Yang, Faraday Discuss. **162**, 113 (2013).

[35] S. Yang, A. M. Ellis, D. Spence, C. Feng, A. Boatwright, E. Latimer, and C. Binns, Nanoscale **5**, 11545 (2013).

[36] E. Loginov, L. F. Gomez, and A. F. Vilesov, J. Phys. Chem. A **115**, 7199 (2011).

[37] T. Döppner, T. Diederich, J. Tiggesbaumker, and K. H. Meiwes-Broer, Eur. Phys. J. D **16**, 13 (2001).

[38] A. Volk, P. Thaler, M. Koch, E. Fisslthaler, W. Grogger, and W. E. Ernst, J. Chem. Phys. **138**, 214312/1 (2013).

[39] L. F. GOMEZ, E. LOGINOV, A. HALDER, V. V. KRESIN, and A. F. VILESOV, International Journal of Nanoscience **12**, 1350014 (2013).

[40] F. Stienkemeier, J. Higgins, C. Callegari, S. I. Kanorsky, W. E. Ernst, and G. Scoles, Z. Phys. D: At., Mol. Clusters **38**, 253 (1996).

[41] R. Mayol, F. Ancilotto, M. Barranco, O. Buenermann, M. Pi, and F. Stienkemeier, Los Alamos Natl. Lab., Prepr. Arch., Condens. Matter, 1 (2004).

[42] O. Buenermann and F. Stienkemeier, Eur. Phys. J. D **61**, 645 (2011).

[43] d. L. L. An, P. Bartl, C. Leidlmair, H. Schoebel, R. Jochum, S. Denifl, T. D. Märk, A. M. Ellis, and P. Scheier, J. Chem. Phys. **135**, 044309/1 (2011).

[44] L. A. der Lan, P. Bartl, C. Leidlmair, H. Schoebel, S. Denifl, T. D. Maerk, A. M. Ellis, and P. Scheier, Phys. Rev. B: Condens. Matter Mater. Phys. **85**, 115414/1 (2012).

[45] G. P. Bewley, D. P. Lathrop, and K. R. Sreenivasan, Nature **441**, 588 (2006).

[46] L. F. Gomez, E. Loginov, and A. F. Vilesov, Phys. Rev. Lett. **108**, 155302 (2012).

[47] L. F. Gomez, K. R. Ferguson, J. P. Cryan, C. Bacellar, R. M. P. Tanyag, C. Jones, S. Schorb, D. Anielski, A. Belkacem, C. Bernando, R. Boll, J. Bozek, S. Carron, G. Chen, T. Delmas, L. Englert, S. W. Epp, B. Erk, L. Foucar, R. Hartmann, A. Hexemer, M. Huth, J. Kwok, S. R. Leone, J. H. S. Ma, F. R. N. C. Maia, E. Malmerberg, S. Marchesini, D. M. Neumark, B. Poon, J. Prell, D. Rolles, B. Rudek, A. Rudenko, M. Seifrid, K. R. Siefermann, F. P. Sturm, M. Swiggers, J. Ullrich, F. Weise, P. Zwart, C. Bostedt, O. Gessner, and A. F. Vilesov, Science **345**, 906 (2014).

[48] R. M. P. Tanyag, C. Bernando, C. F. Jones, C. Bacellar, K. R. Ferguson, D. Anielski, R. Boll, S. Carron, J. P. Cryan, L. Englert, S. W. Epp, B. Erk, L. Foucar, L. F. Gomez, R. Hartmann, D. M. Neumark, D. Rolles, B. Rudek, A. Rudenko, K. R. Siefermann, J. Ullrich, F. Weise, C. Bostedt, O. Gessner, and A. F. Vilesov, Struct. Dyn. **2**, 051102 (2015).

[49] P. Thaler, A. Volk, F. Lackner, J. Steurer, D. Knez, W. Grogger, F. Hofer, and W. E. Ernst, Phys. Rev. B: Condens. Matter Mater. Phys. **90**, 155442 (2014).

[50] E. Latimer, D. Spence, C. Feng, A. Boatwright, A. M. Ellis, and S. Yang, Nano Lett. **14**, 2902 (2014).

[51] S. Yang and A. M. Ellis, Rev. Sci. Instrum. **79**, 016106 (2008).

[52] Y. He, J. Zhang, and W. Kong, J. Chem. Phys. **144**, 084302 (2016).

[53] M. N. Slipchenko, S. Kuma, T. Momose, and A. F. Vilesov, Rev. Sci. Instrum. **73**, 3600 (2002).
[54] S. Yang, S. M. Brereton, and A. M. Ellis, Rev. Sci. Instrum. **76**, 104102 (2005).
[55] D. Pentlehner, R. Riechers, B. Dick, A. Slenczka, U. Even, N. Lavie, R. Brown, and K. Luria, Rev. Sci. Instrum. **80**, 043302 (2009).
[56] J. Zhang, Y. He, and W. Kong, J. Chem. Phys. **144**, 221101 (2016).

Chapter 3 Experimental setup II: Electron gun

3.1 Overall description of gas phase electron diffraction

Gas phase electron diffraction GED has had a history of over half a century.[1,2] It bridges accurate structural information with our understanding of the nature of chemical bonding and a wealth of molecular properties. A typical experimental setup for GED consists of three parts, as shown in Fig. 3.1: an electron gun to generate a high-energy monochromatic well-collimated electron beam, an inlet to introduce gas phase samples and a detector to image the patterns of diffracted electrons. All components are housed in high or ultrahigh vacuum (UHV), and the experiment can operate in either pulsed or continuous mode. For non-volatile compounds and to maximize the sample concentration in the electron beam, the inlet is typically placed in close proximity of the electron beam.[3,4] Traditionally the detector is a photographic plate, and after each exposure, the diffraction rings are read and digitized for data processing. Phosphor screens have also been used, with an enhanced digital camera located outside the vacuum chamber for data transfer. Image quality microchannel plates with phosphor screens are not preferred because of the high sensitivity of channel plates to the x-ray background of the electron source.

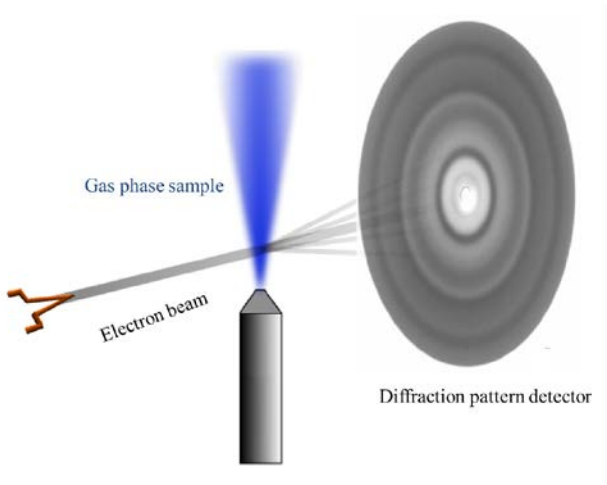

Fig 3.1 Schematic diagram of a GED setup.

3.2 Electron gun

An electron gun is the central device for electron diffraction. It consists of an electron emitter, either through thermionic emission or field emission (FE) or photoelectric effect, a current control grid (the Wehnelt grid), an anode, and focusing and beam steering elements. Although field emission offers the advantage of a higher emission current with a lower optical background,[5] thermionic sources are still popular because of their stability and ease in operation.[6] Photoelectric electron sources require additional lasers for operation, and they are only used in time resolved experiments.[7-9]

3.2.1 Electron source

3.2.1.1 Thermionic sources

In thermionic sources, electrons are produced by heating conductive materials. The outer orbital electrons of the filament can then overcome the work function barrier and escape. There are two main types of materials used in thermionic sources: tungsten and lanthanum hexaboride (LaB_6) crystal.

The most conventional electron source is a tungsten thermionic emitter, as shown schematically in Fig. 3.2. The filament is at the accelerating potential of the instrument and is heated to about 2800 K. The Wehnelt is biased by the potential drop across R_{bias}. The Wehnelt together with the grounded anode act as an electrostatic lens. Operation of this type of gun requires a vacuum level of ~10^{-5} Torr. The filament is relatively low cost and is easy to maintain. Higher filament heating temperatures can deliver higher beam currents, but the tradeoff is the decreasing lifetime due to thermal evaporation of the cathode material.

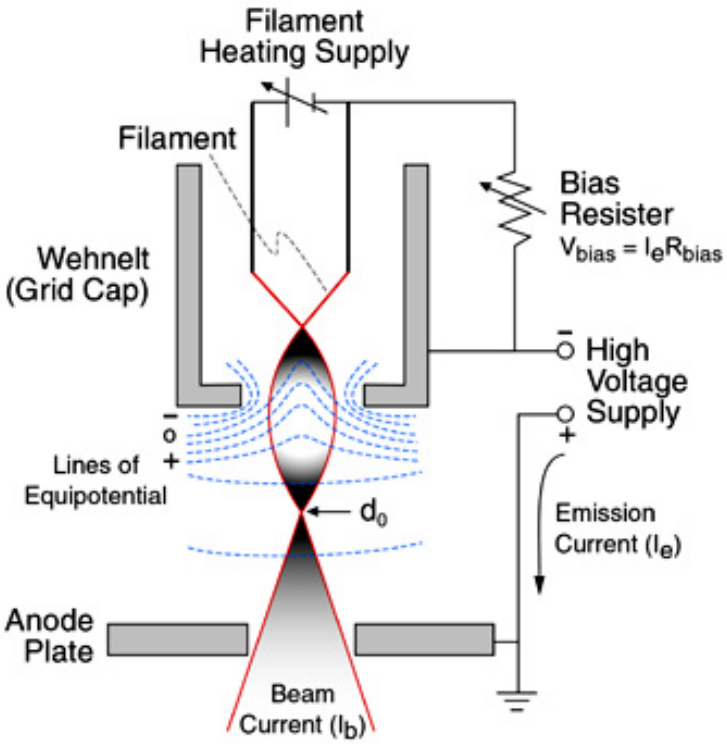

Fig. 3.2 Schematic diagram of a tungsten thermionic source.[6]

Another thermionic emission source is single crystal LaB_6 cut into a cone shape with a flattened point, as shown in Fig. 3.3. The single crystal LaB_6 is mounted directly on the carbon heater and heated to 1800 K. This subassembly is then mounted on a two-

pin ceramic base. With its low work function near 2.7 eV,[10] LaB_6 yields higher currents at lower cathode temperatures than tungsten, and typically LaB_6 cathodes exhibit 10 times the current and 50 times the lifetime of tungsten cathodes.[11] They have now replaced the conventional tungsten filament in many electron beam instruments. However, operation of this type of gun requires vacuum levels of ~10^{-7} Torr. In addition, LaB_6 is reactive at high temperatures, and it needs to be kept under high vacuum all the time. Once the vacuum breaks, the gun needs to be conditioned to heat off the contamination on the surface of the crystal.[12]

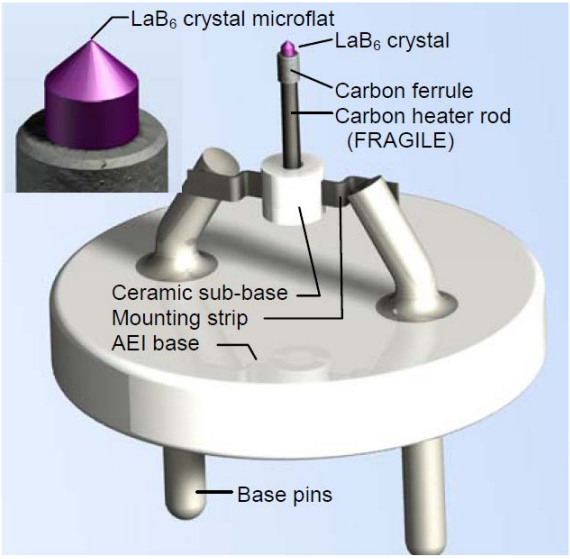

Fig. 3.3 LaB_6 cathode assembly

3.2.1.2 Field emission sources

The basic mechanism of field emission is that a high voltage applied between a pointed cathode and a plate anode can cause a current flow.[5] A field emission gun thus has a sharply pointed emitter that is held at several kilovolts negative potential relative to the first electrode. The potential gradient at the emitter surface is sufficient to cause electron emission. The emitter is usually made of single crystal tungsten

sharpened to a tip with a radius of about 100 nm. There are two different emitters in field emission guns: (1) cold field emission where the tungsten tip is operated at ambient temperature in UHV (<10^{-11} Torr); (2) thermal field emission where the emitter is coated with a layer of zirconium oxide, and limited heating is supplied to the cathode to assist electron emission. A thermal field emission source can operate at a poorer vacuum of <10^{-9} Torr.

Fig 3.4 shows the schematic diagram of a thermal field emission source: the 1st anode provides the extraction voltage to pull electrons out of the tip, and the 2nd anode accelerates the electrons.

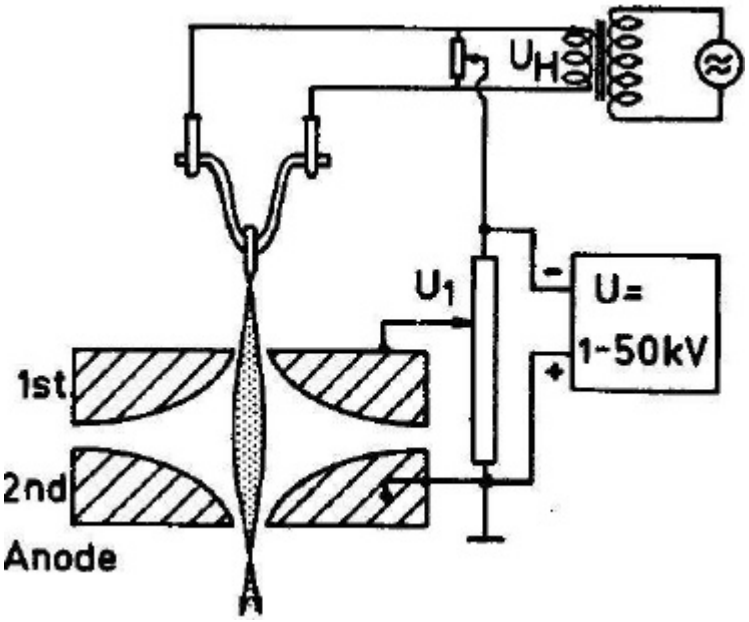

Fig. 3.4 Schematic diagram of thermal field emission source[5]

Advantages of field emission guns include smaller beam spot, higher coherence, and up to 3 orders of magnitude greater brightness than conventional thermionic tungsten emitters or LaB_6 filaments.[5,13] When used in electron microscopy, the signal-to-noise

ratio and spatial resolution are significantly improved. The emitter lifetime and reliability are also greatly increased compared with thermionic emitters. A major disadvantage of field emission guns is that it needs UHV. In addition, cost and maintenance are also challenging factors.

3.2.1.3 Photoelectric sources

For creating electron pulses short enough to study ultrafast processes of molecules, photoelectric sources are typically used. As shown in Fig. 3.5, a femtosecond laser is directed toward a back-illuminated silver photocathode to generate ultrashort electron pulses via the photoelectric effect. Many groups have developed the ultrafast electron diffraction apparatus to study ultrafast processes of molecules.[7,9,14-17]

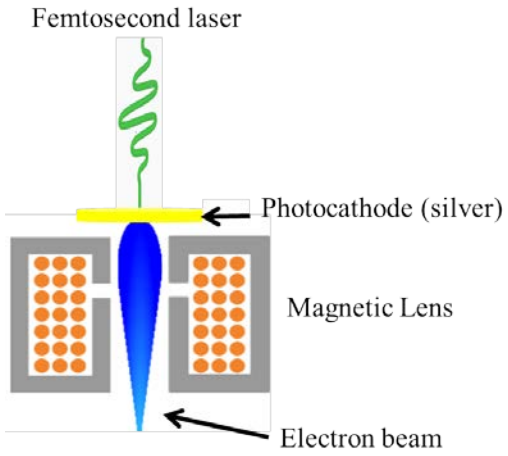

Fig. 3.5 Schematic diagram of photoelectronic source

3.2.2 Focusing lens

Coming out of the electron gun, high energy electrons need to be focused or collimated for diffraction. Hence all electron sources contain one or more focusing elements using electrostatic fields or electromagnetic fields. Electrostatic lenses are

simple to construct and operate, and have been used in cathode-ray tubes including television picture tubes.[18] For electron microscopes, however, because of the high voltages of the electron beam (over 20 keV), electrostatic lenses require high voltages, hence in modern electron guns, electromagnetic lenses are typically used. In addition, electromagnetic lenses have lower aberrations than electrostatic lenses.

An electromagnetic lens is formed by a solenoid. When an electric current goes through the lens coil, it induces a magnetic field, with field lines running roughly parallel to the axis of the coil and field strength proportional to the current. The soft iron pole pieces concentrate the field in between the gap region, enhancing the strength of the field, as shown in Fig 3.6.

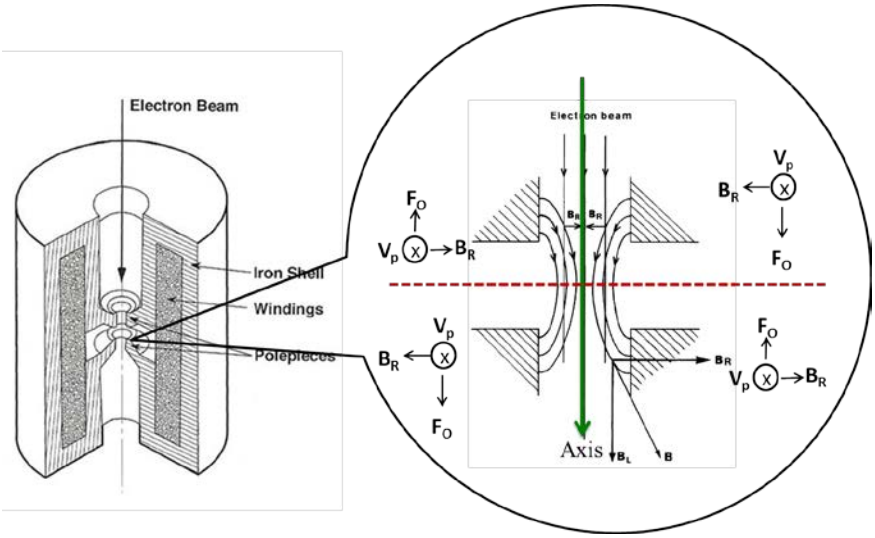

Fig. 3.6 Electromagnetic lens with magnetic field around the pole pieces. The labels V_p, B_r, and F_o are top views of the velocity.

The deflection force **F** experienced by an electron with charge -e and velocity **V** in a magnetic field **B** is given by the Lorentz force:

$$\mathbf{F} = -e\,(\mathbf{V} \times \mathbf{B}) \qquad (3.1)$$

The magnitude of the force is then given by $F= eBV \sin\theta$, where θ is the angle between **B** and **V**. Fig. 3.6 is a cross section of a typical magnetic lens showing the distribution of the magnetic field. It consists of a radial and longitudinal component $\mathbf{B_R}$ and $\mathbf{B_L}$, which vary along the length of the lens and in the plane perpendicular to the axis of the lens. An electron entering the lens axially ($V_p = V$, $V_R = 0$) from the top of the lens through the radial center of the aperture (green arrow in Fig 3.6), will experience no force from the field in the lens, since the only component of the field in this part of the lens is $\mathbf{B_L}$ ($B_R = 0$), which is parallel to **V**. For an electron travelling along the axis of the lens but not exactly through the radial center of the lens, i. e. at a displacement R from the center of the aperture, the situation is different. Such electrons will interact with the radial component of the field $\mathbf{B_R}$, since $\mathbf{B_R}$ is orthogonal to $\mathbf{V_p}$, and the electrons will experience a force $\mathbf{F_o}$ of magnitude eV_pB_R. This force is perpendicular to the plane of $\mathbf{B_R}$ and $\mathbf{V_p}$ and causes the electron to gain a velocity V_o perpendicular to B_R. The presence of V_o reduces the magnitude of V_p, and its interaction with B_L creates a force eV_oB_L, directing the electrons towards the radial center of the aperture. The result of the compounded effect of the magnetic field is that the electron, which is initially travelling axially with $V_p = V$ and $V_R = 0$, spirals towards the radial center of the lens as it travels toward the vertical center of the lens. The more off-center the incident electron is, the bigger is this converging force, since the magnitude of B_R reduces to zero at the center of the aperture. As shown in Fig 3.6, the lens is divided into four quarters by the axis and the middle of the pole piece. If viewed from the top of the lens, as shown by the four insets of the figure, $\mathbf{V_p}$ goes into the plane, $\mathbf{B_R}$ and $\mathbf{F_o}$ change directions after the electron passes the middle of the

polepiece. Hence the top half of the lens is of focusing effect, while the bottom half is defocusing. However, the focusing force of the top half is stronger than the defocusing effect of the bottom half of the lens, because the electrons are already traveling at a reduced radial position with a smaller value of $\mathbf{B_R}$ by the time they reach the middle of the lens. The net effect of the magnetic field is therefore focusing of the incident electrons.

Empirically, the focal length of an electromagnetic lens can be expressed as: $f = \frac{K V}{I^2}$, where f is the focal length, K is a constant based on the number of turns of the lens coil and the geometry of the lens, V is the beam accelerating voltage in units of keV, and I is the lens current. The focusing effect of a magnetic lens is therefore adjustable via the current on the lens coil. Changing of the energy of the electron beam also requires changing of the lens current to achieve the same focusing condition.

3.2.3 Beam steering and shaping

Electromagnetic lenses usually do not have perfect symmetry and the resulting electron beam may not be perfectly round in shape. In addition, the beam may not be at the right spot for diffraction. Beam Steering and shaping are therefore needed before the use of the electron beam.

Steering and shaping of an electron beam can be achieved using electromagnetic coils or electrostatic fields. The principle is the same as that of the lenses, but the field strengths are typically weaker and the fields are perpendicular to the optical axis in beam shaping and steering optics. Fig. 3.7 shows the top view of the field distribution, with the red arrows representing the directions of the forces on the electron beam. Fig. 3.7 (a) is a deflector for beam steering, which consists of a

uniform field to shift the beam. Fig. 3.7(b) is a stigmator for beam shaping where electrons experience forces from four directions: compression or elongation in the plane perpendicular to the optical axis changes the ellipticity of the electron beam. Magnetic deflection introduces less distortion than electrostatic deflection. However, electrostatic deflection can achieve much higher speeds since the inductance of the magnetic deflection coils limits their frequency response.

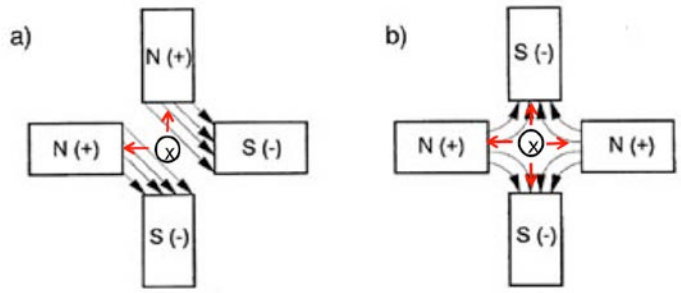

Fig. 3.7 Schematic drawing of the magnetic/electrostatic field distribution in beam steering and shaping optics.

3.2.4 Operational parameters of our electron gun

Fig. 3.9 is a schematic block diagram showing the interior components of the gun used in our experiment (Kimball Physics, EGPS-6210B). The electron gun consists of three major elements: triode, lens, and XY deflection/shaping coils. The triode includes the cathode, Wehnelt (grid), and the grounded anode. Electrons are first 'evaporated' from a hot cathode (LaB_6) and are accelerated to the full kinetic energy outside the Wehnelt grid. The electron beam is further focused, positioned and shaped with an electromagnetic lens (I_{LS}) and the beam shaping coils (I_X and I_Y).

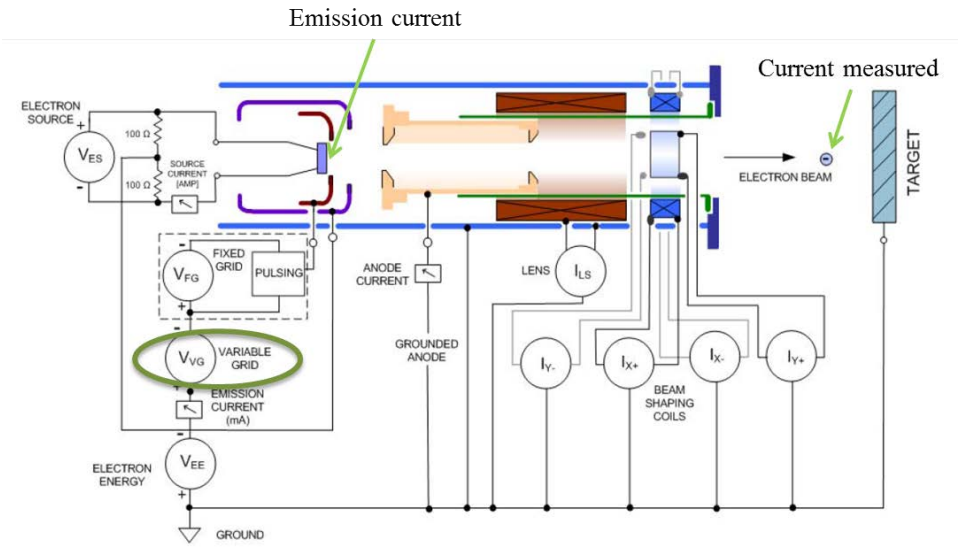

Fig. 3.8 A block diagram of the electron gun used in our setup with the electrical connections of the power supplies and gun elements (adapted from Kimball Physics, EGPS-6210B)

In our experiment of ss-EDI, we have two conditions for the electron beam: (1) to obtain a sharp diffraction image, the electron beam needs to be focused on the phosphor screen, and (2) to achieve effective laser alignment, the beam size in the diffraction region needs to be minimized. Obviously one lens cannot satisfy both requirements, and a second electromagnetic lens is needed, as shown in Fig. 3.9. We used the first condenser lens from a surplus transmission electron microscope (TEM, Zeiss EM-10) to act as the second lens C2. Due to resistive heating of the lens coil, cooling water is necessary to maintain a stable operational temperature. The top lens C1 (from Kimball) converges the cone of the electron beam to a spot below it, but before the cone flares out again, it is converged back by a second C2 (added) lens, which then focuses the beam down onto the phosphor screen. A crossover is therefore

formed between C1 and C2. Two sets of beam steering plates, biased at static voltages, are also added at the exit of C2 for directing the electron beam to the diffraction region.

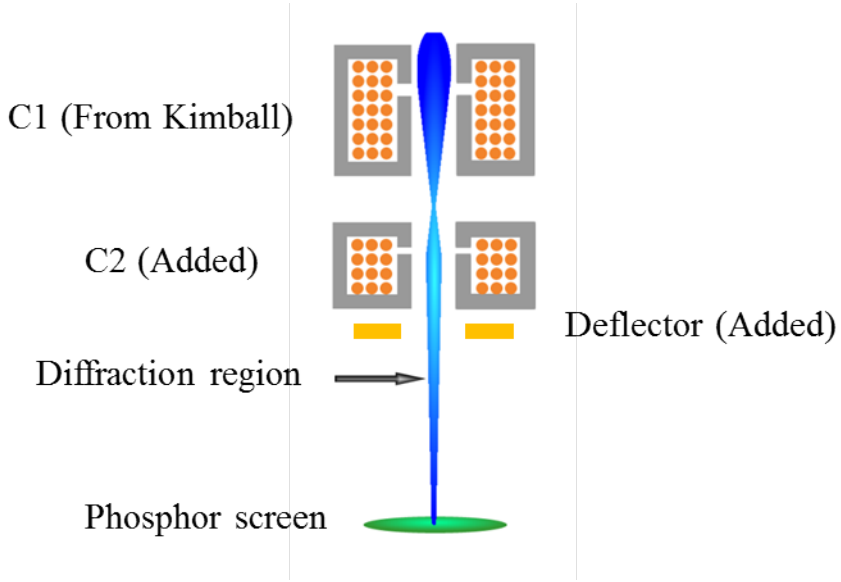

Fig. 3.9 The electron beam in SS-EDI.

In our diffraction experiment, the energy of the electrons was set at 40 keV. The grid (green circle in Fig. 3.8) was set at 220 V and the beam current was 1.4 mA. The first lens C1 was operated at 0.928 A and C2 at 0.778 A, resulting in a beam size in the diffraction region to about 300 μm. The voltages on the deflector electrodes were -50 V to50 V.

3.2.5 Beam current measurement

The number of electrons impinging on the sample in the diffraction region directly affects the signal-to-noise ratio of the experiment, hence an important operational parameter is the beam current in the diffraction region. Here the beam current is not identical to the emission current (shown in Fig. 3.8), which is the total current that leaves the cathode source and goes to ground through the diffraction path and all other possible paths of losses. In the process of traveling down from the electron gun

to the phosphor screen, some electrons can land on the lens elements or steering electrodes. Hence the beam current in the diffraction region is less than the initial emission current, shown in Fig. 3.8 as ‘Current measured’.

Measurements of diffraction beam currents are typically achieved using a Faraday cup.[19] A Faraday cup is a cylinder made of conducting materials. To further limit production of secondary electrons, we have coated the interior and exterior of the cup with graphite. Electrons hit inside the tube and produce a current. The small input opening of a Faraday cup is to limit the interference of escaped direct incident electrons, secondary electrons, and x-ray photons. The cup is wired to a resister, converting the current to voltage shown on an oscilloscope. Faraday cups have no amplification effects, hence they are not as sensitive as electron multiplier detectors. However, Faraday cups can be used for accurate measurements of beam currents because of the direct relation between the measured current and the number of charged particles.

We have two Faraday cups in our experimental setup to measure the electron beam current at two positions: in the diffraction region and at the phosphor screen. The one in the diffraction region was used for alignment of the electron gun, particularly after each filament change or each major realignment event, when the beam current cannot reach the Faraday cup down at the phosphor screen. The Faraday cup on top of the phosphor screen prevents the phosphor screen from getting burnt by the intense un-diffracted main electron beam.

3.2.6 Beam size measurement

The size of the electron beam in the diffraction region directly determines the size of the alignment laser and hence the degree of alignment. We have invented a convenient method to determine the beam size using a linear variable differential transducer (LVDT, Omega, LD340-6.0). As shown in Fig. 3.10 (a), the device also contains a picomotor (Newport 8302-UHV) to drive the LVDT, and a shuttle carrying a cutting edge.[20] The device is contained in a vacuum chamber, and the electrical supply and readout of the transducer are routed out of the vacuum chamber via vacuum feedthroughs. The LVDT allows position measurement with a precision determined by the voltage readout. Our model Omega LD340-6.0 generates a voltage reading of 1 V with a traveling distance of 500 μm. The precision of the measurement can thus be 0.5 μm if the voltage can be read with a precision of 1 mV. Fig. 3.10 (b) shows the transmission profiles of a focused laser beam, measured using the LVDT device. The light source was a helium-neon laser with an optical lens placed in the beam path. A light sensitive photodiode was used as the intensity detector of the laser beam. Three measurements at three different locations relative to the lens were performed. The two traces obtained at 4 inches and 6 inches from the lens were almost the same, implying that the focal point of the laser beam should be around 5 inches. The measurement at 5 inches resulted in the sharpest change in transmission, implying a small beam size.

The total electron beam current (maximum value) was first measured by passing the whole beam to the Faraday cup. As the beam cutter traverses the path of the electron

beam, the transmission would be changed. We record the voltage reading from the LVDT and the corresponding current reading on the Faraday cup. Since an electron beam does not have sharp edges, we use the $1/e^2$ width to define the beam diameter, which is the distance between the two points that are 0.135 times of the total beam current. For example, the LVDT read -0.555 V and -1.093 V at 86.5% of the total beam current, hence the approximate beam size is 500 μm/V × 0.54 V = 270 μm.

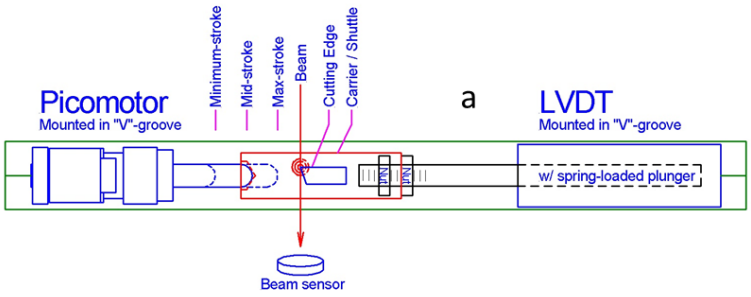

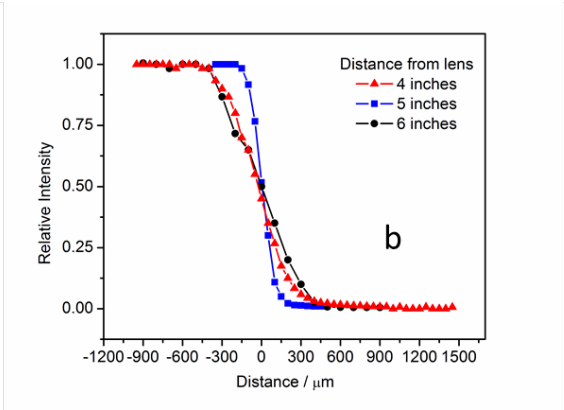

Fig. 3.10 (a) Schematic drawing of the LVDT device
(b) Transmission profiles of a focused laser beam using the LVDT device

3.3 Imaging system

3.3.1 Phosphor screen

Phosphor screens are used as detectors in almost all GED experiments, because of their high photon yields upon impact with high energy electrons. Typical conversion

factors of phosphor screens are between 20 and 200 photons per electron, depending on the type of phosphor screen and the kinetic energy of the electrons.[21] To increase light efficiency and reduce stray light transmission, phosphor screens in GED are normally coated with an aluminum layer on top, and this conductive overlay also helps avoid charge accumulation on the screen. In some cases, the phosphor screen also acts as the vacuum barrier, and the image is directly coupled to an outside camera via fiber optics. Other times, an additional optical grade window is used to transfer the image to the outside camera.

There are three important considerations in choosing a phosphor screen: efficiency, decay time and spatial resolution. The two mostly used phosphor screens are P43 (emission wavelength: 360 nm-680 nm, maximum at 545 nm) and P46 (emission wavelength: 490 nm-620 nm, maximum at 530 nm). The P43 phosphor screen has a higher efficiency and higher spatial resolution due to its smaller grain size, but it has a long decay time. For faster applications, such as when the interframing time is on the order of 500 ns, P46 is necessary to avoid ghost images from the previous exposure. In our experiment, we use P43 (Beam Imaging Solutions, P43 40 mm) since our typical repetition rate is 10 Hz, and the interval between images leaves enough time for the fluorescence to decay. The Faraday cup and phosphor screen assembly is shown in Fig. 3.11.

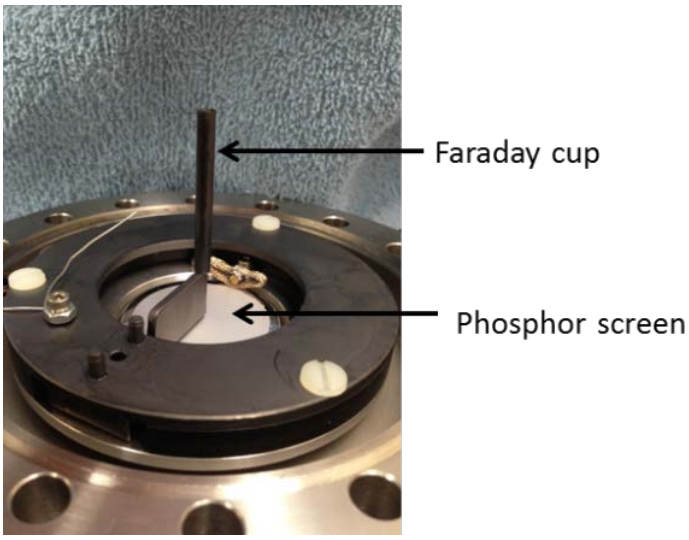

Fig 3.11 Faraday cup and phosphor screen assembly

3.3.2 Camera

Immediately below the phosphor screen outside the vacuum chamber is the camera system, which converts the optical image on the phosphor screen to a digital matrix and sends it to the computer. In our experiment, an Electron Multiplying Charge Coupled Device (EMCCD) camera (Andor Technology, iXON Ultra) is used to record the diffraction pattern. The camera is cooled down to -80° C to reduce thermal noise, and it is operated at a resolution of 512 × 512 pixels at 10 or 14 Hz.

This EMCCD camera is capable of detecting single photon events whilst maintaining high quantum efficiency, achievable via a unique electron multiplying structure built into the sensor. Unlike a conventional CCD, an EMCCD camera is not limited by the readout noise of the output amplifier. It relies on a solid state electron multiplying (EM) register at the end of the normal serial register for magnification before readout.

The gain of the EM is controlled by higher than typical CCD clock voltages (up to 50 V), and the resultant gain is exponentially proportional to the voltage.

3.3.3 Vacuum requirement

The ambient air in the diffraction chamber contribute to the background in an diffraction image and needs to be removed. One straightforward method is to improve the vacuum in the diffraction chamber. We used: (1) two turbomolecular pumps to keep the base pressure of the diffraction chamber at 5×10^{-8} Torr; (2) baking with heating belts to reduce the water residue on the chamber wall, and (3) liquid N_2 cooled block inside the chamber to further improve the vacuum to 1×10^{-8} Torr during diffraction. With these measures, the vacuum level can reach 7×10^{-9} Torr.

The level of vacuum in the pickup chamber is also of concern, to prevent contamination of the droplet beam by foreign species other than the intended dopant. We used two turbomolecular pumps to reach a base pressure of 2×10^{-7} Torr.

3.4 Data processing

The diffraction pattern from the doped droplets is a combination of diffractions from the dopant molecules, the helium jacket outside the dopant molecule, undoped helium droplets, and background from the residual gas in the diffraction chamber. To magnify the structural information, the *sM(s)* profile removes all contributions from atoms and background, and the remaining molecular interference is further magnified by the momentum transfer *s:*

$$sM(s) = \frac{A_s \cdot I_{total}(s) - A_d \cdot I_{droplet}(s) - A_b \cdot I_{background}(s)}{I_{T,at}(s)} \cdot s - s \qquad (3.2)$$

Where s is defined as $\frac{4\pi}{\lambda}\sin\frac{\theta}{2}$, and $I_{total}(s)$, $I_{droplet}(s)$, and $I_{background}(s)$ are intensities from the experiment of doped droplets, pure droplets, and background, A_s, A_d and A_b are the corresponding fitting parameters, $I_{T,at}(s)$ is the theoretical diffraction intensity from the atoms of the dopant molecule. The values of $I_{total}(s)$, $I_{droplet}(s)$, and $I_{background}(s)$ are from the experiment directly obtained from the diffraction image, and $I_{total}(s)$ and $I_{droplet}(s)$ are obtained under the same experimental conditions with and without the sample.

The following illustrates the necessary steps for image processing. Fig 3.12 (a) shows the raw diffraction image from electron diffraction of CBr_4 doped in superfluid helium droplets. The shadow of the Faraday cup, its support arm, and blemishes on the phosphor screen can be seen. Fig. 3.12(b) shows the processed image by removing the dashed region in Fig. 3.12 (a), filling it with data from the opposite side of the same image, taking an average over all four quadrants of the picture, and applying the Wiener filter on the resulting image for noise removal. The Wiener2 function in Matlab was used and the block parameter was 4 × 4 pixels (the camera has 512 × 512 pixels). Other filter methods have also been tested but with no observable differences in the resulting *sMs* curve. Fig. 3.12 (c) is the difference between the image of Fig 3.12 (b) and a background image taken alternately with the droplet beam and processed with the identical procedure, and the radial profile from Fig. 3.12 (c) leads to $I_{total}(s)$. Similar steps were applied to get $I_{droplet}(s)$. Based on comparisons

with the theoretical $sM(s)$, we performed multilinear regression to obtain the coefficients of each component A_s, A_d and A_b. After the multilinear regression, reverse Fourier transform of *sM(s)* results in the pair correlation function that peaks at the interatomic distance of each correlated pair:

$$f(r) \propto \int_0^{s\_max} sM(s) \cdot \sin(sr) \cdot \exp(-k_d s^2)\, ds \qquad (3.3)$$

where k_d is a damping factor to account for the limited range of s values determined by the size of the detector.

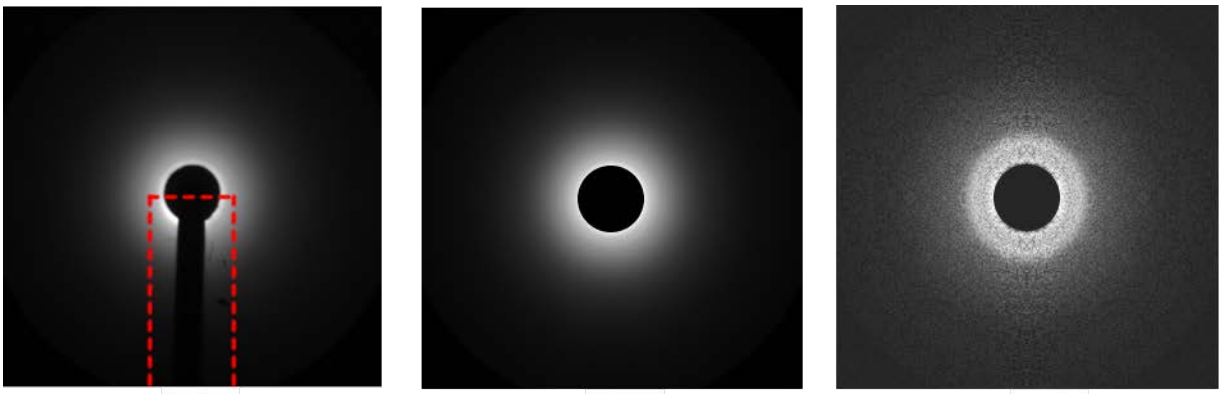

Fig. 3.12 Diffraction images from CBr_4 doped helium droplets. (a) Raw image from CBr_4 doped helium droplets, (b) Wiener filtered regenerated image from (a) by refilling the portion inside the dashed box with data from the opposite side of the box and averaging over all four quadrants, (c) difference image between PV on and PV off.

3.5 Auxiliary components

3.5.1 The 6-position wheel

The experimental apparatus requires considerable tuning and alignment efforts, most of which require a high vacuum condition. Adjustment under vacuum is difficult, and the venting and pumping processes also take time. Moreover, some parameters, such as the electron gun and laser, are unstable enough that daily tuning is necessary. Given these constraints, it is necessary to have a flexible diagnostic system that can be temporarily used without breaking the vacuum. For this purpose, we have designed a 6-position rotatable wheel inside the diffraction chamber, switchable via rotation of a cajon feedthrough. Fig. 3.13 shows the drawing of the wheel. Calibration and alignment components can be mounted on the wheel, and each can be rotated into and out of the electron beam when necessary.

The wheel was located 2.5 cm below the diffraction spot, supported from the top of the diffraction chamber. Its axis of rotation was off center so that one of its six positions along the edge could be rotated into the path of the electron beam. Each position on the wheel is a hole of 2.5 cm dia. or 0.6 cm dia., inlaid with a variety of components, including LVDT and picomotor to control beam cutter and measure the electron beam size; a diffraction bit containing an aperture of 6 mm dia. facing the droplet beam and a graphite aperture (2 mm dia.) located 5 mm above the diffraction region to limit the optical image of the electron beam; a standard TEM calibration sample polycrystalline aluminum (Electron Microscopy Sciences, Catalog #80044) for calibration of the camera length and wavelength of the system; a diffraction bit with a fixed needle for diffraction with diffused gaseous samples without helium

droplets. Limited by the available space on the wheel, not all necessary components can co-exist in the chamber. Hence depending on the stage of the experiment, occasional venting of the chamber is still necessary to accommodate different components.

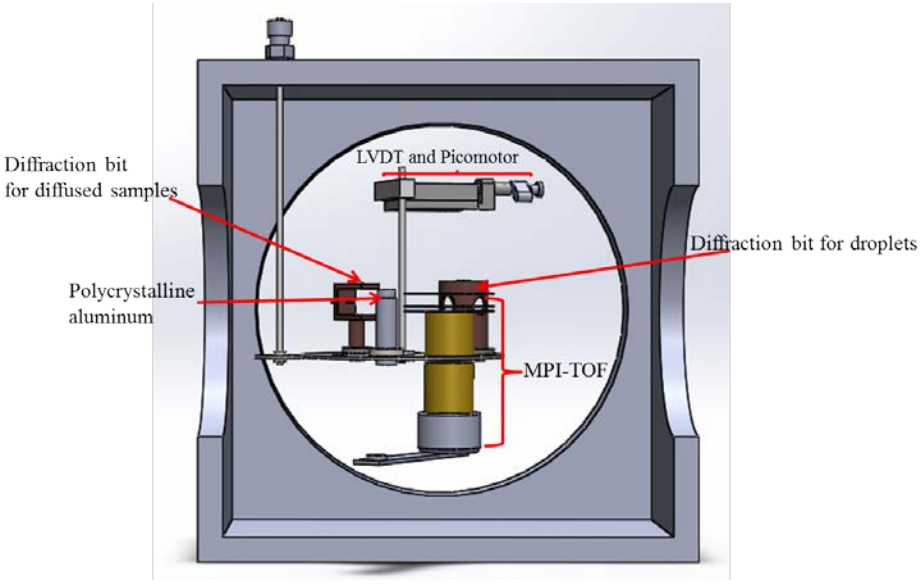

Fig. 3.13 The 6-position rotatable wheel in the diffraction chamber and the components on it

3.5.2 Calibration of camera constant

To obtain the actual interatomic distance from a diffraction pattern using electron diffraction, we need to know the wavelength of the electron and the camera length – the camera constant.[22] Camera length is the distance from the diffraction region to the projected image on the phosphor screen, represented by L in Fig. 3.14. The Bragg angle (diffraction angle) 2θ is typically small due to the short wavelength of an electron beam (0.06 Å at 40 KeV), so Bragg's Law reduces to $2d\theta \approx \lambda$ in this case. From trigonometry, $2\theta \approx R/L$, hence we can establish a relation $Rd \approx L\lambda$. The factor $L\lambda$ is often referred to as the camera constant and is usually calibrated by reference to

a known substance with well-defined diffraction spacings. One of the standard samples for calibration is evaporated polycrystalline aluminum on a 3 mm TEM grid.

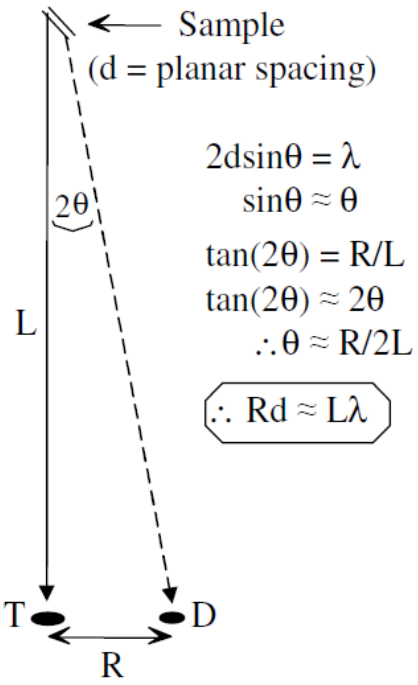

Fig. 3.14 Geometry in electron diffraction

The polycrystalline aluminum standard was placed at the diffraction spot, sitting on the 6-position rotatable wheel, as shown in Fig. 3.13. Intense and sharp diffraction rings could be observed and assigned, as shown in Fig. 3.15. To avoid burning of the phosphor screen, the electron beam current was tuned down to 50 μA in this calibration experiment.

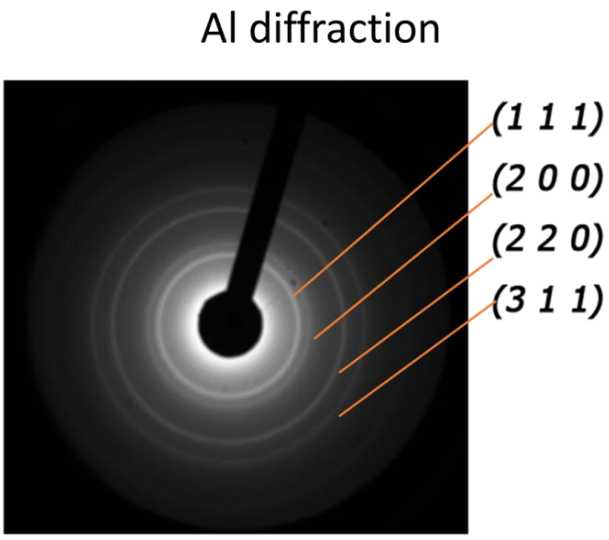

Fig. 3.15 Calibration image of polycrystalline aluminum with assignment of lattice planes

Table 3.1 Calibration of camera constant using polycrystalline aluminum

Miller Indices (hkl)	Lattice Spacing d (Å)	Pixels from the center (N)	Momentum transfer (S)	Pixles/S
1 1 1	2.338	81	2.687	30.140
2 0 0	2.024	93	3.104	29.958
2 2 0	1.431	133	4.391	30.291
3 1 1	1.221	156	5.146	30.315

To determine the camera constant, we first determine the number of pixels N from the center for each diffraction ring. The radius of the phosphor screen is 2.0 cm, covered by 240 pixels in the image, hence the radius of the ring R is N×2.0/240 cm. From the assignment of the Miller Index of the ring, the corresponding Lattice Spacing d can be found from online technical notes[23]. Thus the camera constant $dR = d \times N \times \frac{2.0\ cm}{240} \times \frac{10^8 Å}{cm} = 1.6 \times 10^8 Å^2$. The corresponding value of the momentum transfer *s* for the diffraction ring can then be calculated by $\frac{4\pi}{\lambda}\sin\frac{\theta}{2} = \frac{4\pi}{\lambda}\frac{R}{2L} = \frac{2\pi R}{dR} = \frac{2\pi}{d}$. In

practice, another useful quantity in image analysis is *Pixel/s*, which can be calculated by $\frac{N}{s}$. This value makes it easier in identifying features (such as bumps or valleys) in the diffraction pattern and in comparison with simulations.

3.5.3 Diffraction bit

The diffraction bit is designed for defining the diffraction region of doped droplets, and it is shown in Fig. 3.13. The entrance and exit apertures along the droplet beam direction select the center of the droplet beam, and the 2 mm diameter graphite aperture on the top of the bit is used to filter out the light emitted from electron gun filament. Another set of opposite holes is designed for passing an alignment laser.

3.5.4 MPI-TOF

The purpose of the MPI-TOF is to characterize the doping condition of the droplets.[24,25] Its principle of operation is non-resonant multiphoton ionization. The spectrometer is a standard Wiley-Maclaren type.[26] As shown in Fig. 3.16, the gap between the two extraction electrodes was 9 mm to accommodate the whole droplet beam, and the gap between electrode II and the flight tube was only 3 mm. The flight tube was 6 cm long and was grounded.

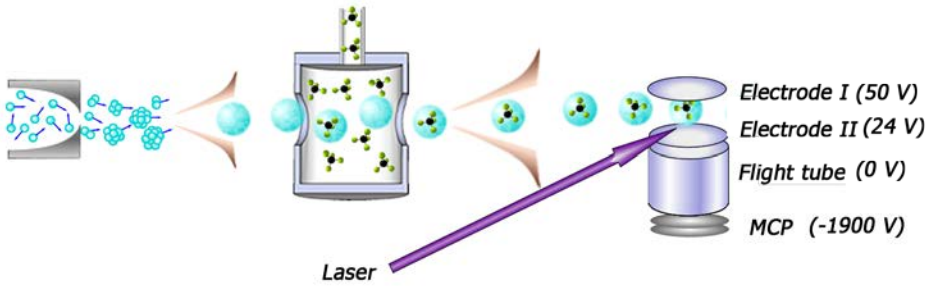

Fig 3.16 Schematic diagram of MPI-TOF setup

The electrodes and flight tube were attached to the rotatable wheel connected to a Cajon vacuum feedthrough, and they could be moved out of the way of the droplet beam by rotating the rod connected to the wheel. The MCP detector was mounted on a slide movable on a rail system, and it could be retracted to a corner of the chamber using another Cajon feedthrough. See more details in chapter 3 and chapter 5.

The laser is able to ionize almost everything except helium, thus it is not useful in charactering pure droplets. However, it is sensitive to dopants and other residual gases. To illustrate its performance, the MPI spectrum of CBr_4 doped droplets is shown in Fig. 3.17. The lower panel includes the two traces recorded when the droplet PV was on and off: when the PV is off, it is effectively a residual gas analyzer. The upper panel is the net difference, representing effects due to solely doped CBr_4.

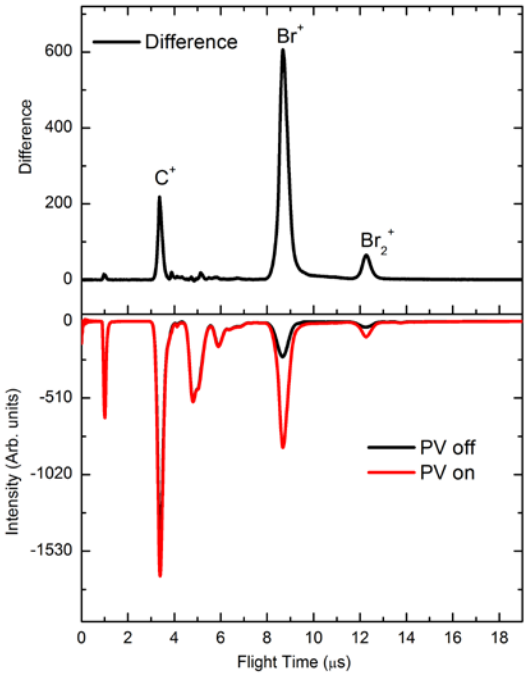

Fig. 3.17 MPI spectrum of CBr_4

3.5.5 Diffraction bit for diffused samples

Although the focus of this thesis is diffraction of molecules embedded in superfluid helium droplets, reference diffraction images from pure gas phase samples are sometimes helpful for comparison and analysis. For this purpose, we constructed a special bit on the 6-position wheel to route pure gas phase samples into the diffraction region. A 2 mm diameter graphite aperture on top of the bit is also used to filter out the light emitted from electron gun filament. The sample was introduced into the rubber tube connected to a needle, hence diffused sample emits from the tip of the needle into the electron beam. The needle tip is quite sharp and located about 2 mm away from the electron beam, to ensure a high particle density and a limited spreading in the electron beam.

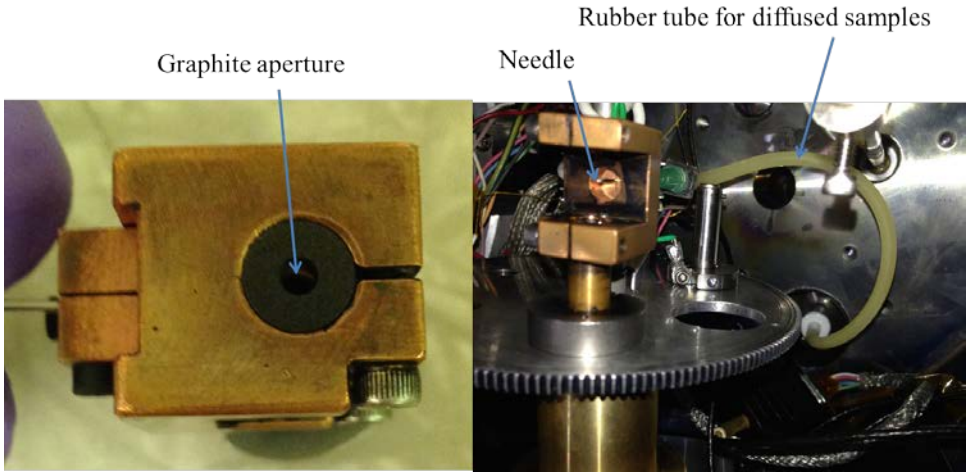

Fig. 3.18 Diffraction bit for diffused samples: the left is the top view, and the right is the side view.

3.5.6 **Alignment using the LVDT cutter system**

There are three beams involved in SS-EDI: electron beam, helium droplet beam and laser beam. The droplet path is defined from the skimmer through the center of the diffraction chamber, and the droplet beam diverges into a cone of 1°. Thus alignment

with the droplet beam is typically not a concern for either the electron beam or the laser beam. Alignment between the electron beam and the laser beam for orientation, however, is critical. We can use the LVDT - cutter system to align the electron beam (z direction) and laser beam (y direction) in one direction by translating the cutter along the x-direction. We can first record the reading of the LVDT when the electron beam is cut to half of its total current, and then adjust the laser beam so that half of its power passes through the cutter at the same reading of the LVDT.

3.6 Timing Control

The apparatus is controlled by an interface card (DAQ NI-PCIe-6320), which sends out a master clock at 14 Hz, limited by the data acquisition rate of the camera. The master clock triggers the electron gun and the camera, and it produces a 7 Hz trigger to the droplet pulsed valve and to an input channel of the interface card. Hence the effective repetition rate of the overall experiment is 7 Hz, while the data acquisition rate of the camera is 14 Hz. The relative timing among the beams is controlled by delay generators (Stanford Research, DG535). A LabView program reads the image after each electron pulse and accumulates the droplet image (PV on) and background image (PV off) separately based on the input channel of the interface card. This “toggle” mode of operation effectively removes the contribution from diffused bare sample into the diffraction region, thus any molecular diffraction should be related to the sample in the droplet beam. The partial pressure of the doping sample in the doping chamber remained the same with and without the droplet beam, hence the degree of diffusion should remain the same independent of the droplet beam. The net difference in diffraction signal recorded with and without the droplet beam is

therefore the net contribution of all droplets, with or without dopant. The timing diagram is shown in Fig. 3.19.

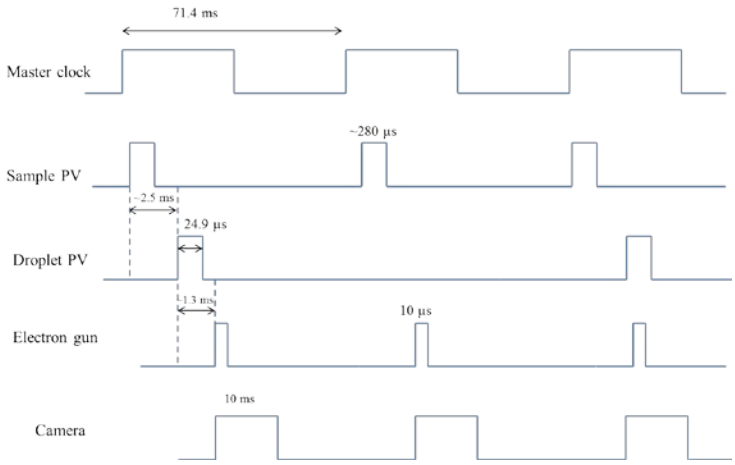

Fig. 3.19 Timing diagram

If the sample pulsed valve is used, there are two critical timing searches: the timing between droplet and sample pulsed valves (see section 2.4.2) and timing between ionization laser and droplet pulsed valve (see section 5.3.2). In the presence of a velocity slip and with pulsed sampling, this method offers a path to size selection of the dopant cluster for electron diffraction. For example, in our ferrocene experiment, to achieve mostly singly doped droplets, we first find the timing of the laser pulse based on the diagnostic signal at a low doping pressure, and this time setting eliminates contributions of larger-sized droplets and dopant clusters. Then we increase the doping pressure and maximize the dopant related signal. Multiply-doped large droplets are too slow to be sampled by the laser pulse, and small droplets that survive the doping region should be mostly singly doped. The net result is a high concentration of singly doped droplets sampled by the pulsed electron gun.

3.7 References

1 P. Allen and L. E. Sutton, Acta Crystallographica 3, 46 (1950).
2 L. O. Brockway, Rev. Mod. Phys. 8, 231 (1936).
3 K. Hedberg and L. Hedberg, Science 254, 410 (1991).
4 A. Haaland, in *Gas-Phase Electron Diffraction* (Springer, 1975), pp. 1.
5 S. Fukuhara, H. Todokoro, and Y. Sakitani, (Google Patents, 1981).
6 D. B. Williams and C. B. Carter, in *Transmission Electron Microscopy: A Textbook for Materials Science* (Springer US, Boston, MA, 2009), pp. 73.
7 J. C. Williamson, J. Cao, H. Ihee, H. Frey, and A. H. Zewail, Nature 386, 159 (1997).
8 H. Ihee, V. A. Lobastov, U. M. Gomez, B. M. Goodson, R. Srinivasan, C.-Y. Ruan, and A. H. Zewail, Science 291, 458 (2001).
9 B. J. Siwick, J. R. Dwyer, R. E. Jordan, and R. D. Miller, Science 302, 1382 (2003).
10 H. Yamauchi, K. Takagi, I. Yuito, and U. Kawabe, Applied Physics Letters 29, 638 (1976).
11 L. Swanson and T. Dickinson, Applied Physics Letters 28, 578 (1976).
12 J. D. Verhoeven and E. D. Gibson, Journal of Physics E: Scientific Instruments 9, 65 (1976).
13 A. Crewe, D. Eggenberger, J. Wall, and L. Welter, Review of Scientific Instruments 39, 576 (1968).
14 J. C. Williamson, M. Dantus, S. B. Kim, and A. H. Zewail, Chem. Phys. Lett. 196, 529 (1992).
15 R. Li, C. Tang, Y. Du, W. Huang, Q. Du, J. Shi, L. Yan, and X. Wang, Review of Scientific Instruments 80, 083303 (2009).
16 J. Cao, Z. Hao, H. Park, C. Tao, D. Kau, and L. Blaszczyk, Applied Physics Letters 83, 1044 (2003).
17 A. Janzen, B. Krenzer, O. Heinz, P. Zhou, D. Thien, A. Hanisch, F.-J. M. z. Heringdorf, D. v. d. Linde, and M. H. v. Hoegen, Review of Scientific Instruments 78, 013906 (2007).
18 E. Harting and F. H. Read, (1976).
19 K. Brown and G. Tautfest, Review of Scientific Instruments 27, 696 (1956).
20 J. Beckman, W. Kong, V. G. Voinov, and W. M. Freund, Patent No. US20150168318A1 (2015).
21 Y. Glinec, J. Faure, A. Guemnie-Tafo, V. Malka, H. Monard, J. P. Larbre, V. D. Waele, J. L. Marignier, and M. Mostafavi, Review of Scientific Instruments 77, 103301 (2006).
22 J. McCaffrey and J. M. Baribeau, Microscopy research and technique 32, 449 (1995).
23 https://www.tedpella.com/technote_html/619%20TN.pdf.
24 Y. He, J. Zhang, Y. Li, W. M. Freund, and W. Kong, Rev. Sci. Instrum. 86, 084102 (2015).
25 Y. He, J. Zhang, and W. Kong, J. Chem. Phys. 144, 084302 (2016).
26 W. C. Wiley and I. H. McLaren, Rev. Sci. Instrum. 26, 1150 (1955).

Chapter 4 Facile time-of-flight methods for characterizing pulsed superfluid helium droplet beams

Yunteng He, Jie Zhang, Yang Li, William M. Freund, and Wei Kong*

Department of Chemistry, Oregon State University, Corvallis, OR 97331

Review of Scientific Instruments

1305 Walt Whitman Road Suite 300

Melville, NY 11747-4300

86, 084102 (2015)

*Corresponding author, 541-737-6714, wei.kong@oregonstate.edu

Abstract

We present two facile time-of-flight (TOF) methods of detecting superfluid helium droplets and droplets with neutral dopants. Without an electron gun and with only a heated filament and pulsed electrodes, the electron impact ionization TOF mass spectrometer can resolve ionized helium clusters such as He_2^+ and He_4^+, which are signatures of superfluid helium droplets. Without ionizing any helium atoms, multiphoton non-resonant laser ionization of CCl_4 doped in superfluid helium droplets at 266 nm generates complex cluster ions of dopant fragments with helium atoms, including $(He)_nC^+$, $(He)_nCl^+$ and $(He)_nCCl^+$. Using both methods, we have characterized our cryogenic pulsed valve – the Even-Lavie valve. We have observed a primary pulse with larger helium droplets traveling at a slower speed, and a rebound pulse with smaller droplets at a faster speed. In addition, the pickup efficiency of dopant is higher for the primary pulse when the nozzle temperature is higher than 13 K, and the total time duration of the doped droplet pulse is only on the order of 20 μs. These results stress the importance of fast and easy characterization of the droplet beam for sensitive measurements such as electron diffraction of doped droplets.

4.1 Introduction

Superfluid helium droplets provide an ultra-cold non-interacting medium for studies of dopants at 0.37 K, and helium nanodroplet isolation spectroscopy has proven a versatile technique for many forms of molecular spectroscopy[1-3]. It has been applied in studies of structures and dynamics of novel systems such as biomolecules, free-radicals, metal clusters, and molecular clusters[4-8]. However, the generation of superfluid helium droplets and confirmation of dopant uptake are still challenging for many new laboratories venturing into this field. For large droplets containing more than millions of helium atoms, Rayleigh scattering can be used to confirm the existence of droplets and to determine the timing of a pulsed beam[9]. However, for effective Rayleigh scattering, an ultraviolet (UV) light source is strongly preferred and efforts in background light reduction are necessary. Fast ion gauges have also been used to confirm the existence of droplets, but the lack of mass information prevents knowledge of the doping status of a droplet beam. A widely used and effective method for detecting both pure and doped droplets is a quadrupole mass spectrometer with a hot filament for electron impact ionization[10-13]. Unfortunately, the cost of a standard quadrupole mass spectrometer is considerable. Several groups have employed a pulsed collimated electron beam coupled with a time-of-flight mass spectrometer (TOF) for studies of pure droplets and doped droplets[14,15]. However, a pulsed collimated electron beam is not easily available, and the need for deflectors to correct the off-axis velocity of the ions further complicates the system. Moreover, to accelerate the electrons for ionization, a transverse field perpendicular to the flight axis is typically used, which could further exacerbate the off-axis velocity of the thus

produced ions in the ionization region. Using photoionization, either with a single photon from a synchrotron source or multiple photons in the nanosecond or femtosecond domain, spectroscopic studies of pure droplets and doped droplets have been reported[16-19]. For the purpose of diagnosis, however, many of the light sources are impractical or overly expensive.

Here we present two facile approaches to detect helium droplets and droplets with neutral dopants using time-of-flight technology. First, we use a heated tungsten filament as an electron source with a pulsed grid for electron impact ionization (EI-TOF). The acceleration field for the ionizing electrons is in-line with the flight axis and in-line with the droplet beam. Consequently, the mass resolution is limited, but helium cluster ions including $He_2^+$and He_4^+ can still be separated. This apparatus is easy to operate and economical to build. It requires no deflectors and no collimated electron beam, and it can measure the free drift time of the neutral droplet beam. Second, we use the 4th harmonic of a nanosecond Nd:YAG laser for non-resonant multiphoton ionization (MPI-TOF). The MPI-TOF is miniature in size but has a better mass resolution than the EI-TOF. With several millijoules at 266 nm from a small Nd:YAG laser, the MPI-TOF is blind to pure droplets, but it can resolve complexes formed between fragments of neutral dopants with helium. Using CCl_4 as a sample dopant, we also report some differences between our mass spectra and those from previous reports of laser ionization obtained under much higher laser intensities. The two different TOF mass spectrometers are in different locations along the droplet beam, which enable the comparison of timing and doping conditions. This capability further reveals the existence of a rebound pulse from our droplet source containing

smaller clusters with a faster speed. Doping is more effective for larger sized clusters, hence at higher nozzle temperatures (above 13 K), only the slower primary pulse contains substantial dopant molecules.

4.2 Experimental Details

A schematic of our experimental arrangement is shown in Fig. 4.1. The apparatus combined a superfluid helium droplet source with two homemade Wiley-McLaren type time-of-flight mass spectrometers[20]: one in-line with the droplet beam (EI-TOF) and the other (MPI-TOF) perpendicular to the beam. The droplet source consisted of a pulsed valve (Digital Technology Trading & Marketing Ltd., E-L-5-8-C-Unmounted Cryogenic Copper Even-Lavie Valve) cryogenically cooled with a closed-cycle helium cryostat (Sumitomo, SRDK-408SW), and the lowest achievable temperature was ~8 K. The driving electric pulse for the valve had a duration of 24.8 μs, controlled by a driver from the same manufacturer (2009 Model Electronic Driver Unit). Superfluid helium droplets were formed by supersonic expansion of helium (Airgas, 99.9995%) through a conical nozzle of 50 μm in diameter with a stagnation pressure of 50 atm. The droplet beam passed through a 2 mm skimmer before entering the pickup chamber. In the pickup chamber, a flexible gas line (6 mm in outside diameter) was routed to the top of a pickup cell of 4 cm in diameter, and two circular apertures of 5 mm in diameter on the wall of the pickup cell were in line with the droplet beam. The vapor of room temperature CCl_4 was controlled by a leak valve, and it was sufficient to just open the leak valve to produce a stable doping pressure. The pickup chamber was separated from the main chamber through a home-

made conical cone with a 5 mm opening. The base pressure in the main chamber was below 10^{-6} Torr.

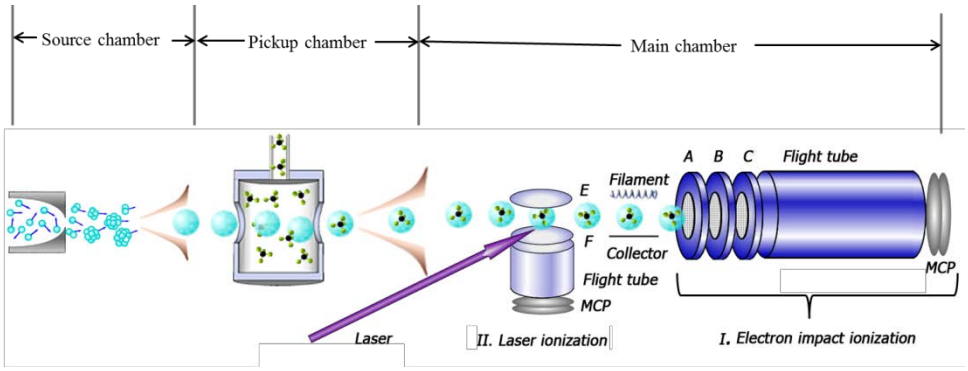

Fig. 4.1. Schematic diagram of the overall experimental setup including the electron impact ionization and laser ionization time-of-flight mass spectrometers.

For electron impact ionization, the electron source was a commercial fast ion gauge (Beam Dynamics, Inc, Model FIG-1) rewired for our purpose, although we have also had equal success with a home-made filament and grid. The tungsten filament supplied electrons by running at a constant current of 2.4 A, and the collector grid facing the filament was biased at 51 V to contain the thermal electrons. The droplet beam passed through the space between the filament and the grid. About 12 mm downstream from the electron source were three electrodes A – C separated by 19 mm, and the flight tube was about 43.2 cm long. Electrodes A and C were pulsed from -70 V to 300 V for 4 μs using a DEI PVX-4140 pulse generator, while electrode B was grounded. The negative voltage on electrode A was to prevent electrons from entering the interior of the mass spectrometer. Once the electrons were energized by the positive pulse, ionization was confined to the vicinity of electrode A, and ionized cations were pushed to electrode B. The duration of 4 μs of the ionization pulse was

necessary for accumulation of ions around electrode B. As soon as the voltage on electrode C was dropped back to -70 V, all cations accumulated between B and C were attracted to the flight tube, which was biased at a constant voltage of -180 V. Hence the time-of-flight of the detected ions started at the falling edge of the positive pulse. Ion signals were detected on a chevron-type microchannel plate detector (MCP).

For laser ionization, we used the fourth harmonic of a Nd:YAG laser (Quantel, Brilliant) at 266 nm and focused the laser beam using a 10" cylindrical lens between electrodes E and F. The pulse energy was ~10 mJ and the resulting power density was about 10^{12} W/cm^2. A single power supply was used to bias electrode E at 50 V and electrode F at 24 V. The gap between electrodes E and F was 9 mm to accommodate the whole droplet beam, and the gap between electrode F and the flight tube was only 3 mm. The flight tube was 6 cm long and was grounded. The electrodes and flight tube were attached to a rotatable wheel connected to a Cajon vacuum feedthrough, and they could be moved out of the way of the droplet beam by rotating the rod connected to the wheel. The MCP detector was mounted on a slide movable on a rail system, and it could be retracted to a corner of the chamber using another Cajon feedthrough . The whole assembly fits inside the bottom half of a cube-shaped chamber, measuring 25 cm in side length.

The apparatus was controlled by an interface card (DAQ NI-PCIe-6320), which sent out a 10 Hz trigger signal to electrodes A and C for the EI-TOF or to the Fire and Q-switch control of the laser for the MPI-TOF. A synchronized 5 Hz trigger was sent to the pulsed valve (PV) and to an input channel of the interface card. A

LabView program read the mass spectrum from an oscilloscope (Agilent, DSOX 2004A) and accumulated the droplet signal (PV on) and background signal (PV off) separately based on the input channel of the interface card.

Each mass spectrometer serves a different purpose. The EI-TOF was simple to construct and could ionize pure and doped droplets for preliminary diagnosis. However, the mass resolution of this simple setup was limited, and for detailed diagnosis of doped droplets, it was insufficient. The MPI-TOF relies on non-resonant multiphoton ionization, and under the current operating conditions, the laser power density was insufficient to ionize any helium atoms (more than five photons are needed), as was confirmed by the lack of any ionization signal with pure droplets. However, with the exception of helium, almost all molecular substances can be ionized with less than three photons at 266 nm. The precise position and timing of a pulsed laser and the easy fulfillment of the spatial focusing condition of the Wiley-McLaren TOF ensure a reasonable mass resolution within the limited space.

4.3 Results

4.3.1 Electron impact ionization

In the current configuration of the EI-TOF, the group velocity of the droplet beam was in-line with the flight axis of the EI-TOF, hence when all electrodes and the flight tube were grounded and the grid was biased at 160 V, we could observe droplet related ions directly arriving at the MCP detector. In fact, at a nozzle temperature of 16 K, we observed two peaks separated by 310 μs on the MCP under this condition, and only when we set the timing of the ionization pulse between the

two peaks could we record any mass spectrum containing substantial contributions from He^+_n with n > 1. Occasionally after changing the kapton gasket or cleaning the nozzle of the pulsed valve, we could observe a single peak when the opening time of the pulsed valve was shortened to less than 23 μs, but the observed beam intensity was typically lower than that when the pulse duration was longer than 24 μs and with the presence of twin peaks. We also noticed the existence of twin peaks when we reconnected the control of the ionizer to the fast ionization gauge. These two peaks could signify velocity slipping between smaller and larger droplets in a bi-modal size distribution[9,21], or they could represent the primary and a rebound pulse of the pulsed valve.

Fig. 4.2a shows the time-of-flight spectrum of the EI-TOF with (PV on) and without (PV off) pure helium droplets. The temperature of the droplet source was 16 K and the stagnation pressure was 50 atm. Without the droplet beam (PV off), energized electrons can ionize the ambient gas in the main chamber, producing a mass spectrum containing mostly H^+ at 2.105 μs and OH^+ at 8.655 μs from the residual H_2O in the high vacuum chamber. A long tail after the OH^+ is unresolvable, corresponding to masses in the range of 24 – 100 amu. Although some of these ions can be related to other residue gases such as N_2^+/CO^+, others are possible contaminants from previous experiments in the chamber or on the filament of the fast ionization gauge. When the pulsed valve is on (PV on), both ambient gas and helium droplets can be ionized, and quantitative changes occur in the mass spectrum. The difference between the two traces of PV on and off, as shown in the lower panel of Fig. 4.2, reveals the fragments related to the droplet, including atomic helium ions

and two distinguishable helium cluster ions He_2^+ and He_4^+. These clusters can be considered characteristic signatures of helium droplets.

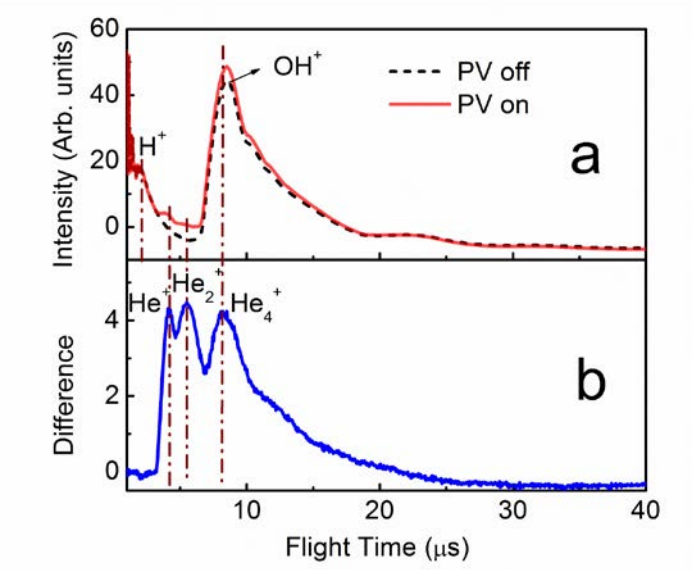

Fig. 4.2. Electron impact ionization time-of-flight mass spectra of background and pure helium droplets. The top panel shows the mass spectrum of the background (PV off) and that of the droplet beam (PV on) together with the background. The difference in the bottom panel is the net effect of the droplet beam.

The mass distribution in Fig. 4.2 was stable in terms of relative intensities of the different ion fragments when the source temperature of the pulsed valve varied from 8 K to 22 K, although the timing of the ionization pulse had to be adjusted due to the different speeds and hence arrival times of the droplet beam. Above 22 K, the magnitude of the cluster ions dropped precipitously, while the mass peak corresponding to He^+ remained more or less constant for all nozzle temperatures, up to room temperature.

Fig. 4.3 shows the time profile for the different helium related ions at a source temperature of 16 K. The atomic cation signal contains two peaks, with the first peak more intense and longer lasting. This peak was stable under almost all source temperatures, and it was substantially longer than that of the electrical driving pulse of the valve. The second narrow peak only existed when the nozzle temperature was between 8 and 22 K, and its full-width-at-half-maximum (FWHM) was only ~20 μs. This latter peak also coincided with the main peaks for the clusters $He_2^+$and He_4^+. We therefore conclude that only the latter peak contains substantial droplets, while the broader earlier peak contains mainly gaseous helium and a small amount of small droplets.

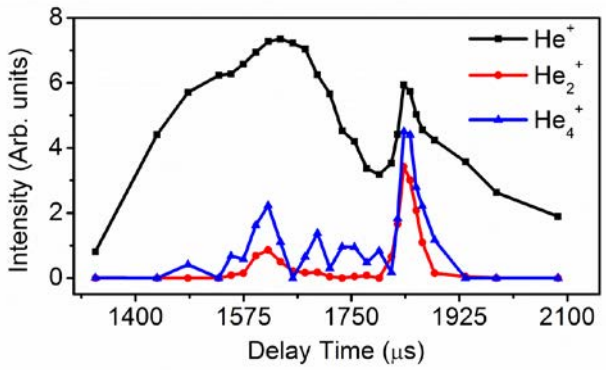

Fig. 4.3. Time profiles of the different cations He^+, He_2^+ and He_4^+ from the EI-TOF at a source temperature of 16 K. The delay time refers to the time between the electrical trigger signal to the pulsed valve and the time of the electric pulse for ionization.

The conclusion of Fig. 4.3 shows the importance of mass resolution in characterizing a helium droplet beam. Without the observation of helium clusters, it would be difficult to discern the presence of droplets since ionization from gaseous

helium still dominates the total ion signal. Furthermore, the time of arrival of the droplet beam is later than that of gaseous helium, and depending on the flight length between the nozzle and the ionization region, there can be a substantial separation between the gaseous signal and the droplet signal, by up to 600 μs in our case. The duration of the droplet beam is much shorter than that of the gaseous beam, which adds another layer of difficulty for pulsed experiments.

Fig. 4.4 shows the TOF spectrum when room temperature CCl_4 vapor was introduced into the doping chamber. The pulsed valve was at 16 K with a stagnation pressure of 50 atm. The base pressure of the doping chamber was 10^{-6} Torr, and during doping, the pressure rose to 10^{-5} Torr. Introduction of CCl_4 into the pickup chamber resulted in minimal change in the vacuum level of the main chamber, as confirmed from the comparison of the background spectra with and without doping. The negligible effect of the doping gas in the main chamber was mostly because of the 5 mm cone separating the main chamber from the doping chamber. Moreover, any signal from CCl_4 due to diffusion can be effectively removed when the difference between PV on and PV off was taken, as shown in the lower panel of Fig. 4.4. Upon doping, both He^+ and He_2^+ are reduced by 25% in the mass spectrum, and the presence of He_4^+ is no longer definitive. Instead, a new fragment of CCl_3^+ due to CCl_4 is observable. The exact time of arrival of the CCl_3^+ fragment, based on the calibration constants of the TOF, is labeled in the figure by the dot-dashed line, hence there is no ambiguity about its identity. Its broad width, however, hinders further resolution of other clusters including complexes of CCl_3^+ with helium atoms.

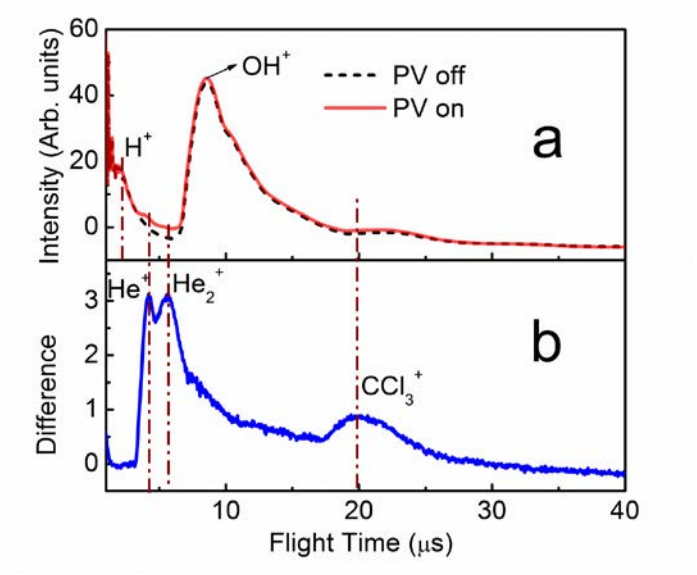

Fig. 4.4. Electron impact ionization time-of-flight mass spectra of background and doped droplets. The top panel shows the mass spectrum of the background (PV off) and that of CCl_4 doped droplets together with the background. The bottom panel shows the difference – the net effect of the doped droplets.

4.3.2 Laser ionization

As explained in the section on "Experimental Details", the intensity of our laser beam was insufficient to ionize helium atoms, hence the MPI-TOF can only be used to probe doped droplets. The top panel of Fig. 4.5 shows the MPI-TOF spectra without (PV off) and with (PV on) CCl_4 doped helium droplets, and the lower panel is the net difference between the two spectra. Conditions of the experiment, including the source temperature and stagnation pressure, remained the same as those of Figs. 4.2 - 4. Although the flight tube in this MPI-TOF is less than 1/5 the length of that of the EI-TOF, the mass resolution is much higher due to the well-defined small ionization region, the short ionization time (5 ns from the Q-switched Nd:YAG laser), and the spatial focusing conditions of the mass spectrometer. Similar to the EI-TOF

spectrum, the background from MPI-TOF also shows a prominent H^+ ion at 1.008 μs due to the presence of perhaps water or H_2 residues in the main chamber. Fragments at flight times of 3.508 μs can be assigned as C^+ and at 5.208 μs as CO^+ or $N_2{}^+$. However, a prominent peak at 5 μs is difficult to comprehend, corresponding to a mass of ~25 amu. We suspect that perhaps it is due to contaminants in the chamber from previous experiments, similar to those observed in the long tail of the EI-TOF spectrum in Fig. 4.2. Upon doping with CCl_4, the mass spectrum remains almost identical, and the difference is only observable after signal subtraction. Part of the reason for the small change is the not-so-ideal level of vacuum in the pickup chamber at 1×10^{-6} torr. Under this condition, without the "toggle" mode of data collection, it would be impossible to discern the doped signal from the background.

The difference spectrum shows that the most prominent peak is the fragment C^+, followed by Cl^+ and CCl^+. Although $CCl_3{}^+$ has the lowest threshold of formation from photoionization of CCl_4, it is not observable in our spectrum, most likely because of the abundant photons in the ionization region for subsequent dissociation. More importantly, we observe complexes of C^+ with helium atoms He_nC^+ with n = 1 – 5 and He_nCCl^+ with n = 2 - 9 in Fig. 4.5b. In an effort to find the missing complexes of He_nCl^+, we have extended the flight tube to 20 cm by adding an extension tube below the main chamber. Fig. 4.6 shows the improved mass spectrum, with resolution of the isotopes of chlorine. Complexes of He_nCl^+ can now be identified, albeit small in abundance. The formation of these complexes is only possible from ionization of doped droplets, since the density of CCl_4 in the ionization region should be far below that required for combination with a helium atom.

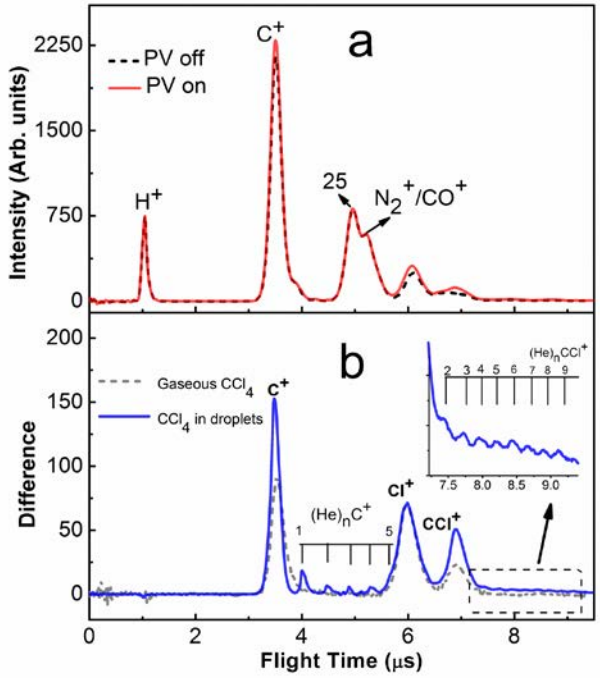

Fig. 4.5. Multiphoton ionization TOF of helium droplets doped with CCl_4. The top panel shows the mass spectrum of the background (PV off) and that of CCl_4 doped droplets together with the background. The solid line in the bottom panel shows the difference – the net effect of the doped droplets. The dashed grey line shows the mass spectrum of bare CCl_4 recorded by purposely diffusing the gaseous sample into the main chamber, and the signal intensity is normalized for the mass peak of Cl^+.

The dashed grey line in Fig. 4.5 shows the mass spectrum of bare CCl_4 purposely diffused into the main chamber recorded under the same laser conditions. The spectrum has been scaled for the intensity of the mass peak of Cl^+. The mass spectrum of gaseous CCl_4 contains relatively less C^+ and CCl^+, and in either case, the relative abundance of C^+/Cl^+ is far from 1:4. The relative abundance of Cl^+/CCl^+, however, is close to 3:1 for bare gaseous CCl_4.

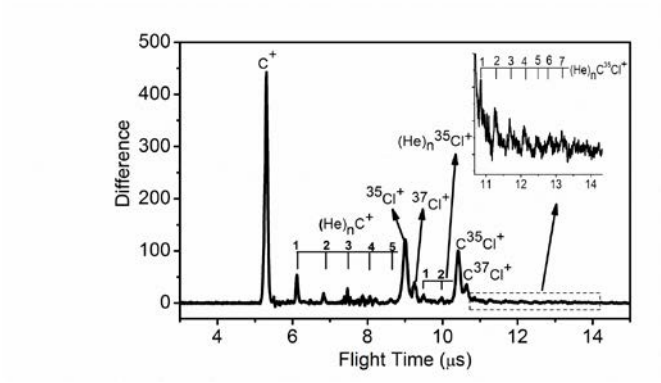

Fig. 4.6. Multiphoton ionization TOF of helium droplets doped with CCl_4 obtained using a longer flight tube (20 cm instead of 6 cm).

We have measured the power dependence of the different fragments as shown in Fig. 4.7. The relative intensity distribution of the different masses does not show any obvious dependence on the laser power, but the overall signal strength shows a general decrease with decreasing laser power. The experimental data have been fitted with polynomials. With F-test check, C^+ and Cl^+ can be best fitted using second order functions and CHe^+ and CCl^+ can be fitted with third order functions, all with the restriction of forcing the fitting functions through the origin. Energetically, 6 photons are required to strip all chlorine atoms from CCl_4 to form C^+ at 266 nm. The fitting results therefore imply extensive saturation in a few of the intermediate steps. On the other hand, the relative branching ratio of Cl^+ and CCl^+ increases with laser flux, in general agreement with the fact that when more photons are available, CCl^+ can further fragment into Cl^+.

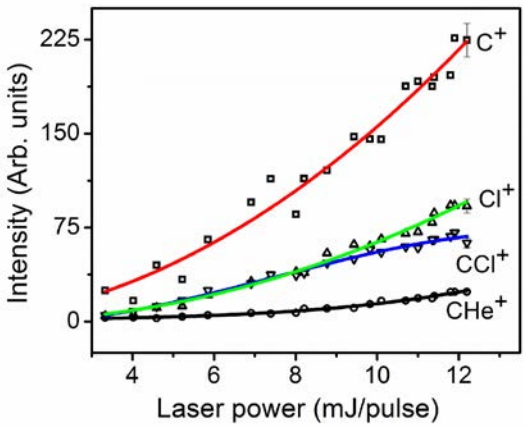

Fig. 4.7. Power dependent studies of the different fragments from MPI of CCl_4 doped droplets. The solid lines going through the experimental points are fittings using polynomials (C^+ and Cl^+ are second order; CCl^+ and CHe^+ are third order).

Photoionization of doped helium droplets has been investigated using synchrotron radiations, femtosecond lasers, and nanosecond lasers[18,19,22]. Different approaches seem to follow different ionization mechanisms, with different fragmentation patterns for the same doped species. Our condition with a nanosecond laser at 266 nm in the power density range of 10^{12} W/cm^2 proves to be yet another unique case, with abundant formation of C^+ and without any fragment larger than CCl^+.

4.3.3 Time profile of the Even-Lavie pulsed valve

We have also measured the time profile of the dopant from our droplet beam, using the four most abundant fragments from Fig. 4.5b. Fig. 4.8 shows the variation of ion yields as a function of the delay time between the electrical pulse to the pulsed valve and the laser pulse for ionization. The same measurement has also been carried out using the EI-TOF at the same source temperature of 16 K, and very similar time

profiles have been obtained, although a time delay of ~300 μs has been observed due to the drift time between the locations of MPI and EI. For all four fragments, Fig. 4.8 shows a consistent double pulse and a duration of 20 μs for the more intense pulse. This result confirms that the duration of doped droplets is only 20 μs, and that the latter pulse, nearly 200 μs after the earlier pulse, contains more dopant under the current condition.

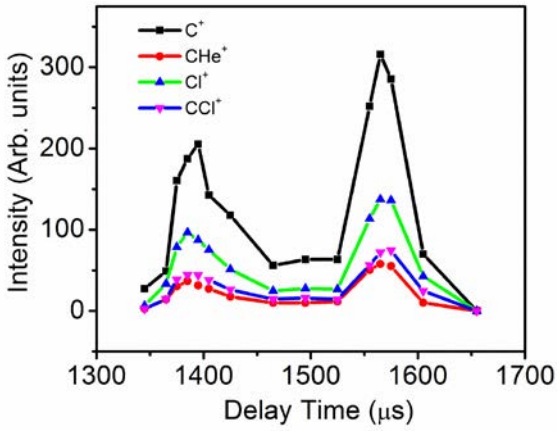

Fig. 4.8. Time profiles of the different cations C^+, CHe^+, Cl^+ and CCl^+ from the MPI-TOF recorded at a source temperature of 16 K. The delay time refers to the time between the electrical trigger signal to the pulsed valve and the time of the laser pulse for ionization. The latter peak produces more dopant fragments than the earlier one.

We have repeated the same type of measurements at different source temperatures between 8 K and 18 K, and the results are qualitatively the same, always with two droplet pulses. The relative intensities of the two pulses and their separation in timing, however, depended on the source temperature. Below 13 K, the earlier droplet pulse contained more doped ions than the latter droplet pulse, while above 13 K, it was always the latter pulse that contained more droplets. Fig. 4.9 shows a

sample profile at 12 K using CBr_4 as dopant. In this case, the earlier pulse contains more dopant than the latter pulse. The time separation of the two droplet pulses progressively gets smaller with increasing source temperature, from 600 μs at 8 K to 100 μs at 18 K.

The twin pulse in the time profile can be analyzed from the available data of the two spectrometers at two different locations along the beam path. As shown in Fig. 4.1, the MPI-TOF is located in the middle of the main chamber 54 cm from pulse valve, and the EI-TOF is located further downstream, at the exit of the chamber separated by 13 cm from the MPI-TOF. Knowing the timing of the laser pulse and the EI pulse, we can calculate the velocity of the two different droplet pulses: the earlier pulse has a velocity of 452 m/s, and the latter pulse of 374 m/s. If we assume that the speeds are the same along the whole travelling distance, we can calculate the exit times of the droplet pulses from the pulsed valve. Knowing the time of the electrical pulse to the pulsed valve, we can then obtain the release time of each droplet pulse. Our numbers indicate that at a source temperature of 16 K, the earlier pulse is released 146 μs after the electrical pulse, and the latter pulse is released 71 μs after the electrical pulse. Thus the latter pulse is released ~70 μs prior to the earlier pulse at the pulsed valve! Somewhere downstream from the pulsed valve, the two pulses have to overlap and switch in order. To confirm this assessment, we can check the free drift time in the EI-TOF when all electrodes and the flight tube are grounded – an advantage of having the EI-TOF coaxial with the droplet beam. The flight path in the EI-TOF is 46 cm, hence the droplets drift a total distance of 113 cm to the MCP detector with total flight times of 2635 μs and 2965 μs. Taking the release times of

the pulses into consideration, we can then get the velocities of the two groups of ions: 451 m/s and 389 m/s. These numbers agree with the calculated speeds from MPI-TOF/EI-TOF.

The above situation alludes to an interesting working hypothesis. When the pulsed valve is first opened, larger droplets with a slower speed are initially formed (referred to as the initial or primary pulse in the following), and then the valve has a rebound, and smaller droplets with a faster speed are released (the rebound pulse). The faster rebound group catches up with the slower group, most likely before the skimmer of the source chamber. At a source temperature of 16 K, the location for the overlapping pulses is ~15 cm downstream from the nozzle, just before the skimmer. In the doping chamber, when the source temperature of the pulsed valve is higher than 13 K, the rebound pulse passes through the doping region picking up only a small amount of dopant due to the small sizes of the droplets. The latter primary pulse, on the other hand, has a higher doping efficiency, resulting in abundant dopant in the latter pulse as shown in Fig. 4.8. Further downstream, in both the MPI and EI experiments, the faster earlier group is actually the rebound pulse, while the slower pulse is the initial pulse with a higher droplet content and larger droplets. At lower source temperatures, on the other hand, even the rebound pulse contains sufficiently large droplets for effective doping. Thus the rebound pulse can result in depletion of dopant molecules in the pickup chamber, thereby decreasing the amount of dopant in the latter primary pulse as shown in Fig. 4.9.

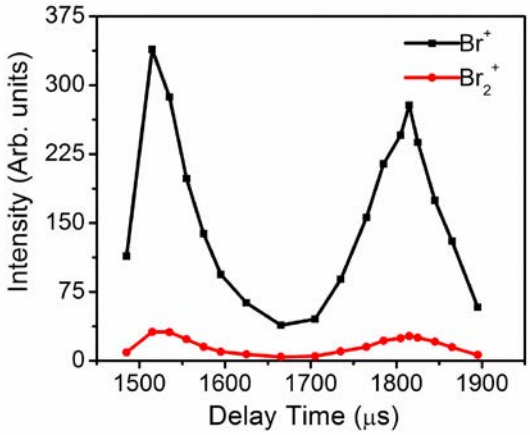

Fig. 4.9. Time profiles of Br^+ and Br_2^+ from MPI-TOF of CBr_4 doped droplets recorded at a source temperature of 12 K. The delay time refers to the timing between the electrical trigger signal to the pulsed valve and the time of the laser pulse for ionization. Opposite to the case of Fig 4.8, the earlier peak generates more dopant fragments than the latter one.

In a previous report by Pentlehner et al[9], the Even-Lavie pulsed valve has been fully characterized based on Rayleigh scattering and laser induced fluorescence (LIF). Under most stagnation pressures and source temperatures between 10 and 15 K, double peaks in both Rayleigh scattering and LIF experiments could be observed. Based on the persistence of signal in the latter pulse in the absence of doping or under non-resonant excitation, the authors attributed the latter pulse to Rayleigh scattering of large droplets, and thus established the bimodal size distribution of the droplet source. However, when the source temperature was raised to 20 K and the repetition rate was lowered to 10 Hz, a condition highly unfavorable for Rayleigh scattering, the time profile of the fluorescence still showed a broad shoulder separated by ~40 μs from the main pulse (Fig. 10 of ref [9]). In general, the double peaks seemed to

disappear at high stagnation pressures (above 50 atm) and high repetition rates (≥ 100 Hz).

At this point, we cannot completely eliminate the possibility of velocity slip and a bimodal size distribution in our droplet beam, and we are unclear if the shoulder peak in the report of Pentlehner et al[9] is the same as the twin peak that we observe in this work. However, there are several pieces of evidence that favor our conclusion. First we observe dopant fragments in both droplet pulses, and the relative intensities of the fragments switch with changing source temperature. We therefore can deduce that there should be a temperature, perhaps around 13 K, that corresponds to equal sized droplets in the two pulses. This is in direct contradiction of bimodal size distribution. Second, the speeds obtained from the free drifting condition, 451 and 389 ± 30 m/s for the two droplet pulses, and from the timing of ionization between EI and MPI, 452 and 374 m/s, are consistent with the idea of two pulses instead of bifurcation of one pulse. We have also found that by shortening the duration of the electrical control to the pulsed valve, the double pulse can sometimes be combined into one, but the intensity of the droplet beam suffers. This fact further disagrees with the possibility of velocity slip and bimodal size distribution.

A point of concern with cryogenic pulsed valves is the seal between the nozzle component and the valve body. The assembly of both the Even-Lavie valve and the general valve from Parker Hannifin Corp (series 99) requires finger tightening of the nozzle component, which results in inconsistent behavior of the resulting device, even for operation under room temperatures. As illustrated by Pentlehner et al[9], the time profile of the droplet beam also varies with stagnation pressure and

source temperature. It is therefore likely that the difference between the work of Pentlehner et al[9] and our own is due to the different tightness of the nozzle component. It is also possible to suppress the rebound by adjusting the electrical control, the stagnation pressure and the temperature of the nozzle, but some compromise would have to be made in the droplet size or flux. Improvements in the consistency of the valve assembly are certainly important in eliminating discrepancies regarding pulsed droplet sources.

4.4 Discussion

Our EI-TOF is simple to construct and is good enough for rudimentary diagnosis of helium droplet beams. A key component is a pulser that provides a negative offset and a positive pulse to energize thermal electrons for ionization. The frequency of the pulser should be on the order of a MHz, since the time scale of the TOF is on the order of microseconds. The electron source is a tungsten filament supplied with a large current, and the electron collector grid can be of any shape between a coil and a straight piece of wire. The acceleration field for the electrons is in-line with the flight tube, hence no transverse velocity is gained for the charged particles from the ionization process. Compared with a fast ionization gauge, a commonly used diagnostic tool for molecular beams, the overall cost of our EI-TOF might be higher because of the pulser and the MCP detector, but the additional mass information is valuable, particularly because of the short duration and the complicated time profile of the droplet beam.

In comparison, typical TOF mass spectrometers use collimated electron beams for electron impact ionization. Although a commercial electron gun or beam[23,24] has

its advantages in spatial and timing control, it is expensive and largely overkill for diagnostic purposes. Moreover, the acceleration field of the electron beam also introduces a velocity perpendicular to the flight axis for the cations, and to compensate, a set of deflectors is needed downstream from the ionization region. Using an electron beam source coupled with a time-of-flight mass spectrometer (TOF), Ellis's group has demonstrated velocity slip in a droplet beam and reported the effect of the nozzle shape on droplet sizes[21,23]. The authors have even suggested size selection based on the time delay between the electrical driving pulse and the firing time of the ionization or excitation beam. Although the mass resolution of our EI-TOF is far inferior to that of commercial mass spectrometers, it is sufficient for identifying signatures of superfluid helium droplets and dopants and for mapping out the time profile of a droplet beam with a time resolution of a microsecond.

The major item in our MPI-TOF is a pulsed Nd:YAG laser. The additional mass resolution afforded by the compact MPI-TOF is appealing for diagnosis of doping conditions. With a moderate laser and by focusing the UV light into the ionization region, almost all molecular species can be ionized, with the exception of helium atoms. Lack of pure helium ions makes the method only sensitive to doped droplets, a unique feature of this setup. The spectrometer can be made miniature in size, and can be removed from the interaction region after diagnosis without venting the chamber. These features make it appealing for a quick check prior to any planned experiments.

The key to the success of these two spectrometers is the "toggle" function offered by the interface card. The mass spectrum taken by the oscilloscope is sorted

and accumulated in the computer after each ionization event, and instantaneous subtraction effectively removes the background obtained without the droplet beam. Limited by the data transfer protocol of the oscilloscope, however, our highest effective repetition rate is 8 Hz.

4.5 Conclusion

We have presented two facile methods of detecting superfluid helium droplets and droplets with neutral dopants, both using time-of-flight technology for mass resolution. Without an electron beam and with pulsed electrodes, we have demonstrated electron impact ionization of pure and CCl_4 doped helium droplets with a moderate mass resolution. The information was sufficient to diagnose the droplet beam, with clear indications of helium cluster ions and fragments of dopants. By focusing the 4^{th} harmonic of a pulsed Nd:YAG laser, we have ionized CCl_4 doped in helium droplets and resolved helium complexes with C^+ and other fragments from non-resonant multiphoton ionization. These two spectrometers have been used to measure the time profile of the droplet beam, revealing the existence of an initial primary pulse and a rebound pulse, each with a duration as short as 20 μs. The rebound pulse could overtake the initial pulse prior to doping. When the source temperature was below 13 K, there were sufficient droplets in the rebound pulse to deplete the dopant prior to the arrival of the initial pulse, so the earlier pulse in the MPI and EI region contained more dopant. At higher source temperatures, on the other hand, the rebound pulse did not have enough large sized droplets for dopant depletion, and the initial pulse that arrived later than the rebound pulse contained more dopant. Without the mass resolution and the timing information afforded by the

mass spectrometers, it would be difficult to capture the detailed behavior of the droplet beam and to precisely determine the timing of dopant containing droplets.

Acknowledgement

This work is supported by the National Institute of General Medical Sciences (1RC1GM092054 -01 and 1R01GM101392-01A1) from the National Institutes of Health. The content is solely the responsibility of the authors and does not necessarily represent the official views of the National Institutes of Health. Additional support from the Oregon Nanoscience and Microtechnologies Institute, and the Environmental Health Science Center at Oregon State University funded by the National Institute of Environmental Health Sciences (ES000210) are also deeply appreciated. We also thank Collin Harthcock in helping with the laser ionization setup. Special thanks to Dr. Slenczka for his consultation with the performance of the Even-Lavie pulsed valve.

4.6 References

1 J. P. Toennies and A. F. Vilesov, Annu. Rev. Phys. Chem. **49**, 1 (1998).
2 J. P. Toennies and A. F. Vilesov, Angew. Chem., Int. Ed. **43**, 2622 (2004).
3 S. Yang and A. M. Ellis, Chem. Soc. Rev. **42**, 472 (2013).
4 A. Bartelt, J. D. Close, F. Federmann, N. Quaas, and J. P. Toennies, Phys. Rev. Lett. **77**, 3525 (1996).
5 J. Tiggesbaeumker and F. Stienkemeier, Phys. Chem. Chem. Phys. **9**, 4748 (2007).
6 W. Kong, L. Pei, and J. Zhang, Int. Rev. Phys. Chem. **28**, 33 (2009).
7 F. Bierau, P. Kupser, G. Meijer, and G. von Helden, Phys. Rev. Lett. **105**, 133402 (2010).
8 M. Goulart, P. Bartl, A. Mauracher, F. Zappa, A. M. Ellis, and P. Scheier, Phys. Chem. Chem. Phys. **15**, 3577 (2013).
9 D. Pentlehner, R. Riechers, B. Dick, A. Slenczka, U. Even, N. Lavie, R. Brown, and K. Luria, Rev. Sci. Instrum. **80**, 043302 (2009).
10 H. Buchenau, J. P. Toennies, and J. A. Northby, J. Chem. Phys. **95**, 8134 (1991).

[11] B. E. Callicoatt, K. Forde, T. Ruchti, L. Jung, K. C. Janda, and N. Halberstadt, J. Chem. Phys. **108**, 9371 (1998).
[12] T. Ruchti, K. Forde, B. E. Callicoatt, H. Ludwigs, and K. C. Janda, J. Chem. Phys. **109**, 10679 (1998).
[13] M. N. Slipchenko, S. Kuma, T. Momose, and A. F. Vilesov, Rev. Sci. Instrum. **73**, 3600 (2002).
[14] S. Yang, S. M. Brereton, M. D. Wheeler, and A. M. Ellis, J. Phys. Chem. A **110**, 1791 (2006).
[15] H. Schöbel, P. Bartl, C. Leidlmair, S. Denifl, O. Echt, T. D. Märk, and P. Scheier, Eur. Phys. J. D **63**, 209 (2011).
[16] R. Froechtenicht, U. Henne, J. P. Toennies, A. Ding, M. F. Fieber-Erdmann, and T. Drewello, J. Chem. Phys. **104**, 2548 (1996).
[17] D. S. Peterka, J. H. Kim, C. C. Wang, L. Poisson, and D. M. Neumark, J. Phys. Chem. A **111**, 7449 (2007).
[18] A. Braun and M. Drabbels, J. Chem. Phys. **127**, 114303 (2007).
[19] M. Mudrich and F. Stienkemeier, Int. Rev. Phys. Chem. **33**, 301 (2014).
[20] W. C. Wiley and I. H. McLaren, Rev. Sci. Instrum. **26**, 1150 (1955).
[21] S. Yang and A. M. Ellis, Rev. Sci. Instrum. **79**, 016106 (2008).
[22] D. S. Peterka, J. H. Kim, C. C. Wang, and D. M. Neumark, J. Phys. Chem. B **110**, 19945 (2006).
[23] S. Yang, S. M. Brereton, and A. M. Ellis, Rev. Sci. Instrum. **76**, 104102 (2005).
[24] H. Schöbel, M. Dampc, d. S. F. Ferreira, A. Mauracher, F. Zappa, S. Denifl, T. D. Märk, and P. Scheier, Int. J. Mass Spectrom. **280**, 26 (2009).

Chapter 5 Electron impact ionization and multiphoton ionization of doped superfluid helium droplets: a comparison

Yunteng He, Jie Zhang, and Wei Kong

Department of Chemistry, Oregon State University, Corvallis, OR 97331

Journal of Chemical Physics

1305 Walt Whitman Road Suite 300

Melville, NY 11747-4300

144, 084302 (2016)

*Corresponding author, 541-737-6714, wei.kong@oregonstate.edu

Abstract

We compare characteristics of electron impact ionization (EI) and multiphoton ionization (MPI) of doped superfluid helium droplets using the same droplet source. Selected dopant ion fragments from the two ionization schemes demonstrate different dependence on the doping pressure, which could be attributed to the different ionization mechanisms. While EI directly ionizes helium atoms in a droplet therefore has higher yields for bigger droplets, within a limited size range, MPI is insensitive to the helium in a droplet and is only dependent on the number of dopant molecules. The optimal timing of the ionization pulse also varied with the doping pressure, implying a velocity slip among different sized droplets. Calculations of the doping statistics and ionization probabilities qualitatively agree with the experimental data. Our results offer a word of caution in interpreting the pressure and timing dependence of superfluid helium droplets, and we also devise a scheme in achieving a high degree of doping while limiting the contribution of dopant clusters.

5.1 Introduction

Superfluid helium droplets have proven a versatile medium to isolate and cool both neutral and ionic species for spectroscopic and other fundamental studies, and for generation of esoteric species.[1-4] Recently, our group has introduced electron diffraction of doped superfluid helium droplets for single molecule diffraction,[5] with the ultimate goal of structure determination from Fraunhofer diffraction of oriented molecules.[6] Among the many research activities involving superfluid helium droplets, ionization of pure and doped helium droplets has been intensively studied.[7-10] In fact, mass spectrometers have played and continue to play a crucial role in the development of techniques involving superfluid helium droplets. As the most inert element, helium has the highest ionization potential, hence electron impact ionization (EI) has been the initial choice.[10,11] Upon collision with sufficiently high energy electrons, He_n^+ ($n \geq 1$) has been observed, and the presence of these cluster ions has been regarded as evidence of helium droplets. If neutral dopant molecules are present in the droplet, bare fragment ions of dopant and cluster ions of dopant fragments with helium atoms and helium clusters have also been observed.[12,13] A prevailing theory on the mechanism of electron impact ionization is the charge hopping model,[14,15] where the first target of ionization is a helium atom on a droplet. Then He^+ undergoes resonant hopping inside the droplet until the charge localizes or until it encounters a dopant molecule. The ionization yield of electron impact ionization therefore decreases with decreasing droplet size.

Photoionization of doped helium droplets has been investigated using synchrotron sources, femtosecond lasers, and nanosecond pulsed lasers.[7] In the extreme ultraviolet region where the photon energy is above the ionization threshold of helium, direct ionization of both helium and dopant molecules is possible.[16,17] However, given the presence of thousands to millions of helium atoms compared with one neutral molecule, direct ionization of helium probably dominates the first ionization event. For light sources with lower photon energies, multiphoton ionization (MPI) is typically required.[18-20] Since ionization of a ground state helium atom requires more photons than that of a neutral dopant molecule, in MPI, dopant molecules are the frontline species of direct ionization. Hence depending on the experimental procedure, different modes of photoionization occur with different fragmentation patterns even for the same doped species.[7,21]

In all previous literature reports, typically only one type of ionization processes was employed in one laboratory.[7,9,13] Our group has employed both electron impact ionization and multiphoton ionization mass spectrometry in the same vacuum system,[20] which enables us to directly compare the yields and sensitivities of the two types of processes. We measure the ionization fragments under different droplet source conditions and different doping conditions, with two essentially exchangeable dopant molecules CCl_4 and CBr_4. Our results are surprising at first sight, and we attribute the difference between EI and MPI to the different ionization mechanisms. We also offer a word of advice in choosing a diagnostic tool for the performance of a neutral doped helium droplet beam, particularly for pulsed beams,

and we also devise a condition to maximize the fraction of doped droplets while still limiting the formation of dopant clusters.

5.2 Experimental Setup

A schematic of our experimental arrangement has been described in our previous publication.[20] The pulsed droplet beam was formed by supersonic expansion of helium (Airgas, 99.9995%) from an Even-Lavie pulsed valve with an electric driving pulse of 24.8 μs in duration. The droplet beam passed a 2 mm dia. skimmer to enter the pickup chamber and a 5 mm dia. home-made conical cone to enter the main chamber. The pressure of the doping chamber was measured by an ionization gauge located ~12 cm away from the droplet beam. Two home-made time-of-flight (TOF) mass spectrometers were used in the main chamber: one in-line with the droplet beam (EI-TOF) and the other (MPI-TOF) perpendicular to the beam. The overall system ran at 5 Hz, and in between droplet pulses, a background spectrum was taken as reference, so the repetition rate of the ionization pulse, either electrons or photons from a laser, was 10 Hz. The difference between the signals from the doped droplets and the background should therefore be representative of the net effect of the droplet beam, independent of any slow drifts in the experimental condition. This aspect was crucial particularly when doping with a gaseous sample such as CCl_4, and the doping gas could diffuse into the main chamber and contribute to the background.

For the EI-TOF, the ionization source was a heated tungsten filament, and the electrons were momentarily energized by a pulsed grid to 300 V for ionization. The ionization pulse of 4 μs was superimposed on a constant offset of -70 V on the

extraction electrode, and the falling edge of the ionization pulse was the starting time of the time-of-flight mass spectrum. The ionization potentials for CCl_4 and CBr_4 are 11.5 eV[22] and 10.3 eV[23] respectively, and intense fragmentation is expected in the mass spectrum. Limited by the not-well-defined ionization region of the electron source and the initial velocity of the droplets, the mass resolution of the EI-TOF was insufficient to resolve small fragments of dopant molecules from cluster ions of helium. However, when doping with CCl_4, the signal from CCl_3^+ was sufficiently shifted from the congested region where helium cluster ions He_n^+ are significant. Consequently, $CCl_3^+$was chosen as the signature of the doped droplet.

We used the 4th harmonic of a nanosecond Nd:YAG laser (Quantel, Brilliant) for non-resonant multiphoton ionization. With a power density of 10^{10} W/cm^2 at 266 nm, only dopant molecules could be ionized. The mass spectrometer was similarly designed as the EI-TOF,[20] except that the flight tube was less than 1/3 of the length of the EI-TOF, and it was perpendicular to the traveling direction of the droplet beam. Nevertheless, the well defined ionization region and time from the focused laser resulted in high resolution mass spectra, and fragments of dopant molecules and clusters of dopant fragments with helium atoms, including $(He)_nC^+$, $(He)_nCl^+$ and $(He)_nCCl^+$ (n = 0 – 9), were observable. Unfortunately, easy fragmentation in the presence of a photon flux at 10^{28} photons/s·cm^2 severely limited the yield of the larger CCl_3^+ ions. Attempts to lower the intensity of the laser beam by reducing the laser power and by shifting the focal point of the laser did not yield any substantial difference in the fragmentation pattern. Given the complexity of the ionization mechanism, no further effort was dedicated to further decipher the fragmentation

pattern. The largest detectable dopant fragment was CCl^+ and its complexes with helium, and the intensity of bare CCl^+ was about 1/3 less than that of Cl^+. Consequently, here we use the intensity of the light fragment Cl^+ as a signature of the doped droplet.

5.3 Results

5.3.1 Dependence of ionization yield on doping pressure

The traces labeled "fixed timing" in Fig. 5.1 show the dependence of signature fragments from EI and MPI on the doping pressure. The stagnation pressure and temperature of the pulsed valve were kept at 50 atm and 16 K. The presence of CCl_3^+ from the EI-TOF is only observable within a small pressure range, and the maximum signal corresponds to a doping pressure of 6×10^{-6} Torr. The timing of the ionization pulse was therefore set based on the signal at 6×10^{-6} Torr, and so was the normalization of the ion yields under different doping pressures. The profile of Cl^+ from MPI is normalized to be comparable with that from the EI-TOF, but the actual signal intensity from the MPI experiment was more than 3 orders of magnitude larger than that from the EI-TOF. The timing of the ionization laser was set based on the optimal signal at 1×10^{-5} Torr.

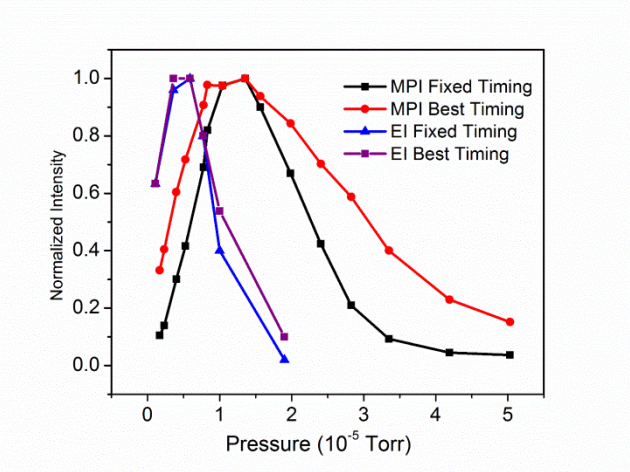

Fig. 5.1. Dependence of electron impact ionization and multiphoton ionization of CCl_4 doped helium droplets on the doping pressure recorded at a source temperature of 16 K and a stagnation pressure of 50 atm. The MPI trace labeled "fixed timing" was recorded at the optimal timing of the laser pulse obtained at a doping pressure of 1×10^{-5} Torr, while the EI trace labeled "fixed timing" was recorded at the timing determined at a doping pressure of 6×10^{-6} Torr. The profiles labeled "best timing" were obtained by adjusting the timing of the ionization pulse at each doping pressure.

The results in Fig. 5.1 are surprising at first sight – they reveal different optimal doping conditions for the two different experiments. Signal from the MPI-TOF reaches its peak after that from the EI-TOF has dropped to a negligible level. Although the spectrometers are not identical, and limited by the resolution and mass range, different fragments are used in Fig. 5.1, the different responses of the two spectrometers to the doping pressure of the same droplet beam are still unexpected.

A plausible explanation of Fig. 5.1 is the different ionization mechanisms of EI and MPI. The cross section of electron impact ionization for helium at 300 eV is

28 Mb based on the database from National Institute of Standards and Technology.[24] Although there is no data for the cross section of CCl_4, based on the values for CCl_nF where n = 1 to 3, an upper estimate of 1000 Mb can be assumed. Thus it takes less than 40 helium atoms to shadow a CCl_4 molecule during EI. For a droplet containing over a thousand helium atoms and one CCl_4 molecule, the first ionized species should be helium atoms surrounding the dopant. The ionization yield should thus be reflective of the size of the droplet: assuming a constant probability of charge transfer, larger droplets are highly favored in producing dopant ions in EI.

For MPI, on the other hand, only doped CCl_4 can be ionized given the limited photon flux. Superfluid helium is transparent in the ultraviolet, and based on the lack of any ion signal without dopant, we are confident that no substantial absorption is possible under our current laser intensity. Hence absorption of CCl_4 at 266 nm is not affected by the surrounding helium atoms. It takes three photons to ionize one CCl_4 molecule and to produce one CCl_3^+ ion, and 5 photons are needed to produce Cl^+.[25] Power dependent studies of the yield of Cl^+ have revealed a second order relation – a significant but not full saturation.[20] With increasing doping pressure, more droplets are doped and more than one dopant molecule can reside in one droplet, and both result in increased yields of dopant fragments at high doping pressures.

5.3.2 Timing dependence

During the MPI experiment, we noticed that the best timing for the dopant fragments also changed with the doping pressure. Fig. 5.2 shows the time profile of Br^+ from MPI of doped CBr_4 at two different nozzle temperatures. Similar results

were also obtained with CCl_4, but our data for CBr_4 are much more complete. The delay time in Fig. 5.2 is the time between the trigger signal to the pulsed valve and the onset of the laser pulse. In a previous publication,[20] we have established the existence of a primary and a rebound droplet pulse under our experimental conditions, and have detailed the different pickup probabilities of the two pulses at different source temperatures. When the nozzle temperature is below 13 K, the rebound pulse contains enough large droplets for effective doping, so the earlier pulse at 8.5 K contains abundant dopant.[20] Since the rebound pulse has an effect of depleting the dopant concentration in the doping chamber, the amount of dopant in the primary pulse is smaller. Above 13 K, the rebound pulse does not contain sufficiently large droplets for effective doping and dopant depletion, hence the primary pulse contains more dopant molecules.

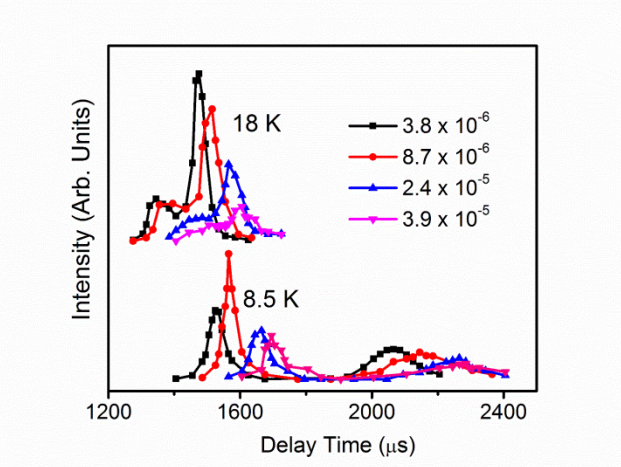

Fig. 5.2. Time profiles of Br^+ at different doping pressures of CBr_4 (in Torr) from the MPI-TOF recorded at source temperatures of 8.5 K and 18 K. The delay time refers to the time between the electrical trigger signal to the pulsed valve and the time of the

laser pulse for ionization. Only one of the peaks at each temperature contains a substantial amount of dopant molecules.

The shift in timing with doping pressures at both source temperatures, up to 200 μs, is noticeable. The mechanism is related to the different speeds of different sized clusters in a droplet beam, i. e., velocity slip.[26] The electrical pulse of the pulsed valve (24.8 μs) is much shorter than the flight time from the pulsed valve to the ionization region (> 1 ms), hence all droplets can be regarded as formed at the same the time from the pulsed valve. The much longer duration of the actual droplet pulse probed in Fig. 5.2, more than 200 μs in time spread among the sampled doping pressures, should therefore be predominantly due to the different velocities of the different sized droplets. Smaller droplets have higher speeds and are at the front of the pulsed beam, and they are easily destroyed with doping. Larger slower droplets survive the doping process but they reach the detection region at a later time. This change in timing with doping pressure is particularly important for pulsed droplet beams, since the doping pressure directly affects the timing of the excitation beam.

This realization prompted us to revisit Fig. 5.1, for both the MPI and EI experiments. At each doping pressure, we varied the timing of the ionization pulse to find the best ion signal, and the resulting pressure profiles are designated as the "best timing" profiles. The MPI profile labeled "fixed timing" was obtained by optimizing the timing at a doping pressure of 1×10^{-5} Torr, hence at this pressure, the two MPI experiments have the same signal strength. At lower doping pressures, the "best timing" profile extends further into the region with lower doping pressures, while at higher doping pressures, the "best timing" profile extends to much higher pressures.

At 3×10^{-5} Torr, the MPI signal shows a more than 3-fold increase under the "best timing" condition. In contrast, the EI signal shows limited improvement as the timing is varied at different doping pressures. In fact, the best timing for EI is within 50 μs of the original timing set at a doping pressure of 6×10^{-6} Torr. The effect of velocity slip in the EI experiment seems to be weaker than in the MPI experiment.

5.4 Analysis

A qualitative modeling of both the MPI and EI processes can be achieved based on Poisson pickup statistics.[27] We can calculate the probability of a droplet containing *n* helium atoms capturing *k* number of molecules $P_k(\rho;n)$ at a dopant gas density ρ. Unfortunately, the analytical expression from Poisson statistics[27] is based on negligible changes in the droplet size upon collisions. The most probable size of our droplet beam is ~2000 atoms/droplet,[28] and pickup of one CCl_4 reduces the size by nearly 1/3. For these small sized droplets, size reduction has to be taken into consideration. For qualitative modeling, we modified the expression for the pickup probability by:

$$P_k(\rho;n) = \frac{z_k^{\,k}}{k!}\exp(-z_k), \qquad (5.1)$$

where z_k is the effective cross section for picking up *k* molecules with $z_1 = \rho \cdot \sigma_{e0} \cdot L$, and *L* (30 cm) is the length of the doping cell. The effective capture cross section σ_{e0} of a undoped droplet is considered proportional to the physical size of the droplet $\sigma_0 = \pi r_0^2$ with $r_0 = 2.22\sqrt[3]{n}$ (Å). After picking up one dopant molecule, a droplet reduces its size by N_1 (500 – 700 helium atoms[29]) to $n_1 = n - N_1$, and the new

pickup cross section is reduced to $\sigma_1 = \pi r_1^2$ with $r_1 = 2.22\sqrt[3]{n_1}$ (*Å*), so the effective pickup cross section across the whole length of the doping cell is $\sigma_{e1} = (\sigma_0 + \sigma_1)/2$, and the corresponding $z_2 = \rho \cdot \sigma_{e1} \cdot L$. For a droplet containing only 2000 helium atoms, the maximum doping number is $k_{max} = 3$, with $\sigma_{e3} = (\sigma_0 + \sigma_1 + \sigma_2)/3$. In practice, however, a helium reserve is required to transport the doped droplet from the doping region to the detection region and to limit the gain in transverse velocity from side-on collisions with dopant molecules, hence the maximum doping number should be smaller than the thermal dynamic limit n/N_1.

5.4.1 Modeling the MPI pressure profiles

During the MPI experiment, the laser has a duration of 5 ns, hence ionization should only probe droplets of a fixed size, assuming sufficient velocity slip in the droplet beam. If the timing of the ionization laser is fixed, then the same sized droplets are detected throughout the whole range of pressures for the profile labeled "fixed timing" in Fig. 5.1. The signal in the MPI experiment should depend on the number of dopant molecules in the droplet beam. Here we ignore the dependence of the ionization mechanism on cluster size,[30] and assume that the yield of Cl^+ ions $I_{MPI}(\rho;n)$ is proportional to the number of doped molecules k:

$$I_{MPI}(\rho;n) \propto \sum_{k=1}^{k_{max}} k \cdot P_k(\rho;n) \ . \qquad (5.2)$$

To compare with the experiment under "fixed timing", we varied n from 1000 to 10,000, k_{max} from 1 to n/N_1, and N_1 from 500 – 700,[29] and the calculated maximum intensity from each set of (n, k_{max}, N_1) as a function of doping pressure was

normalized to a value of 1. We then calculated the square deviations of the intensities at different pressures between calculation and experiment. The values of N_1 did not affect the general shape of the profile, hence it was set at 600. When the square deviations are plotted against values of n and k_{max}, a trough can be observed as shown in Fig.5.3(a). In the range of n = 1000 – 6000, the trough can be roughly fit with an equation $k_{max} = (n - 600)/600$, as shown by the straight line in the figure. Hence we conclude that in our MPI experiment, a helium reserve of 600 atoms is required to carry the doped droplets into the MPI-TOF, and that the uptake of one room temperature CCl_4 molecule requires 600 helium atoms. We can ignore the bend of Fig. 5.3(a) in the region with n > 6000 based on conditions of our droplet source (16 K at 50 atm) hence the general size range of our droplet beam.[28]

a

b

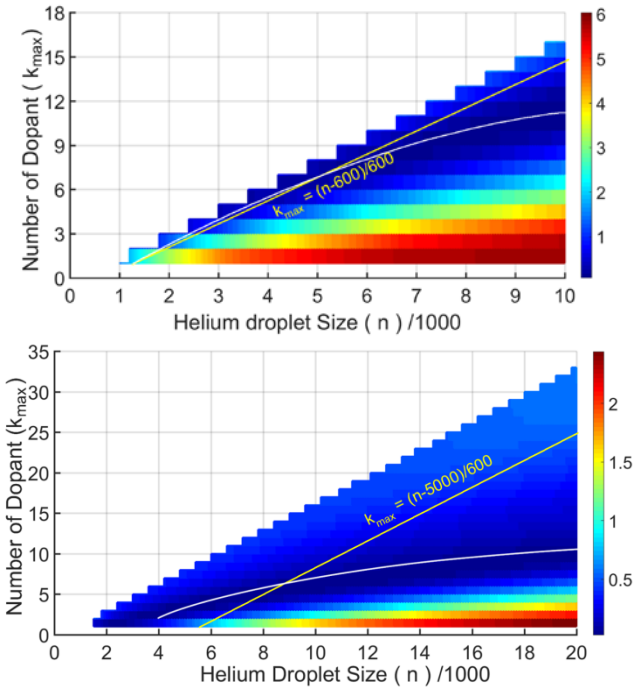

Fig. 5.3. Deviations of simulation results from experimental data plotted as functions of the droplet size n and the maximum number of dopant molecules k_{max} from

experiments of: (a) MPI, and (b) EI under "fixed timing" conditions. The white continuous lines are just guides for the troughs in each panel.

For the experiment under "best timing", at each doping pressure, the intensity from each sized droplets n was calculated according to Eq. 5.2, with the corresponding values of k_{max} chosen from the trough of Fig. 5.3(a). This intensity was then attenuated by the abundance of the corresponding droplet size in a log-normal distribution. The maximum intensity from the whole range of chosen n values was considered the intensity at the chosen doping pressure, and the corresponding n value was considered the sampled droplet size under the "best timing" conditions. The resulting pressure dependence was then normalized and compared with the experimental data. Square deviations of the pressure profiles under "best timing" conditions were obtained and minimized by varying the parameters of the log-normal size distribution. A log-normal size distribution function[31] is specified by two parameters, an average size and a standard deviation.[32] Our minimization process resulted in an optimal average size of 5000 with a standard deviation of 0.85. At a doping pressure of 1×10^{-5} Torr, the largest contribution to the ionization signal was from droplets containing 4700 helium atoms. Fig. 5.4 shows the calculated profiles overlaid with the experimental data for both timing scenarios, with $n = 4700$ and $k_{max} = 6$ for the profile under "fixed timing". Although the agreement is not quantitative, both calculations capture the essence of the experimental data.

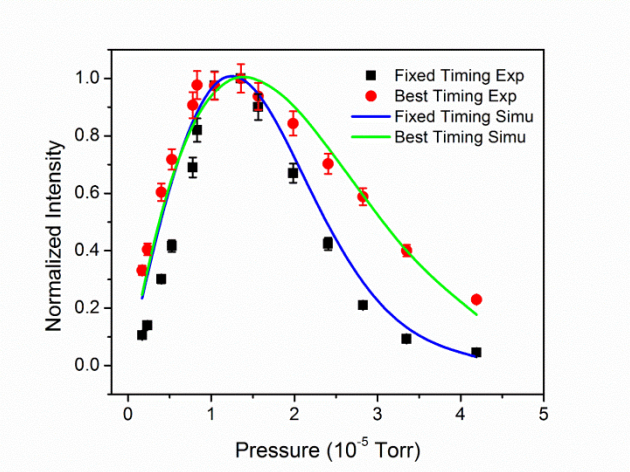

Fig. 5.4. Modeling of the MPI experiment using Eq. 5.2 under different timing conditions. The experimental data are reproduced from Fig. 5.1.

5.4.2 Modeling the EI pressure profiles

Electron impact ionization is dependent on the ionization of helium atoms, while ionization of dopant is a consequence of helium ionization. A different model is therefore required to simulate the EI profiles. The charge hopping model implies that regardless of the number of dopant molecules in a droplet, with the ionization of one helium atom, only one CCl_4 molecule can be ionized to produce one CCl_3^+. The overall ionization signal from the EI experiment is therefore proportional to the collective ionization cross section of the helium atoms in a droplet and the probability of picking up one or more dopant molecules:

$$I_{EI}(\rho; n) \propto \sum_{k=1}^{k_{max}} \sigma_{He} \cdot (n - k \cdot N_1)^{2/3} \cdot P_k(\rho; n) \ . \qquad (5.3)$$

In Eq. 5.3, we have replaced the total ionization cross section of a droplet by $\sigma_{He} \cdot n^{2/3}$ where σ_{He} is the ionization cross section of one helium atom.[15] Based on our numerical calculations, however, replacing the ionization cross section by $\sigma_{He} \cdot n$ does

not make any noticeable difference in the resulting pressure profiles. The mean free path of an electron with a kinetic energy of 300 eV in helium is ~30 Å based on the total collision cross section[33] and the density of superfluid helium[32], hence for a droplet with less than 10^4 helium atoms and with a radius less than 100 Å, almost all helium atoms should have equal probability of being ionized in a droplet.

Equation 5.3 implies that the probability of charge transfer is constant throughout the size range of the probed droplets. This assumption is valid only when the dopant is located at the center of the droplet, and the size range of the sampled droplet, i. e., the square deviation of the log-normal distribution, is reasonably small. Ellis and Yang have modeled the probability of charge transfer by assuming a directed path of a helium cation to the dopant molecule for small sized droplets, and the result shows a more or less constant probability for droplets with average sizes above 2000.[33] The assumption of a directed path should break down for large sized droplets containing more than 50,000 atoms, and experimental results suggest much decreased probability than predicted by the model.[9,34] The calculation by Ellis and Yang was performed for electrons with a kinetic energy of 40 eV, while in our experiment, the impact energy was 300 eV, above the second ionization threshold of helium at 54 eV.[35] This difference can not only affect the total ionization cross section, but also the mechanism of charge transfer. Given the complexity of the situation and the qualitative nature of our model, here we ignore the change in the probability of charge transfer with droplet size, and consequently, we are cautious about any quantitative interpretation of our calculation result.

A few other considerations are included in the calculation of the EI profile. The EI experiment used an electric pulse of 4 μs in duration, much longer than the ionization laser pulse of 5 ns. However, considering the time scale of the velocity slip of several hundred microseconds, it is still reasonable to assume that the EI experiment only probes one sized droplets. The spectrometers for EI and MPI are at two different locations along the path of the droplet beam, and difference in timing between the two ionizing pulses can be calculated based on the average speed of the droplet beam. However, given the width of the EI pulse and the width of the laser pulse in the MPI experiment, this information is insufficient to determine if the EI pulse probes the same sized droplets as the MPI pulse. To reach the EI-TOF after doping, a droplet has to travel an extra 12 cm to reach the ionizer and another 43 cm to reach the detector.[20] This situation requires a much larger droplet with a higher helium reserve than that of the MPI.

Similar to the approach used for the MPI calculation, to simulate the pressure profile of EI under "fixed timing", we normalized intensity distributions calculated from Eq. 5.3 for each n and k_{max} value while fixing N_1 at 600. The resulting pressure profile was compared with the experimental results obtained under "fixed timing", and the square deviations of the intensities are plotted in Fig. 5.3(b). The range of values for n was from 2000 to 20,000, and the range of values for k_{max} was the thermal dynamic limit n/N_1. Compared with the line represented by $k_{max} = (n - 5000)/600$, the trough in the plot of the square deviation has a much smaller slope, implying that more than 600 helium atoms are required to pick up one room temperature CCl_4 molecule and carry it to the EI-TOF.

To simulate the EI profile under the "best timing" conditions, we chose the same average size (5000 atoms/droplet) and standard deviation (0.85) as those from the calculation of the MPI profile to represent the log-normal distribution of the droplet beam. The ionization yield from Eq. 5.3 for each (n, k_{max}) pair in the trough of Fig. 5.3(b) was attenuated by the size distribution and then the highest ion yield was obtained at each doping pressure. The corresponding droplet size was then considered the sampled size in the "best timing" conditions. The resulting pressure profile was normalized and plotted on the same scale as that of the experimental data in Fig. 5.5. The calculation has no adjustable parameters, and the agreement is qualitatively satisfactory. At a doping pressure of 6×10^{-6} Torr, the maximum contribution to the ionization signal was from droplets containing 8300 helium atoms with $k_{max} = 5$, hence the corresponding pressure profile is plotted in Fig. 5 under "fixed timing" conditions. We therefore conclude that under the conditions of our EI-TOF, more than 5000 helium atoms are needed in a doped droplet for detection. While this detection threshold seems large, it is a combination of several factors, including the ionization current of the electron beam, the detection efficiency of the mass spectrometer, and the probability of transport from the doping region to the detector.

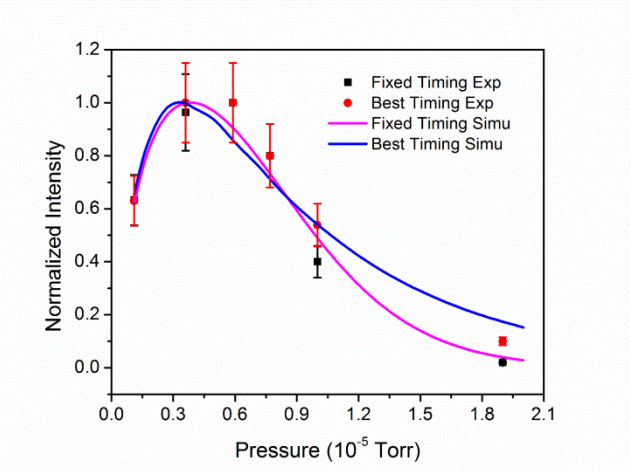

Fig. 5.5. Modeling of the EI experiment using Eq. 5.3 under different timing conditions. The experimental data are reproduced from Fig. 5.1.

Given the crudeness of the pickup model and the ionization models of Eqs.5.2 and 5.3, the agreement of Figs. 5.4 and 5.5 is remarkable. Attempts to simply include an exponential decay function in Eq. 5.3 with a decay constant on the scale of the mean free path of an electron, similar to the method of ref 33, did not result in substantial improvement in the level of agreement. Further improvements in the calculation will perhaps require a numerical simulation of the pickup statistics, for which no closed form analytical expression is possible.

The different behaviors of the MPI and EI experiments under "best timing" conditions can be understood from the following consideration. In the MPI experiment, every additional dopant molecule picked up by a droplet can potentially yield one extra Cl^+. Hence smaller droplets (n = 4700) and higher doping (k_{max} = 6) conditions are favored. The EI experiment is the contrary: once a single dopant molecule is picked up, additional doping is detrimental to the final ion yield. One reason is that doping decreases the ionization cross section by decreasing the droplet

size through helium evaporation. Another reason is that the extra dopant molecule is not ionized to contribute to the observed ion signal since one helium ion can transfer its charge only to one neutral dopant molecule. On the other hand, a higher doping pressure also increases the fraction of doped droplets and hence increasing the ion yield. Consequently, a more delicate balance is required in the EI experiment, resulting in a narrower optimal pressure range for ion production. For a log-normal distribution with an average size of 5000 atoms/droplet and a standard deviation of 0.85, the most probable droplet size is 2000. While the optimal droplet size for the highest ionization yield of MPI is about the same as the average size, the corresponding value for EI is much larger, mostly because of the larger helium reserve (5000).

5.4.3 EI vs MPI: relative yield

A comparison between the relative yields of MPI and EI is informative in understanding the current experimental results. There is no reported three photon absorption cross section for CCl_4 at 266 nm, but the one photon absorption cross section is on the order of 10^{-4} Mb.[36] For a single photon process at 266 nm, with a photon density of over 10^{28} photons/s·cm^2, the probability of excitation in 5 ns is about 10^{-3}. A three photon process should have a comparable excitation probability since we are operating in a partial saturation scheme. In comparison, the effective ionization cross section of 8000 helium atoms is 2.2×10^5 Mb for collisions with electrons at 300 eV,[24] but the density of electrons is limited by the space charge effect to 10^7/cm^3. If the interaction path length between the electrons and the droplets is on the order of 1 cm (the reality was more likely to be 0.5 cm), the probability of

ionization is 10^{-6}, about 0.1% of that of MPI. In the calculations of Figs.5.4 and 5.5, optimal EI requires a size of 8300, while optimal MPI requires a size of 4700. This condition further reduces the yield of EI by a factor of three because of the size distribution of the droplet beam. The deficiency in ionization from the EI experiment can be partially compensated for by the larger sampling fraction of doped droplets, because the ionization volume of EI encompasses the whole doped droplet beam, while only a small fraction of the beam is sampled in the MPI experiment. However, the collection efficiency of the EI-TOF is substantially lower than that of the MPI-TOF because of the longer path length and inefficient space focusing. An unknown factor is the yield of CCl_3^+ for each helium ion in a droplet, and the yield of Cl^+ after multiphoton ionization of one CCl_4. Assuming both unknowns are about the same order of magnitude, the overall signal for EI should be comparable to or weaker than that of MPI. Experimentally, we have observed a three orders of magnitude deficiency in the signal strength of EI.

The above consideration did not include the caging effect of superfluid helium droplets in the MPI process. Less than unity escaping probability of photofragments in superfluid helium droplets has been documented in several previous works.[17,37] For example, Braun and Drabble have investigated photodissociation of CH_3I and its structural analogues at different dissociation wavelength.[37] They have been able to reproduce the escaping probability using a classical binary collision model. The most probable droplet size in our experiment is ~2000 atoms/droplet, much smaller than those used in previous studies. The small mass of a helium atom is ineffective in slowing down a massive fragment like Cl^+.

A word of caution and a solution

Our results tell a cautionary tale in using mass spectrometry to characterize the doping conditions of a droplet beam. Depending on the nature of investigation, the best doping conditions and the best timing of a pulsed droplet beam vary. Electron impact ionization benefits from the collective large ionization cross sections of helium atoms in a droplet, but its sensitivity suffers under heavy doping conditions because of the loss of helium atoms. In this sense, EI is an ideal characterization method for experiments that only concern with singly doped droplets, for example, spectroscopic investigations. The MPI experiment with a moderate laser power, on the other hand, is partially blind to the droplet condition and blind to the presence of dopant clusters, but it is sensitive to the presence of dopant molecules. Caution has to be exerted when using MPI to optimize the doping pressure for experiments of singly doped molecules.

By taking advantage of the velocity slip and the doping statistics, we can devise an approach to maximize the signal from singly doped droplets and to minimize the interference of dopant clusters. If the excitation is pulsed, we can first find the timing of the excitation pulse based on the diagnostic signal at a low doping pressure. This time setting eliminates contributions of larger sized droplets and dopant clusters, regardless of doping conditions. Then we can increase the doping pressure and maximize the dopant related signal. Multiply doped large droplets are too slow to be sampled by the pulsed excitation pulse, and small droplets that survive the doping region should be mostly singly doped. This scheme is more effective for larger dopants with higher heat capacities (larger N_1 value), because evaporative

cooling generates a bigger size difference between singly doped and doubly doped droplets and hence a larger velocity slip. Using this scheme, we have obtained electron diffraction from a droplet beam with 95% of the droplets containing just one ferrocene molecule, and based on analysis of the diffraction pattern, there is no contribution from ferrocene clusters.

5.5 Conclusion

We have compared the characteristics of electron impact ionization and non-resonant multiphoton ionization using the same droplet source. The first event in an EI experiment is ionization of helium atoms in pure or doped droplets, hence the signal of EI is reflective of droplet sizes. The limited photon density of a focused laser beam, on the other hand, has a higher probability of ionizing dopant molecules than helium atoms, hence MPI is only related to the average number of dopant molecules in a droplet. Using a crude model for the pickup statistics and simple models for EI and MPI, we have been able to simulate the pressure profiles of both the EI and MPI experiments performed under different conditions. This comparison offers a word of caution in using different ionization methods for characterization of superfluid helium droplets. Not only the doping pressure for optimal signal strength would be different for EI and MPI, but also the exact timing of arrival of doped droplets in a pulsed droplet beam. On the other hand, this work also alludes to a scheme to reach a high fraction of doping while limiting the contribution of clusters.

Acknowledgement

This work is supported by the National Institute of General Medical Sciences (1R01GM101392-01A1) from the National Institutes of Health and the Environmental Health Science Center at Oregon State University funded by the National Institute of Environmental Health Sciences (ES000210).

5.6 **References**

1 J. P. Toennies and A. F. Vilesov, Angew. Chem., Int. Ed. **43**, 2622 (2004).
2 W. Kong, L. Pei, and J. Zhang, Int. Rev. Phys. Chem. **28**, 33 (2009).
3 S. Yang and A. M. Ellis, Chem. Soc. Rev. **42**, 472 (2013).
4 J. Zhang, L. Chen, W. M. Freund, and W. Kong, J. Chem. Phys. **143**, 074201 (2015).
5 J. Zhang, Y. He, W. M. Freund, and W. Kong, J. Phys. Chem. Lett. **5**, 1801 (2014).
6 J. C. H. Spence and R. B. Doak, Phys. Rev. Lett. **92**, 198102 (2004).
7 M. Mudrich and F. Stienkemeier, Int. Rev. Phys. Chem. **33**, 301 (2014).
8 H. Schöbel, P. Bartl, C. Leidlmair, S. Denifl, O. Echt, T. D. Märk, and P. Scheier, Eur. Phys. J. D **63**, 209 (2011).
9 S. Yang, S. M. Brereton, M. D. Wheeler, and A. M. Ellis, J. Phys. Chem. A **110**, 1791 (2006).
10 M. N. Slipchenko, S. Kuma, T. Momose, and A. F. Vilesov, Rev. Sci. Instrum. **73**, 3600 (2002).
11 H. Buchenau, J. P. Toennies, and J. A. Northby, J. Chem. Phys. **95**, 8134 (1991).
12 T. Ruchti, K. Forde, B. E. Callicoatt, H. Ludwigs, and K. C. Janda, J. Chem. Phys. **109**, 10679 (1998).
13 H. Schöbel, M. Dampc, d. S. F. Ferreira, A. Mauracher, F. Zappa, S. Denifl, T. D. Märk, and P. Scheier, Int. J. Mass Spectrom. **280**, 26 (2009).
14 A. Scheidemann, B. Schilling, and J. P. Toennies, J. Phys. Chem. **97**, 2128 (1993).
15 B. E. Callicoatt, D. D. Mar, V. A. Apkarian, and K. C. Janda, J. Chem. Phys. **105**, 7872 (1996).
16 D. S. Peterka, J. H. Kim, C. C. Wang, L. Poisson, and D. M. Neumark, J. Phys. Chem. A **111**, 7449 (2007).
17 D. S. Peterka, J. H. Kim, C. C. Wang, and D. M. Neumark, J. Phys. Chem. B **110**, 19945 (2006).
18 S. A. Krasnokutski and F. Huisken, J. Chem. Phys. **142**, 084311 (2015).
19 X. Zhang and M. Drabbels, J. Phys. Chem. Lett. **5**, 3100 (2014).

[20] Y. He, J. Zhang, Y. Li, W. M. Freund, and W. Kong, Rev. Sci. Instrum. **86**, 084102 (2015).
[21] Y. Ovcharenko, V. Lyamayev, R. Katzy, M. Devetta, A. La Forge, P. O'Keeffe, O. Plekan, P. Finetti, M. Di Fraia, M. Mudrich, M. Krikunova, P. Piseri, M. Coreno, N. B. Brauer, T. Mazza, S. Stranges, C. Grazioli, R. Richter, K. C. Prince, M. Drabbels, C. Callegari, F. Stienkemeier, and T. Moeller, Phys. Rev. Lett. **112**, 073401 (2014).
[22] Y. J. Kime, D. C. Driscoll, and P. A. Dowben, J. Chem. Soc., Faraday Trans. 2 **83**, 403 (1987).
[23] Y.-L. He and L. Wang, Struct. Chem. **20**, 461 (2009).
[24] *Electron-impact cross sections for ionization and excitation*, edited by Y.-K. Kim, K. K. Irikura, M. E. Rudd, M. A. Ali, P. M. Stone, J. Chang, J. S. Coursey, R. A. Dragoset, A. R. Kishore, K. J. Olsen, A. M. Sansonetti, G. G. Wiersma, D. S. Zucker, and M. A. Zucker (National Institute of Standards and Technology, Gaithersburg MD, 20899, 2011).
[25] G. R. Burton, W. F. Chan, G. Cooper, and C. E. Brion, Chemical Physics **181**, 147 (1994).
[26] S. Yang and A. M. Ellis, Rev. Sci. Instrum. **79**, 016106 (2008).
[27] M. Hartmann, R. E. Miller, J. P. Toennies, and A. F. Vilesov, Science **272**, 1631 (1996).
[28] L. F. Gomez, E. Loginov, R. Sliter, and A. F. Vilesov, J. Chem. Phys. **135**, 154201 (2011).
[29] M. Lewerenz, B. Schilling, and J. P. Toennies, J. Chem. Phys. **102**, 8191 (1995).
[30] L. S. Cederbaum, J. Zobeley, and F. Tarantelli, Physical Review Letters **79**, 4778 (1997).
[31] M. Lewerenz, B. Schilling, and J. P. Toennies, Chem. Phys. Lett. **206**, 381 (1993).
[32] J. Harms, J. P. Toennies, and F. Dalfovo, Phys. Rev. B **58**, 3341 (1998).
[33] A. M. Ellis and S. Yang, Phys. Rev. A: At., Mol., Opt. Phys. **76**, 032714 (2007).
[34] W. K. Lewis, B. E. Applegate, J. Sztaray, B. Sztaray, T. Baer, R. J. Bemish, and R. E. Miller, J. Am. Chem. Soc. **126**, 11283 (2004).
[35] Z. Zhang, L.-Y. Peng, M.-H. Xu, A. F. Starace, T. Morishita, and Q. Gong, Phys. Rev. A: At., Mol., Opt. Phys. **84**, 043409 (2011).
[36] C. Hubrich and F. Stuhl, J. Photochem. **12**, 93 (1980).
[37] A. Braun and M. Drabbels, J. Chem. Phys. **127**, 114303 (2007).

Chapter 6 Electron diffraction of CBr_4 in superfluid helium droplets: a step towards single molecule diffraction

Yunteng He, Jie Zhang, and Wei Kong*

Department of Chemistry, Oregon State University, Corvallis, OR 97331-4003

Journal of Chemical Physics

1305 Walt Whitman Road Suite 300

Melville, NY 11747-4300

145, 034307 (2016)

*Corresponding author, wei.kong@oregonstate.edu, 541-737-6714

Abstract

We demonstrate the practicality of electron diffraction of single molecules inside superfluid helium droplets using CBr_4 as a testing case. By reducing the background from pure undoped droplets via multiple doping, with small corrections for dimers and trimers, clearly resolved diffraction rings of CBr_4 similar to those of gas phase molecules can be observed. The experimental data from CBr_4 doped droplets are in agreement with both theoretical calculations and with experimental results of gaseous species. The abundances of monomers and clusters in the droplet beam also qualitatively agree with the Poisson statistics. Possible extensions of this approach to macromolecular ions will also be discussed. This result marks the first step in building a molecular goniometer using superfluid helium droplet cooling and field induced orientation. The superior cooling effect of helium droplets is ideal for field induced orientation, but the diffraction background from helium is a concern. This work addresses this background issue and identifies a possible solution. Accumulation of diffraction images only becomes meaningful when all images are produced from molecules oriented in the same direction, and hence a molecular goniometer is a crucial technology for serial diffraction of single molecules.

6.1. Introduction

Single molecule diffraction has been considered the ultimate promise of overcoming the difficulty of crystallization in protein crystallography.[1,2] The much weaker diffraction signal from single molecules, as compared with single crystals (even nanocrystals), is to be compensated for by the newly available intense ultrashort x-ray pulses from free-electron lasers. However, the ultimate limit on single molecule diffraction is not imposed by the available facility, but rather by the molecules, i. e., the internal potential of the molecular system, since the probe has to be at largest a perturbation to the molecular Hamiltonian.[3] Alternatively, electron diffraction of a stream of identically oriented single molecules allows accumulation of images for the desired signal-to-noise ratio, hence this method has much milder requirements on the light source and the detector.[4-6] Moreover, using DC or laser fields, several groups have demonstrated orientation of gas phase molecules.[7-10] The thus obtained molecular goniometer relies on the interaction between the electric field and the permanent dipole (DC field orientation) or polarizability anisotropy (laser induced alignment) of the molecule, to overcome the rotational energy of the molecule. Unfortunately, adaptation of these gas phase methods for macromolecular protein ions is subject to the constraints of the sample's high fragility and low volatility. Supersonic molecular beams are inefficient in cooling the massive protein molecules from either a laser desorption ionization source [11] or an electrospray ionization (ESI) source.[12,13] Superfluid helium droplets with a terminal temperature of 0.38 K and a frictionless environment thus emerge as an ideal coolant.[14] Moreover, efficient interface of a superfluid helium droplet source with an electrospray ionization source

has already been demonstrated in more than one laboratory.[15-17] A price for the extreme cooling of superfluid helium droplets, on the other hand, is the diffraction background from helium atoms of the droplet beam.[18] A central issue is therefore the possible existence of an experimental condition where the droplet size is small enough or the sample concentration is high enough that molecular interference from the sample molecules is still observable above the atomic diffraction background of the helium atoms.

Here we demonstrate the feasibility of electron diffraction of molecules embedded in superfluid helium droplets. By varying the degree of doping and modeling the role of undoped droplets in the diffraction process, we conclude that the most important contributor of the diffraction background is the undoped droplets. For neutral dopants, this issue can be resolved by increasing the concentration of dopant molecules in the droplet beam thereby producing droplets doped with multiple dopant molecules, as long as intermolecular diffraction from dimers and trimers can be accounted for. This approach has the added bonus of thinning the surrounding helium jacket to a negligible level for the doped molecules. Compared with our previous report on phthalocyanine gallium chloride (PcGaCl),[18] this work identifies a crucial factor in extending the technology from gaseous species to macromolecular ions. The newly obtained quantitative information enables us to estimate the recording time for macromolecular ions based on a desired resolution.

6.2. Experimental setup

The droplet source is pulsed and the pulsed valve is kept at 18 K with a stagnation pressure of 50 atm. The droplet beam passes through a doping region filled with CBr_4 and picks up one or more dopant molecules.[19] In the diffraction region, a synchronized pulsed collimated electron beam spatially and temporally overlaps with the doped droplets, and the resulting diffracted electrons are detected by a phosphor screen and a camera. A background image is measured between two consecutive droplet pulses, and the images from the droplet pulse and from the background are accumulated separately in a computer. The difference between the two accumulated images is the net diffraction from the droplets, with and without dopant. Hence the effective repetition rate of the overall experiment is 5 Hz, while the data acquisition rate of the camera is 10 Hz.

To characterize the droplet beam and its doping conditions, two time-of-flight mass spectrometers are used, one in-line with the droplet beam located at the exit of the diffraction chamber, and the other perpendicular to the droplet beam located below the diffraction region.[20] Relying on electron impact ionization (EI) and non-resonant multiphoton ionization (MPI), we have determined that the most probable size of our droplet beam is ~2000 helium atoms/droplet, in agreement with the general result by Gomez et al.[21] We have also determined that doping of one CBr_4 molecule requires evaporation of ~600 helium atoms.[22] An important feature of the pulsed droplet beam is velocity slip among different sized droplets: the overall droplet beam spans over 200 μs in the diffraction region, but depending on the timing of the ionization laser, different sized droplets are sampled in the MPI experiment.

6.3. Results

Gas phase electron diffraction of randomly distributed molecules is typically plotted on the scale of momentum transfer *s* defined as:[23]

$$s = \frac{4\pi}{\lambda}\sin(\frac{\theta_d}{2}) \,, \tag{6.1}$$

where λ is the de Broglie wavelength (0.06 Å at 40 keV), and θ_d is the diffraction angle. Each unique pair of atoms (correlated pair) generates a set of rings for randomly oriented samples, and the structure-sensitive component is typically expressed in terms of a modified molecular scattering intensity *sM(s)*:

$$sM(s) = \frac{sI_{mol}(s)}{I_{at}(s)} = s\frac{I_{tl}(s)-I_{at}(s)}{I_{at}(s)} = s\frac{I_{mol}(s)}{I_{at}(s)} - s \,, \tag{6.2}$$

where contributions of all the atoms of the diffractive species are collectively represented by $I_{at}(s)$, the coherent sum of diffractions from each correlated pair is represented by $I_{mol}(s)$, and the total diffraction intensity $I_{tl}(s)$ includes both atomic and molecular diffraction.

Compared with typical gas phase electron diffraction experiments,[23] our diffraction pattern contains contributions not only from the sample molecule but also from the surrounding helium atoms and small molecular clusters due to multiple doping of one droplet. The relative contributions of these effects depend on the experimental conditions, including the pressure and path length of the doping region and the droplet size and hence the pressure and temperature of the pulsed valve. We compare the theoretical modified molecular scattering intensity *sM(s)* of CBr_4 and the experimental data using the equation:

$$sM(s) = \frac{A_s \cdot I_{total}(s) - A_d \cdot I_{droplet}(s) - A_b \cdot I_{background}(s) - C_c \cdot I_{T,c}(s)}{I_{T,at}(s)} \cdot s - s + C, \quad (6.3)$$

where $I_{total}(s)$, $I_{droplet}(s)$, and $I_{background}(s)$ are intensities from the experiment of doped droplets, pure droplets, and background, A_s, A_d and A_b are the corresponding fitting parameters, $I_{T,at}(s)$ is the theoretical diffraction intensity from the atoms of the dopant molecule,[18] and C is for baseline correction. Parameters C_c and $I_{T,c}(s)$ are related to multiply doped CBr_4. Among contributions of intermolecular atomic pairs from clusters, the most intense should come from Br ⋯ Br pairs, and the most prominent in the diffraction image should be from the shortest Br ⋯ Br intermolecular pairs. This is because the most intense contributions from other longer distance pairs are distributed closer to the Faraday cup and are hence blocked out by the cup and its halo. In Eq.6.3, $I_{T,c}(s)$ is the theoretical diffraction profile of the shortest Br ⋯ Br pair with a separation of 4 Å,[24-26] and C_c is the weight of the theoretical contribution of the cluster in the overall diffraction. The quantities I_{total}, $I_{droplet}$, and $I_{background}$ are experimental values directly from the diffraction image, and both I_{total} and $I_{droplet}$ should contain some degrees of $I_{background}$. In particular, I_{total} and $I_{droplet}$ are obtained under the same exposure conditions, thus independent variations of A_s and A_d in Eq. 2 allow adequate account for the difference in flux between the doped droplet beam and the undoped droplet beam, and loss of helium atoms due to doping. The quantity of $I_{T,c}$, on the other hand, is a theoretical value from calculation.[18] Thus while C_c represents the contribution of clusters relative to that of monomers, the contribution of undoped (pure) droplets to the overall signal should be A_d/A_s.

The inset of Fig. 6.1 shows the diffraction image and radial profile after quadrant averaging, Wiener filtering,[27] and removal of intermolecular diffraction from CBr_4 clusters. The radial profiles of different components are shown in the main part of Fig. 6.1. There the total experimental radial distribution ("Total Exp") is compared with the scaled theoretical contribution of clusters in the form of Br ⋯ Br interference denoted "Br ⋯ Br Calculation", and the difference between the experimental data and this theoretical component is labeled as "Exp w/o Br⋯Br". The latter profile should be compared with the theoretical diffraction profile labeled as "CBr_4 Calculation". The halo of the Faraday cup is not included in the profiles. The experimental corrected radial profile contains one clearly observable ring, corresponding to the feature at s = 2.5 $Å^{-1}$ and a weaker feature at about 4.3 $Å^{-1}$.

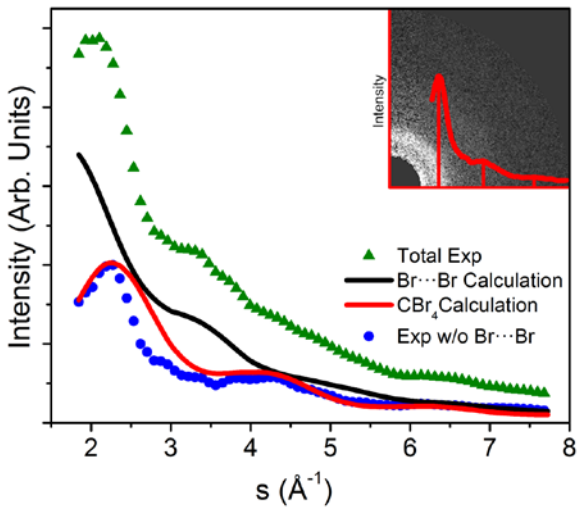

Fig. 6.1. Radial profiles relevant to diffraction from CBr_4 doped superfluid helium droplets. The inset shows the image after treatment using the Wiener filter and after removing contributions from molecular clusters assuming a Br⋯Br pair with a separation of 4 Å. The profile "Exp w/o Br⋯Br" was obtained by subtracting the

theoretical contribution from clusters ("Br···Br Calculation") from the overall experimental profile ("Total Exp"), which should be compared with the theoretical profile from CBr_4 including both atomic and molecular contributions ("CBr_4 Calculation").

We have also recorded gas phase electron diffraction images of CBr_4 by injecting the gaseous sample through a needle positioned directly in place of the droplet beam. The radial profiles and the corresponding pair correlation functions are shown in Fig. 6.2, and they are both similar to those from a previous report [28] (not shown in Fig. 6.2). It is important to note that the "doped" trace in Fig. 6.2 is the net difference recorded with and without the droplet beam, while the doping chamber was maintained at a constant pressure. Contributions from the diffused gas in the trace of the "doped" sample are therefore removed. Nevertheless, the doped sample shows a similar diffraction profile as the gaseous sample, and both experimental results are similar to the theoretical calculation.[18] Although the gaseous sample was at room temperature while the doped sample was at 0.38 K, the predominant factor that determines the width of each interference ring is the wave physics, not the vibrational movement of the atoms in a molecule.[23] Evidently the superfluid helium environment exerts negligible perturbation to the enclosed molecular structure. The weak features near the major features centered at 4.5 and 6.5 $Å^{-1}$ in the *sM(s)* profile from the doped sample could be due to residual contributions from clusters of CBr_4. The same argument is applicable to the pair correlation profiles, where the profile from the doped sample also contains an extra shoulder near 4 Å.

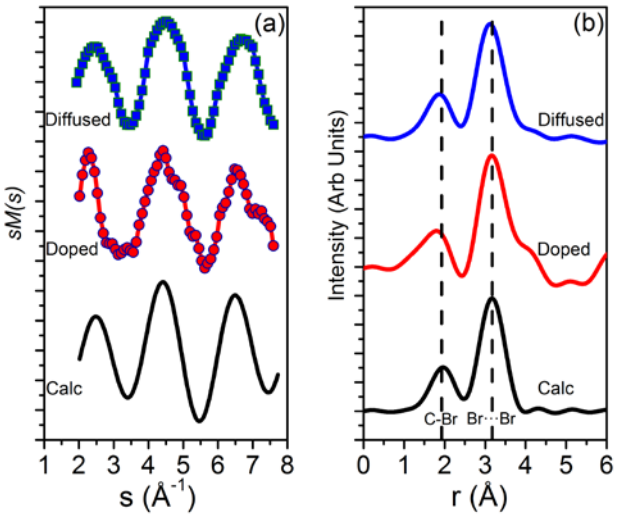

Fig. 6.2. Comparisons of results from gaseous and doped CBr_4 with theoretical calculations: (a) molecular diffraction profiles *sM(s)*, and (b) pair correlation functions.

Different from a diffused sample, however, a droplet can pick up a number of molecules *k* with a probability P_k,[20,22] thus diffraction of the droplet beam contains contributions from dopant clusters as well as undoped pure droplets. The contribution of pure droplets from the fitting of Eq. 6.3, A_d/A_s, should be proportional to P_0, the probability of not picking up any dopant. The contribution of dopant molecular clusters C_c should be proportional to the ratio between the number of intermolecular Br ⋯ Br pairs with a separation of 4 Å and the average number of dopant molecules in a droplet $<k>$:

$$< k > = \sum_k k \cdot P_k \ . \qquad (6.4)$$

If we assume that the electron gun samples the most probable size of the droplet beam of 2000, there should be at maximum 3 dopant molecules in a droplet. Since there are

3 equivalent Br ⋯ Br pairs with a separation of 4 Å in a dimer and 4 such pairs in a trimer,[26] the value of C_c should be proportional to $(3P_2 + 4P_3)/\langle k \rangle$.

To model the doping statistics, we have to take into consideration the polydispersity of the droplet beam. Fortunately, the velocity slip among different sized droplets and the limited duration of the electron beam (16 μs) determines that the electron beam only samples droplets in a limited size range, and for simplicity, we only need to consider one group of fixed sized droplets, similar to our previous work on EI and MPI of doped droplets.[20] Depending on the relative timing of the electron beam to the droplet beam, different sized droplets are sampled. We do not have the direct information on the size of the sampled droplets of this experiment, however, based on the MPI experiment,[20] we are certain that the droplet size sampled in the diffraction experiment should be smaller than the average size of the droplet beam. Thus we choose the most probable size in modeling the doping statistics. In addition, we have also discovered that the actual size does not affect the qualitative conclusion of the calculation within a range of 1800 and 3000 atoms/droplet, given the uncertainty of the experimental data.

Fig. 6.3 compares the experimental fitting results with the Poisson statistics. Fig. 6.3(a) shows the contribution of pure undoped droplets relative to that of doped droplets, and the ratio (vertical axis) is expected to be proportional to the probability of undoped droplets. At a doping pressure of 1×10^{-5} Torr, less than 15% of the droplets are undoped, and this value is reproduced from the experimental fitting value of A_d/A_s. With increasing doping pressure, more and more droplets are doped, and the

portion of undoped pure droplets decreases accordingly. At the lowest doping pressure, the error bar is considerably large and a disagreement exists. We attribute this point to the residual gas in the doping chamber, since the base pressure in the doping chamber without any doping gas was 1×10^{-6} Torr.

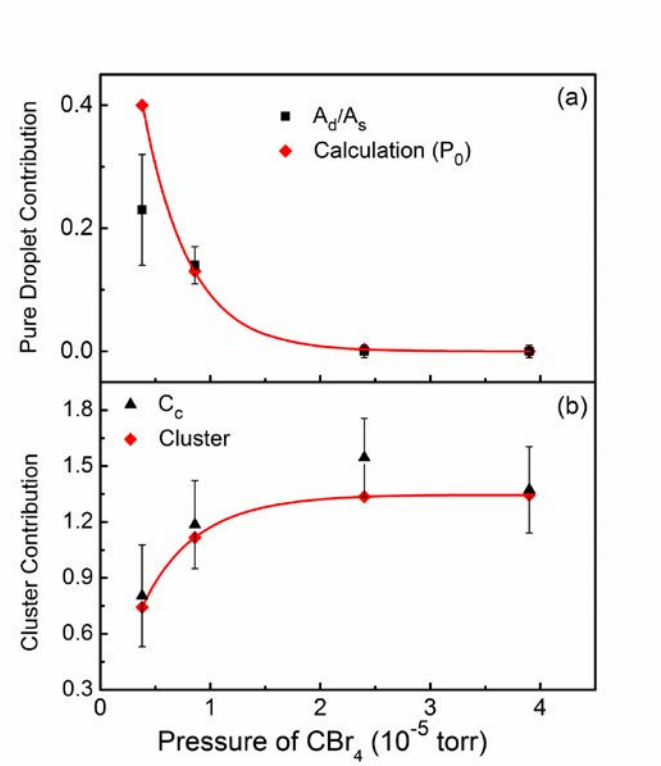

Fig. 6.3 Comparisons between Poisson statistics and experimental results. (a) Calculated probabilities of undoped droplets P_0 in a droplet beam and fitting results A_d/A_s from experiment. (b) Contributions of CBr_4 clusters C_c from experiment and calculated ratios of cluster and monomer contributions (designated as "Cluster").

A coincidence in the diffraction cross section plays a role in the agreement of Fig. 6.3(a) at higher doping pressures, even though the doped droplets are smaller than the undoped droplets under the same droplet source conditions. The adsorption of one

CBr_4 molecule removes 600 helium atoms from the surface of the droplet,[22] and incidentally, at the electron wavelength of 0.06 Å, the total atomic diffraction cross section of one CBr_4 molecule is roughly the same as those of 600 helium atoms.[29] Hence the experimental diffraction intensities of doped droplets and pure droplets are not substantially modified by the change in size due to sample pickup.

Fig. 6.3(b) compares the contribution of clusters calculated using $(3P_2 + 4P_3)/\langle k \rangle$ (designated as "Cluster" in the figure) based on the Poisson statistics[19,20] with the experimental fitting value for clusters C_c. At a doping pressure of 1×10^{-5} Torr, contributions of clusters relative to those of monomers is slightly more than 1:1, and this ratio increases to 1.3:1 at higher doping pressures. This upper limit is attributed to the maximum number of molecules that an average sized cluster can pick up before it is destroyed completely. The coefficients of P_2 and P_3 in the expression $(3P_2 + 4P_3)/\langle k \rangle$ do not play a critical role when varied between 3 and 6: they only affect the scaling of the profile, not the general trend.

6.4. Discussion

The above comparison highlights the crucial issue in using superfluid helium droplets as an ultra cold gentle matrix for electron diffraction from field aligned and/or oriented molecules, i. e., the helium background. In our previous work on phthalocyanine gallium chloride[18], we were limited by the experimental condition to only explore the regime of low doping pressures. However, based on the Poisson model, if the doping pressure in an oven of 2.5 cm (from our experiment of PcGaCl, different from the current doping cell) is 1×10^{-5} Torr, more than 82% of the droplets

will not pick up any number of molecules and will only contribute to the monotonic background in the diffraction pattern. This large unwanted diffraction intensity can potentially overwhelm the detector. This issue should be much more severe for an ion doped droplet beam, since the equivalent vapor pressure of ions at the space charge limit is only 10^{-9} Torr,[15] hence more than 99% of the droplets contain no protein ions at all even in the unrealistically favorable assumption of Poisson statistics.[30] Under low doping conditions, it is therefore the presence of undoped droplets that will dominate the background, and hence elimination of undoped droplets is essential for reducing the background of helium.

To overcome this issue, neutral molecules can be heavily doped by increasing the doping pressure or path length as shown in Fig. 6.3(b), but this approach is complicated by the formation of clusters. Fortunately, contributions from clusters tend to be in the low *s* region close to the Faraday cup because of the longer distances between intermolecular pairs,[31] and data in this region are fortunately either blocked by the Faraday cup or can be discarded during data processing. Moreover, by multiple doping, the size of a helium droplet is reduced, resulting in further reduction in the helium background.

For charged species, elimination of neutral undoped droplets from the charged doped droplets is straightforward using electric fields (magnetic fields are generally avoided because of the difficulty in field containment for electron diffraction). An ion doped droplet beam can be bent from the initial path via an electric field generated by a

stack of electrodes in, for example, a reflectron type of design, which also has the benefit of compressing the droplet pulse spatially and temporally. Alternatively, charged droplets can be accelerated or decelerated relative to the neutral undoped droplets, while the pulsed orientation laser and electron gun can be synchronized to interact only with the doped beam. Electrostatic steering has the additional benefit of size selection, which could be used to eliminate excessively large droplets due to their high helium content hence large background contribution. Moreover, collisional size reduction of neutral doped molecules has been demonstrated in the literature,[32] and its application to charged droplets has been successfully demonstrated in our own laboratory.

The quality of the diffraction signal in this experiment represents a major step forward compared with our previous work on PcGaCl.[18] However, further improvements are needed to expand to diffractions of macromolecular ions. One such improvement is to expand the central region of the diffraction image, since the diffraction intensity scales with s^{-4}. Experimentally this involves lowering the phosphor screen so to minimize the footprint of the Faraday cup. Based on Bragg's law, to determine a minimum distance (resolution) of 1.5 Å using a light source of 0.06 Å, the minimum diffraction angle should be 1.1º. The scale of Fig. 6.1 extends to a diffraction angle of 2.2º (s = 8 Å^{-1}), hence there is at least a factor of 10 to be gained in the diffraction intensity, if we were to reduce the data range to the minimum angle determined by the desired resolution. This measure also benefits detections of larger spatial dimensions, for example macromolecules such as proteins, since a

longer distance translates into a smaller diffraction angle and a smaller *s* number. Another improvement is in hardware: more gains are possible with improved electron detectors, and faster data acquisition at higher repetition rates can also speed up the experiment. For the latter, bigger vacuum pumps for the gas load and faster cameras for data transfer are both viable options. Altogether, Fig. 6.1 is the result of 460,000 shots, and to reach a resolution of 1.5 Å without any improvement in hardware, ~50,000 shots or 5,000 seconds at 10 Hz, are needed for each projection, and to reconstruct a 3-dimensional structure, several projections (hence hours) are necessary. To extend to macromolecular ions that suffer from the space charge limit in concentration, significant improvements in hardware, particularly repetition rates and electron detection efficiencies, are still needed. An advantage of macromolecular ions, on the other hand, is that they can be trapped in the diffraction region for a much longer time than the traveling neutral droplet beam, which could to some degree compensate for its low particle density.

The need of superfluid helium droplet cooling in single molecule electron diffraction is justified by the achievable spatial resolution via orientational control. At 0.38 K, a green fluorescing protein with a polarizability volume of 28,000 $Å^3$ can be confined in a cone of 1º in a laser field of 10^9 W/cm^2.[6] This moderate requirement for such a high degree of alignment is only possible because of the superior cooling effect of superfluid helium droplets. Although background diffraction from helium poses a bigger threat in image contrast when only carbon, nitrogen, and oxygen atoms are present in proteins, the net charges on protein doped helium droplets allow size

selection and reduction using electrostatic fields thereby minimizing the unwanted helium content.

In conclusion, we have demonstrated the practicality of performing electron diffraction of molecules doped in superfluid helium droplets. We have learned that when the droplet size is controlled to a few thousand atoms, the major diffraction background is from helium atoms of undoped droplets. This problem can be solved by increasing the dopant concentration in the droplet beam for neutral molecules, since the contribution of molecular clusters is largely limited to the central region of the diffraction image, in the shadow of the Faraday cup. This work confirms the practicality of using superfluid helium droplets for rotational cooling therefore the potential for field induced orientation in single molecule diffraction. The superior cooling capability of superfluid helium can significantly reduce the necessary field strength for effective orientation, particularly for macromolecules such as proteins. The thus obtained molecular goniometer should be applicable in serial crystallography, using either x-ray photons or electrons.

Acknowledgement

This work is supported by the National Institute of General Medical Sciences (1R01GM101392-01A1) from the National Institutes of Health and the Environmental Health Science Center at Oregon State University funded by the National Institute of Environmental Health Sciences (ES000210). Advice from Dr. J. P. Toennies is deeply appreciated.

6.5. References

1 I. Schlichting, IUCrJ **2**, 246 (2015).
2 R. Neutze, R. Wouts, D. van der Spoel, E. Weckert, and J. Hajdu, Nature (London, U. K.) **406**, 752 (2000).
3 A. Fratalocchi and G. Ruocco, Phys. Rev. Lett. **106**, 105504 (2011).
4 J. Yang, V. Makhija, V. Kumarappan, and M. Centurion, Struct. Dyn. **1**, 044101 (2014).
5 F. Filsinger, G. Meijer, H. Stapelfeldt, H. N. Chapman, and J. Kuepper, Phys. Chem. Chem. Phys. **13**, 2076 (2011).
6 J. C. H. Spence and R. B. Doak, Phys. Rev. Lett. **92**, 198102 (2004).
7 H. Sakai, Adv. Multi-Photon Processes Spectrosc. **18**, 107 (2008).
8 V. Kumarappan, S. S. Viftrup, L. Holmegaard, C. Z. Bisgaard, and H. Stapelfeldt, Phys. Scr. **76**, C63 (2007).
9 W. Kong, Int. J. Mod. Phys. B **15**, 3471 (2001).
10 B. Friedrich and D. Herschbach, Int. Rev. Phys. Chem. **15**, 325 (1996).
11 C. N. McEwen and B. S. Larsen, Int. J. Mass Spectrom. **377**, 515 (2015).
12 C. W. Klampfl and M. Himmelsbach, Anal. Chim. Acta **890**, 44 (2015).
13 L.-S. Wang, J. Chem. Phys. **143**, 040901 (2015).
14 J. P. Toennies and A. F. Vilesov, Angew. Chem., Int. Ed. **43**, 2622 (2004).
15 J. Zhang, L. Chen, W. M. Freund, and W. Kong, J. Chem. Phys. **143**, 074201 (2015).
16 F. Filsinger, D.-S. Ahn, G. Meijer, and G. von Helden, Phys. Chem. Chem. Phys. **14**, 13370 (2012).
17 F. Bierau, P. Kupser, G. Meijer, and G. von Helden, Phys. Rev. Lett. **105**, 133402 (2010).
18 J. Zhang, Y. He, W. M. Freund, and W. Kong, J. Phys. Chem. Lett. **5**, 1801 (2014).
19 M. Hartmann, R. E. Miller, J. P. Toennies, and A. F. Vilesov, Science **272**, 1631 (1996).
20 Y. He, J. Zhang, and W. Kong, J. Chem. Phys. **144**, 084302 (2016).
21 L. F. Gomez, E. Loginov, R. Sliter, and A. F. Vilesov, J. Chem. Phys. **135**, 154201 (2011).
22 M. Lewerenz, B. Schilling, and J. P. Toennies, J. Chem. Phys. **102**, 8191 (1995).
23 L. O. Brockway, Rev. Mod. Phys. **8**, 231 (1936).
24 M. Capdevila-Cortada and J. J. Novoa, CrystEngComm **17**, 3354 (2015).
25 R. Mahlanen, J.-P. Jalkanen, and T. A. Pakkanen, Chem. Phys. **313**, 271 (2005).
26 M. R. Chowdhury and J. C. Dore, J. Non-Cryst. Solids **46**, 343 (1981).
27 K. Kondo, Y. Ichioka, and T. Suzuki, Appl. Opt. **16**, 2554 (1977).
28 H. Thomassen and K. Hedberg, J. Mol. Struct. **240**, 151 (1990).
29 R. A. Bonham and E. W. Ng, Chem. Phys. Lett. **4**, 355 (1969).
30 L. Chen, J. Zhang, W. M. Freund, and W. Kong, J. Chem. Phys. **143**, 044310 (2015).
31 L. S. Bartell, Annu. Rev. Phys. Chem. **49**, 43 (1998).

[32] M. Hartmann, N. Portner, B. Sartakov, J. P. Toennies, and A. F. Vilesov, J. Chem. Phys. **110**, 5109 (1999).

Chapter 7 Electron Diffraction of Ferrocene in Superfluid Helium Droplets

Jie Zhang, Yunteng He, and Wei Kong*

Department of Chemistry, Oregon State University

Corvallis, OR 97331, USA

Journal of Chemical Physics

1305 Walt Whitman Road Suite 300

Melville, NY 11747-4300

144, 221101 (2016)

*Corresponding author, 541-737-6714, wei.kong@oregonstate.edu

Abstract

We report electron diffraction of ferrocene doped in superfluid helium droplets. By taking advantage of the velocity slip in our pulsed droplet beam using a pulsed electron gun, and by doping with a high concentration of ferrocene delivered via a pulsed valve, we can obtain high quality diffraction images from singly doped droplets. Under the optimal doping conditions, 80% of the droplets sampled in the electron beam are doped with just one ferrocene molecule. Extension of this size selection method to dopant clusters has also been demonstrated. However, incomplete separation of dopant clusters might require deconvolution and modeling of the doping process. This method can be used for studies of nucleation processes in superfluid helium droplets.

7.1 Introduction

Gas phase electron diffraction (GED) has long been a high precision structural tool, with resolutions on the order of hundredths of Angstroms, thanks to the much shorter wavelengths and the much larger diffraction cross sections of high energy electrons than those of x-ray photons.[1] In recent years, GED has been adapted for time-domain investigations of structural evolutions of photochemical reactions.[2,3] The large scattering cross sections of electrons, however, have also limited the penetration depth of an electron beam, hence for condensed phase studies in the transmission mode, electron diffraction is only applicable for ultrathin samples. Incidentally, the nucleation or condensation process of vapor phase molecules produces nanoscale naturally thin samples, and hence electron diffraction is ideally suited for studies of structural evolutions of nanomaterials.

Superfluid helium droplets have recently been recognized as an interesting medium for nucleation events,[4,5] and a flurry of activities in growing esoteric species in superfluid helium droplets have been reported.[6,7] Although one of the initial motivations was to use the dopant atoms as probes for vortices in droplets,[8,9] the field has recently expanded to potential means of producing core-shell structures of nanomaterials.[10] Characterization of the resulting solid structure has so far relied on depositing doped droplets on a substrate and then analysis using transmission electron microscopes. The post deposition analysis procedure reveals the final product of doping, after evaporation of helium and after equilibration with the substrate, without information of the nucleation process.

Here we report a possible approach to perform electron diffraction of size selected doped droplets, with the potential of obtaining structures of doped droplets prior to deposition. Unlike spectroscopic studies where the excitation and

detection methods are intrinsically sensitive to only doped droplets, electron diffraction is sensitive to all particles in an electron beam, including undoped droplets. Thus incorporation of superfluid helium droplets for diffraction also comes with a price: the helium jacket has to be thin enough not to generate a substantial background.[11] In addition, undoped droplets, a byproduct of incomplete doping, are also problematic.[12] In our previous work, we have demonstrated that by increasing the number of doped molecules per droplet, we can overcome the background issue, and that our diffraction pattern contains definitive contributions of dopant monomers, dimers and trimers.[12] We have also performed a thorough investigation of the size distribution and doping statistics of our droplet beam.[13] This observation has led us to a proposal of achieving diffraction of singly doped droplets without the interference of dopant clusters. Here we demonstrate this idea using electron diffraction of ferrocene. Different from other experiments of neutral dopants, we have used a pulsed valve to deliver gas phase ferrocene. Our diffraction image shows only contributions from ferrocene monomers, and our analysis reveals that more than 80% of the droplets contain exactly one dopant molecule. The agreements between experimental and calculated diffraction patterns and pair correlation profiles are exceptional.

7.2 Experimental setup

We have used two pulsed valves for droplet formation and for sample doping, and the overall setup is shown in Fig. 7.1. Details of the helium droplet source and the gas phase electron diffraction system have been described in our previous publications.[11,12,14] Superfluid helium droplets were formed by supersonic expansion of precooled ultrapure helium (99.9995%) from an Even-Lavie pulsed

valve (referred to as the droplet PV in the following). The droplet beam was further collimated by a skimmer with an orifice of 2 mm in diameter about 11 cm downstream from the droplet PV. In the doping chamber, another pulsed valve (Parker, series 9, referred to as the sample PV) with a homemade nozzle housed the ferrocene sample and was heated to 73ºC. The sample PV was located 10 cm downstream from the opening side of the skimmer and 5 mm away from the center of the traversing droplet beam. The sample PV and the electron gun were operated at 14 Hz, while the droplet PV ran at half the frequency, and the difference image obtained when the droplet PV was on and off was the net image from the droplets, with or without dopant.

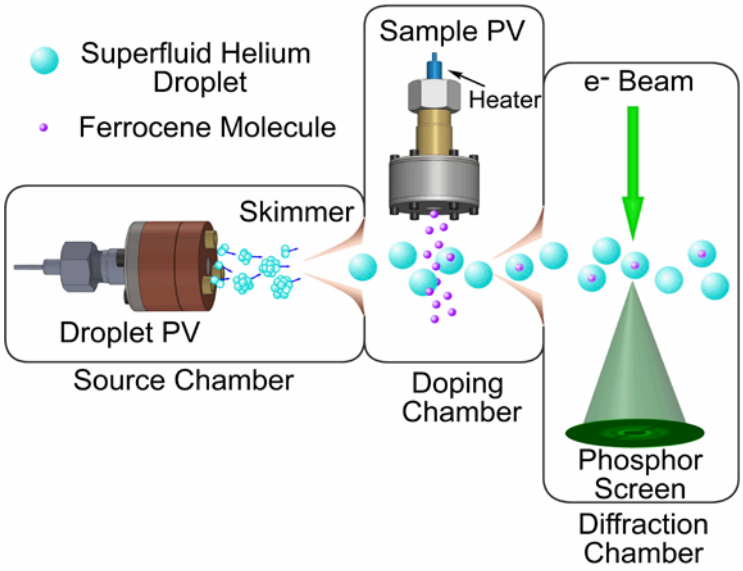

Fig. 7.1. Experimental setup showing the two pulsed valves, one for generation of superfluid helium droplets, and the other for release of gaseous ferrocene.

To obtain diffraction from only singly doped droplets, we relied on our knowledge of the characteristics of the droplet beam and the doping statistics.[13] Since the opening time of the droplet PV is much shorter than the traveling time to

the detection region, we can consider that all droplets are formed at the same time. Smaller droplets travel faster and arrive at the diffraction region earlier, and limited by their capacity to absorb the heat and momentum of a dopant molecule, they are also only capable of carrying just one dopant molecule into the diffraction region. On the other hand, if the doping process is sufficient, all droplets can be doped with at least one dopant molecule. Thus by timing the pulsed electron gun at the leading edge of the doped droplets, we can sample only singly doped small droplets. Furthermore, by delaying the electron gun to a later time, we can also select a certain sized droplet group with a certain sized dopant clusters.

To implement the above idea, several experimental conditions have to be fulfilled. Efficient doping requires sufficient doping pressure and path length. The extensive doping condition also causes diffusion of gaseous dopant molecules into the diffraction region, which requires background subtraction. To minimize diffusion and to limit the gas load in the doping chamber, pulsed delivery of dopant is therefore highly preferred. Consequently, the relative timing between the two pulsed valves becomes an important factor. A shorter delay results in a lower doping pressure when the droplet beam traverses the doping chamber, hence a limited percentage of droplets should be doped. Too long a delay also results in a missed time window for effective doping, since most dopant molecules should have been pumped out.

7.3 Results and analysis

The diffraction pattern from ferrocene doped droplets is a combination of diffractions from ferrocene molecules, the helium jacket outside the dopant molecule, undoped helium droplets, and background from the residual gas in the diffraction chamber. Typical gas phase experiments are expressed in terms of

modified molecular scattering intensity *sM(s)*, where *s* is the momentum transfer defined as:[1]

$$s = \frac{4\pi}{\lambda}\sin(\frac{\theta_d}{2}) \,, \qquad (7.1)$$

λ is the de Broglie wavelength (0.06 Å at 40 keV), and θ_d is the diffraction angle. Each unique pair of atoms (correlated pair) generates a set of rings for randomly oriented samples, and only the interference of correlated pairs contains the structure information of the sample. To magnify the structural information, in typical GED, the *sM(s)* profile removes all contributions from atoms and background, and the remaining molecular interference is further magnified by the momentum transfer *s:*

$$sM(s) = \frac{A_s \cdot I_{total}(s) - A_d \cdot I_{droplet}(s) - A_b \cdot I_{background}(s)}{I_{T,at}(s)} \cdot s - s \qquad (7.2)$$

where $I_{total}(s)$, $I_{droplet}(s)$, and $I_{background}(s)$ are intensities from the experiment of doped droplets, pure droplets, and background, A_s, A_d and A_b are the corresponding fitting parameters, $I_{T,at}(s)$ is the theoretical diffraction intensity from the atoms of the dopant molecule. The values of $I_{total}(s)$, $I_{droplet}(s)$, and $I_{background}(s)$ are from the experiment directly obtained from the diffraction image, and $I_{total}(s)$ and $I_{droplet}(s)$ are obtained under the same experimental conditions with the sample PV on and off respectively. The calculation method for $I_{T,at}(s)$ and for the theoretical values of the modified molecular scattering intensity *sM(s)* have been explained in the supplementary material of our previous publication.[11] Different from our previous work on CBr_4, the above equation does not include any contribution from dopant clusters.

The bottom panel of Fig.7.2 shows the radial distributions directly obtained from an image accumulated from 200,000 shots. The electron gun had a current of 1 mA and a duration of 10 μs, and its timing was set to sample droplets with about

2000 atoms/droplet.[13] We divided the raw image into four nearly equal quadrants, using the support of the Faraday cup – a strip on the image – as one of the dividing lines. The average of the four quadrants was used to generate the radial profile. The difference between the profiles from the doped sample and the pure droplet background shows a large modulation in the bottom panel of Fig. 7.2. Using these profiles as the intensities of Eq.7.2 and based on comparisons with the theoretical $sM(s)$,[15] we performed multilinear regression to obtain the coefficients of each component A_s, A_d and A_b. The left half of the image shown in Fig.7. 2 is the difference image after removing the contribution of pure droplets based on the obtained coefficients. The right side of the image is the theoretical calculation. The agreement between theory and experiment is quantitative, and the fitting has a coefficient of determination (R^2) of 0.92.

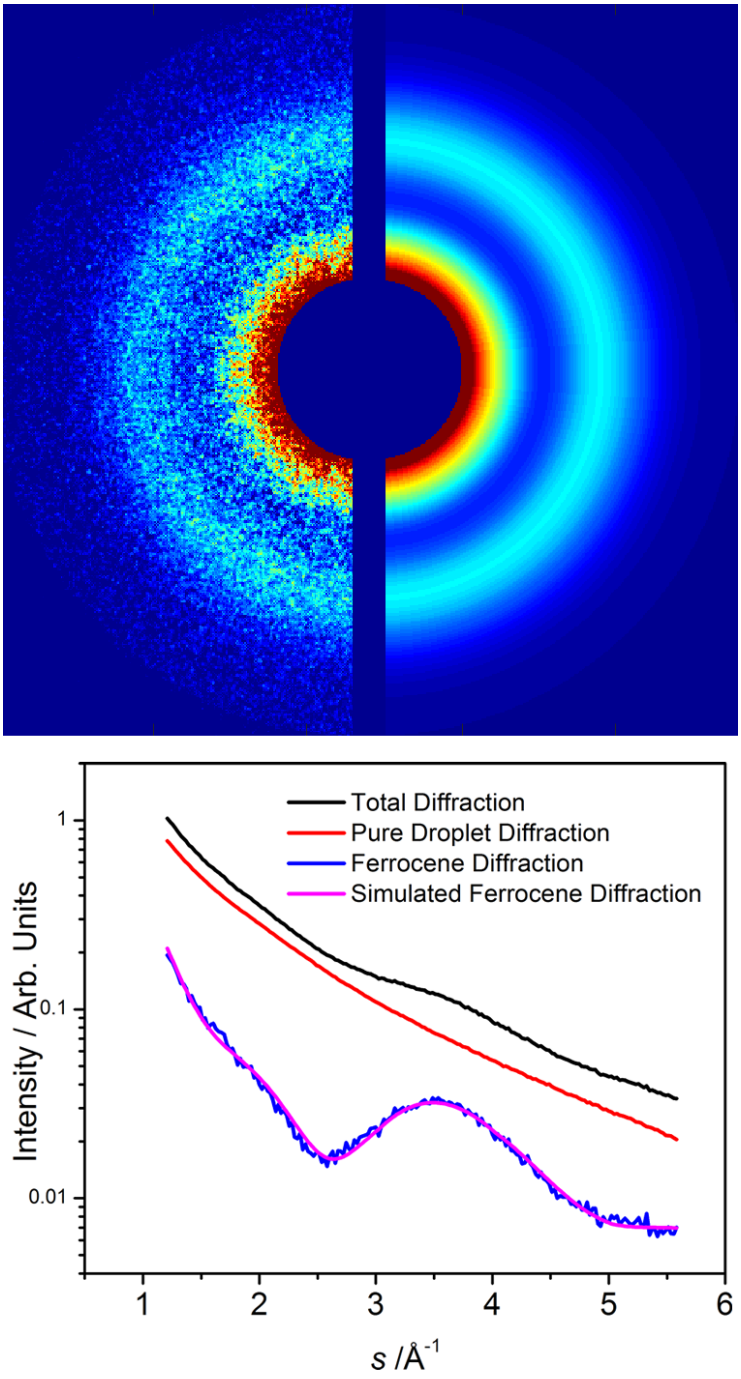

Fig. 7.2. Electron diffraction of ferrocene doped droplets. The left half of the image is the averaged experimental data after removing the contribution of helium, and right half is the simulation result based on the known molecule structure of ferrocene. The bottom panel is the radial profile from an accumulated image of 200,000 shots, with and without dopant, and the difference between the two profiles.

To analyze the doping condition, we performed the experiment under different delay times between the two pulsed valves. Table 7.1 shows the fitting results from images obtained under different time delays. For each delay, 70,000 to 100,000 images were accumulated, and the sample PV was kept at a duration of 280 μs. In all cases, the fitting parameter of the background A_b only accounts to less than 1% of the total diffraction signal A_s. At delay times between 1000 and 1200 μs, the number of helium atoms in the doped droplet beam is reduced to only 4% of their number in a pure droplet beam. The intensity ratio between ferrocene and helium in the overall diffraction signal of the doped droplets I_F/I_{He} can then be derived from

$$\frac{I_F}{I_{He}} = \frac{A_S \cdot I_{total}(s)}{A_d \cdot I_{droplet}(s)} - 1 \,, \tag{7.3}$$

since the contribution of the background is negligible. Although the values of the experimental diffraction intensities I_{total} and $I_{droplet}$ are dependent on the momentum transfer, their ratios only vary slowly in the range of 1.2 and 6 $Å^{-1}$, and an average value is listed in Table 7.1. We notice that the helium content is the same for the two central columns, but the intensity ratio is quite different. These two sets of data were recorded in two different days, with perhaps slight variations in the experimental conditions. It is therefore likely that a slightly different size or size distribution contributes to the marked difference, since the sampling method is critically dependent on small sized droplets.

Table 7.1 Fitting results at different delay times between the two pulsed valves

Delay (μs)	500	1000	1200	4000
A_d/A_s[a]	0.16	0.04	0.04	0.10
I_F/I_{He}[b]	0.11	0.26	0.49	0.20
n_{He}/n_F[c]	2400	1015	539	1320
Pressure[d] *(Torr)*	6.6×10^{-5}	1.1×10^{-4}	1.1×10^{-4}	8.1×10^{-5}
$P_1/(P_0+P_1)$[e]	0.72	0.81	0.81	0.76

[a] ratios of fitting parameters from Eq. (7.2).

[b] average ratios of intensities from ferrocene and from helium atoms in the doped droplet beam.

[c] estimated ratios of the numbers of helium atoms and ferrocene molecules in the doped droplet beam.

[d] equivalent doping pressures obtained from fitting the radial profile and Poisson statistics.

[e] fractions of singly doped droplets in the droplet beam.

To further obtain the number ratio of helium atoms vs. ferrocene molecules n_{He}/n_F, a ratio of the diffraction cross sections is required, which depends greatly on the *s* number. If we only take into consideration the atomic component of the diffraction cross section and ignore the modulation of molecular diffraction, the ratio of the total cross section is 264.[16] The numbers listed in Table 1 are therefore only qualitative. In theory, this number ratio should have a lower limit determined by the number of the remaining helium atoms after picking up one ferrocene molecule. From Table 7.1, at a shorter delay between the two PVs, there are more

than 2000 helium atoms for every ferrocene molecule, but as the delay increases, a higher pressure build-up is achieved, and the number of helium atoms decreases, mostly due to the increase in the number of doped droplets. At a much longer delay, the number of helium atoms increases again.

Due to the transient nature of the doping process, we could not measure the actual pressure in the doping region. However, based on the Poisson pickup statistics[17] and the fitting results A_d/A_s, we can determine the average number of effective collisions between ferrocene and droplets, assuming that trapping of one ferrocene molecule results in a droplet size change from 2000 to 800 (the average of the two middle columns in Table 7.1). For an ideal gas at 346 K over an estimated path length of 5 cm, we can then calculate the equivalent pressure for doping, and then the probability of picking zero (P_0) and one (P_1) ferrocene molecules. Further assuming that there are no droplets containing two or more ferrocene molecules in the diffraction region, we can then calculate the fraction of singly doped droplets. Table 7.1 shows that at delays of 1000 and 1200 μs, more than 80% of the droplets are singly doped.

The above results also imply that regardless of the doping pressure, as long as the contribution of helium atoms can be effectively removed according to Eq. (7.2), there is no essential difference between the resulting *sM(s)* profile. Hence the images obtained from the last three columns were added to improve the signal-to-noise ratio of the final result shown in Fig. 7.2. The data from the first column were not used because of its low ferrocene content. The excellent quality of the fitting procedure also confirms the hypothesis on the sampling condition: in all delay conditions, only singly doped droplets are sampled in the experiment, with no detectable contributions from ferrocene dimers.

Inverse Fourier transform of the modified molecular scattering intensity results in the pair correlation function, which peaks at the unique atomic pairs in the molecule. Fig. 7.3 shows the experimental and theoretical *sM(s)* profiles and the pair correlation functions obtained from Fig. 7.2 and from known molecular structures.[18] Contributions from hydrogen pairs are neglected because of their low intensity. The strongest contribution in the pair correlation profile is from the Fe-C pair, followed by intra-ring carbon pairs. The longer distance carbon pairs between different rings constitute the minor ring. It is worth noting that the contribution from C-H pairs constitute a shoulder in the profile, certainly not negligible at our level of signal-to-noise ratio.

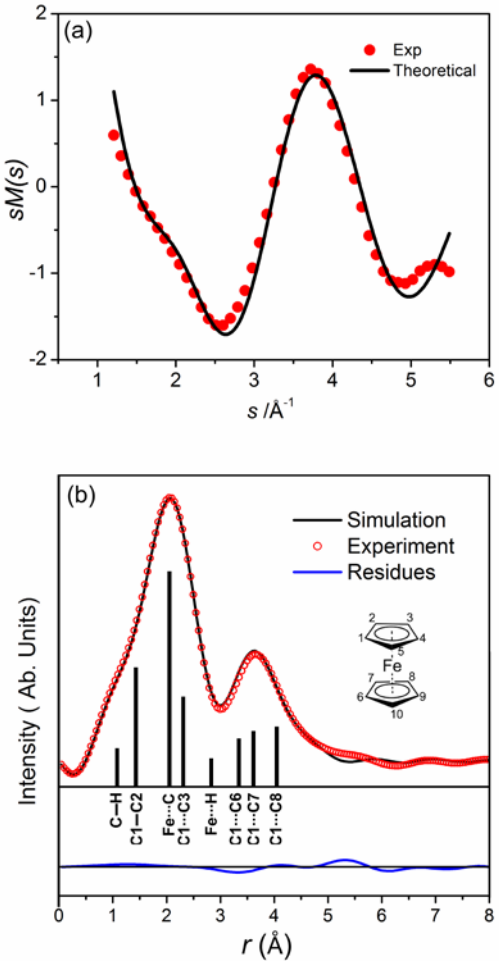

Fig. 7.3. Modified molecular scattering intensities (a) and Pair correlation profiles (b) of doped ferrocene. Contributions from relevant unique atomic pairs are

indicated as sticks, and the numbering scheme is shown in the inset. The residual between experiment and theory is also shown in the bottom of the profile.

Gas phase ferrocene is known to be in the eclipse conformation for the two pentacene rings.[15] Unfortunately, to resolve the relative conformation between the two rings, a larger range of momentum transfer is required. This is because the difference between the staggered and the eclipsed conformations is in the inter-ring C···C pairs, which has distances of 3.32, 3.62, 4.06 Å in the eclipsed form and 3.40, 3.87, 4.13 Å in the staggered form.[18] To resolve such a difference from the diffraction pattern, the range of *s* values needs to exceed 12 $Å^{-1}$.

This work demonstrates the feasibility of sampling only singly doped droplets. To extend the methodology to clusters of dopant molecules, a delay in the electron gun relative to the droplet PV is necessary so to sample larger droplets capable of picking up more dopant molecules. To further increase the flux for larger sized droplets, a concurrent decrease in the source temperature of the droplet beam should be beneficial. Unfortunately limited by the cooling capacity of our cryostat and the large heat capacity and linear momentum of ferrocene, experimental demonstrations of this idea using ferrocene are still challenging. However, in our previous work on CBr_4,[12] a molecule with a smaller heat capacity, even at the same time setting of the electron gun and under the same droplet conditions, we have observed significant contributions from dimers and trimers of CBr_4.

Several factors determine the degree of size selection via velocity slip,[13,19] including the heat capacity and the momentum of the dopant molecule, the binding energy of the dopant molecule and helium, the distance between the

droplet source and the detection region, the effective opening time of the pulsed valve, the average size and the size distribution of the droplet beam, and the duration of the electron gun. The current approach hence is not “one-size-fits-all”, and in many cases particularly for clusters containing several dopant molecules, statistical analysis and deconvolution procedures will be necessary.

In summary, we have achieved electron diffraction of singly doped superfluid helium droplets. The background issue from undoped droplets and excessively large droplets was resolved by sufficient doping of the droplet beam, and size selection was achieved by taking advantage of the velocity slip among different sized droplets. Exact timing of the electron beam and effective background subtraction were two of the key factors for the success of this experiment. This method can be extended to studies of dopant clusters, as demonstrated in our previous work on CBr_4 dimers and trimers, but the size resolution could be limited in some cases.

Acknowledgements

This work is supported by the National Institute of General Medical Sciences (1R01GM101392-01A1) from the National Institutes of Health and the Environmental Health Science Center at Oregon State University funded by the National Institute of Environmental Health Sciences (ES000210).

7.4 References

1 L. O. Brockway, Rev. Mod. Phys. **8**, 231 (1936).
2 J. Yang and M. Centurion, Struct. Chem. **26**, 1513 (2015).
3 D. Shorokhov and A. H. Zewail, Phys. Chem. Chem. Phys. **10**, 2879 (2008).
4 A. Boatwright, C. Feng, D. Spence, E. Latimer, C. Binns, A. M. Ellis, and S. Yang, Faraday Discuss. **162**, 113 (2013).
5 J. P. Toennies and A. F. Vilesov, Angew. Chem., Int. Ed. **43**, 2622 (2004).

[6] A. Volk, D. Knez, P. Thaler, A. W. Hauser, W. Grogger, F. Hofer, and W. E. Ernst, Phys. Chem. Chem. Phys. **17**, 24570 (2015).
[7] D. Spence, E. Latimer, W. York, A. Boatwright, C. Feng, S. Yang, and A. M. Ellis, Int. J. Mass Spectrom. **365-366**, 86 (2014).
[8] L. F. Gomez, K. R. Ferguson, J. P. Cryan, C. Bacellar, R. M. P. Tanyag, C. Jones, S. Schorb, D. Anielski, A. Belkacem, C. Bernando, R. Boll, J. Bozek, S. Carron, G. Chen, T. Delmas, L. Englert, S. W. Epp, B. Erk, L. Foucar, R. Hartmann, A. Hexemer, M. Huth, J. Kwok, S. R. Leone, J. H. S. Ma, F. R. N. C. Maia, E. Malmerberg, S. Marchesini, D. M. Neumark, B. Poon, J. Prell, D. Rolles, B. Rudek, A. Rudenko, M. Seifrid, K. R. Siefermann, F. P. Sturm, M. Swiggers, J. Ullrich, F. Weise, P. Zwart, C. Bostedt, O. Gessner, and A. F. Vilesov, Science (Washington, DC, U. S.) **345**, 906 (2014).
[9] L. F. Gomez, E. Loginov, and A. F. Vilesov, Phys. Rev. Lett. **108**, 155302 (2012).
[10] P. Thaler, A. Volk, F. Lackner, J. Steurer, D. Knez, W. Grogger, F. Hofer, and W. E. Ernst, Phys. Rev. B: Condens. Matter Mater. Phys. **90**, 155442 (2014).
[11] J. Zhang, Y. He, W. M. Freund, and W. Kong, J. Phys. Chem. Lett. **5**, 1801 (2014).
[12] Y. He, J. Zhang, and W. Kong, J. Chem. Phys. **145**, 034307 (2016).
[13] Y. He, J. Zhang, and W. Kong, J. Chem. Phys. **144**, 084302 (2016).
[14] Y. He, J. Zhang, Y. Li, W. M. Freund, and W. Kong, Rev. Sci. Instrum. **86**, 084102 (2015).
[15] R. K. Bohn and A. Haaland, J. Organomet. Chem. **5**, 470 (1966).
[16] A. Jablonski, F. Salvat, and C. J. Powell, *NIST electron elastic-scattering cross-section, Database, Version 3.2, SRD 64*. (National Institute of Standards and Technology, Gaithersburg, MD, 2010).
[17] M. Lewerenz, B. Schilling, and J. P. Toennies, J. Chem. Phys. **102**, 8191 (1995).
[18] S. Coriani, A. Haaland, T. Helgaker, and P. Jorgensen, ChemPhysChem **7**, 245 (2006).
[19] S. Yang and A. M. Ellis, Rev. Sci. Instrum. **79**, 016106 (2008).

Chapter 8 Self-Assembly of Iodine in Superfluid Helium Droplets: Halogen Bonds and Nanocrystals

Yunteng He, Jie Zhang, Lei Lei and Wei Kong*

Department of Chemistry, Oregon State University

Corvallis, OR 97331, USA

Angewandte Chemie International Edition

Postfach 10 11 61

69451 Weinheim Germany

2017, 56, 3541 –3545

---

*Corresponding author, 541-737-6714, wei.kong@oregonstate.edu

Abstract: We present evidence of halogen bond in iodine clusters formed in superfluid helium droplets based on results from electron diffraction. Iodine crystals are known to form layered structures with intralayer halogen bonds, with interatomic distances shorter than the sum of the van der Waals radii of the two neighboring atoms. The diffraction profile of dimer dominated clusters embedded in helium droplets reveals an interatomic distance of 3.65 Å, much closer to the value of 3.5 Å in iodine crystals than to the van der Waals distance of 4.3 Å. The profile from larger iodine clusters deviates from a single layer structure; instead, a bi-layer structure qualitatively fits the experimental data. This work highlights the possibility of small halogen bonded iodine clusters, albeit in a perhaps limited environment of superfluid helium droplets. The role of superfluid helium in guiding the trapped molecules into local potential minima awaits further investigation.

8.1 Introduction

Intermolecular forces significantly affect the physical and chemical properties of molecular systems. Hydrogen bonding, dipole-dipole interactions, ion-dipole interactions, and van der Waals forces are thus the bases for chemical reactivity, catalysis, and biomolecular structures and functions. Recently, a relatively new type of intermolecular forces, the halogen bond (XB), has been observed in many different contexts.[1] Halogen atoms are found to act as not only electron density donors toward electron-deficient partners such as protons or metal cations, but also electron density acceptors in the vicinity of electron donors such as anions or other halogen atoms. In general, halogen bonds are depicted as Y – X⋯D, where the three dots represent the bond, X is the electrophilic halogen atom (Lewis acid), D is an electron density donor (Lewis base), and Y is typically a carbon, nitrogen, or another halogen atom. The existence of XB is signified by a shorter intermolecular distance than the van der Waals distance. In recent years, XB has evolved from a scientific curiosity to practical applications in design and manipulation of aggregation processes.[2,3]

Although in the biological field, XB is typically discussed when Y is a heteroatom, the definition from the International Union of Pure and Applied Chemistry has also included another category of XB where Y = X.[4] This latter type is related to the crystalline structure of halogens. For example, the crystalline state of iodine is layered with both molecular and semiconducting characters.[5] The intermolecular distance within the layer is 3.5 Å, much shorter than the van der Waals distance of 4.3 Å, while in between layers, the distance is 4.3 Å. Iodine crystals are thus a quintessential representation of homo-halogen bonds.

The halogen bond in crystalline iodine raises a question about the criterion of its formation: does XB exist in dimers or trimers, or does it only form in bulk crystals? Rich literature exists for iodine cluster anions and polyiodide anions,[6] but there is paucity in studies of small neutral iodine clusters. Passchier and Gregory reported evidence of molecular dimers of iodine in the vapor phase, and the authors proposed a pair separation of 5.5 Å,[7] even longer than twice the van der Waals radius. Raman spectroscopy offered evidence of small $(I_2)_n$ clusters in rare gas matrices and in liquid iodine, however, no geometric information was reported.[8] Recently, Hulkko et al. reported a sheet-like planar structure for $(I_2)_n$ (n = 2 - 7) in a solid krypton matrix.[9] Based on Raman spectroscopy, the authors assigned purely van der Waals bonding between iodine molecules in the cluster and suggested that all iodine molecules reside in the same plane. It is fair to say that so far the existence of halogen bonds in small neutral $(I_2)_n$ is still an open question.

Superfluid helium droplets have recently been recognized as an interesting medium for nucleation events.[10] The low temperature (0.37 K) and the rapid cooling rate of a droplet can lead to formation of unusual clusters.[11-15] For example, alkali metal atoms are known to reside on the surface of helium droplets, and alkali dimers are observed to exist only in triplet states on the surface.[11,16] Only sufficiently large alkali clusters can switch from a surface location to an interior location.[17] Magnesium foams have been observed to form within helium droplets, and these metastable foams appear to collapse into compact clusters after a weak excitation.[14] For molecular clusters, Nauta and Miller first experimented with $(HCN)_n$ (n = 2 – 7) clusters and confirmed the long chain structure of the clusters using vibrational spectroscopy.[12] Although

thermodynamically, a more compact structure is more stable for a finite cluster, long chains are the structural motif of crystalline HCN. Subsequently, Slipchenko et al. have investigated $(NH_3)_n$ ($n = 2 - 10^4$), and the authors have also concluded that the ammonia clusters form a crystalline structure in helium droplets.[13] This common phenomenon of small clusters forgoing their own global minimum and adopting the global minimum of crystalline bulk has been attributed to the rapid cooling rate in superfluid helium droplets and the long-range dipole–dipole force between the dopant molecules.

Size-dependent evolution of cluster structures has been the subject of basic and applied research, and structure determination is one of the critical challenges of cluster science. Spectroscopy has long been hailed as a powerful tool, but interpretation of spectroscopic signatures relies on the precision of theoretical calculations. Alternatively, gas phase electron diffraction (GED) has enjoyed a long history of success for more than half a century.[18] Recently, the technique has been adapted for time domain studies of reaction intermediates and transient processes.[19-21] Maier-Borst et al. has coupled a Paul ion trap with an electron diffraction apparatus for studies of ionic clusters.[22] Data from GED is the Fourier transform of the charge distribution of a molecule, and reverse Fourier transform reveals interatomic distances corresponding to all unique pairings of atoms in a molecule. By comparing features between experimental and simulated profiles, and by iterative refinement of the simulation model, cluster structures can be determined with confidence.

Our group has constructed an electron diffraction apparatus for structure determination of molecules and clusters doped in superfluid helium droplets.[23-25] Here

we report results of size-selected I_2 clusters in helium droplets, achieved by taking advantage of the velocity slip in our pulsed droplet beam.[26,27] We demonstrate the existence of halogen bonds in two different groups of iodine clusters. The diffraction image from the smaller sized clusters alludes to a predominantly dimeric cluster with an intermolecular distance of 3.65 Å, much shorter than the van der Waals distance. The diffraction profile of the larger clusters deviates from that of a single sheet, implying a multilayer structure. Although the agreement between experiment and simulation is still imperfect, the basic conclusion on the formation of a multilayer iodine nanocrystal inside superfluid helium droplets is indisputable.

8.2 Experimental setup

The overall setup has been described in our previous publications.[24,25] Superfluid helium droplets were formed by supersonic expansion of precooled ultrapure helium (99.9995%) from an Even-Lavie pulsed valve (referred to as the droplet PV in the following). The droplet beam was further collimated by a skimmer with an orifice of 2 mm in diameter about 11 cm downstream from the droplet PV. In the doping chamber, another pulsed valve (Parker, series 9, referred to as the sample PV) with a homemade nozzle housed the I_2 solid at room temperature. It was sufficient to produce a stable doping pressure without heating the sample PV. The sample PV and the electron gun were operated at 10 Hz, while the droplet PV ran at half the frequency, and the difference image obtained when the droplet PV was on and off is the net image from doped and pure droplets.

8.3 Results and analysis

Typical gas phase electron diffraction data are expressed in terms of modified molecular scattering intensity *sM(s)*, where *s* is the momentum transfer defined as[18]:

$$s = \frac{4\pi}{\lambda} sin\left(\frac{\theta_d}{2}\right), \quad (8.1)$$

Where λ is the de Broglie wavelength (0.06 Å at 40 keV), and θ_d is the diffraction angle. Each unique pair of atoms (correlated pair) generates a set of rings for randomly oriented samples, and only the interference of correlated pairs contains the structure information of the sample. To magnify the structural information, in typical GED, the *sM(s)* profile removes all contributions from atoms and background, and the remaining molecular interference is further magnified by the momentum transfer *s*:

$$sM(s) = \frac{A_s \cdot I_{total}(s) - A_d \cdot I_{droplet}(s) - A_b \cdot I_{background}(s)}{I_{T,at}(s)} \cdot s - s \quad (8.2)$$

where $I_{total}(s)$, $I_{droplet}(s)$, and $I_{background}(s)$ are intensities from the experiment of doped droplets, pure droplets, and background, A_s, A_d and A_b are the corresponding fitting parameters, $I_{T,at}(s)$ is the theoretical diffraction intensity from the atoms of the dopant molecule. The values of $I_{total}(s)$, $I_{droplet}(s)$, and $I_{background}(s)$ are from the experiment directly obtained from the diffraction image, and $I_{total}(s)$ and $I_{droplet}(s)$ are obtained under the same experimental conditions with and without the sample. The calculation method for $I_{T,at}(s)$ and for the theoretical values of the modified molecular scattering intensity *sM(s)* have been explained in the supplementary material of our previous publication.[23]

Fig. 8.1 shows the *sM(s)* profiles recorded under two different experimental conditions: the top panel was obtained under a lower effective doping pressure and by sampling the leading edge of the droplet beam, while the bottom panel was obtained under opposite conditions. The experimental radial profiles (red dots) in the two panels are quite different, indicating very different structures sampled under the two different experimental conditions.

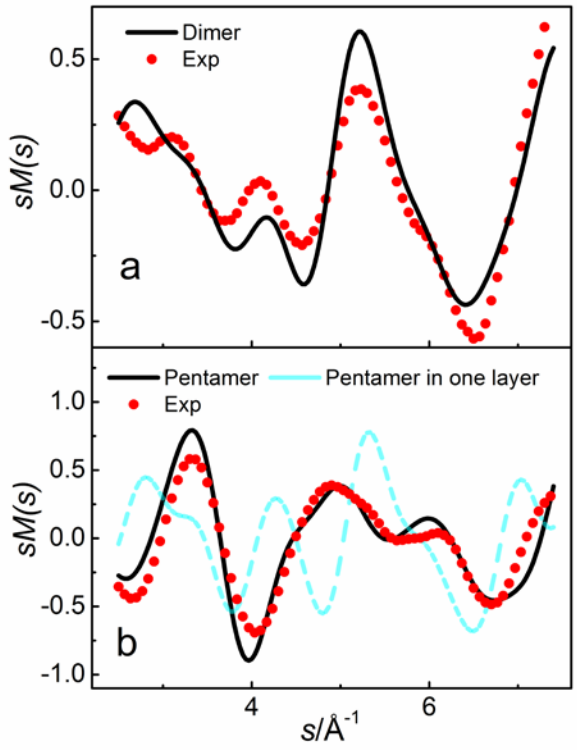

Fig. 8.1. Modified molecular scattering intensities of smaller iodine clusters (a) and larger iodine clusters (b). The solid black lines are calculated profiles based on proposed structures.

We believe that the upper panel should correspond to diffraction from smaller sized iodine clusters. Upon comparison with the theoretical *sM(s)* of I_2 monomer, shown in the supplementary material, we can confidently eliminate the possibility of only monomers and consider diffraction from iodine clusters or mixtures of monomers and clusters. Based on the timing of the electron gun and the size distribution of the droplet beam, we are confident that the general size of the sampled droplets should be smaller than 1500 atoms/droplet.[25,27] In general, pickup of one iodine molecule requires removal of 400 – 600 helium atoms for cooling, and to ensure that the doped droplets continue to travel into the diffraction region, at least 500 helium atoms need to remain with the droplet after doping.[27,28] Taking these numbers into consideration, the sampled iodine cluster in the top panel of Fig. 1 should contain no more than three iodine molecules. We calculated the theoretical *sM(s)* of iodine dimers by fixing the intramolecular bond length at 2.67 Å. Visual inspections of the diffraction profiles of a few possible structures of the dimer, including the “T” shape, the “L” shape, and the parallel configurations, lead to the conclusion of a possible “L” shape structure. We then manually varied the relative distance and angle between the two iodine molecules, compared the resulting diffraction profiles with the experiment, and relied on the fitting result of multi-linear regressions of the diffraction profiles from Eq. 8.2. The continuous black trace is the best fit, with an adjusted intermolecular distance of 3.65 Å between the two nearest iodine atoms. Due to the shadow of the Faraday cup, we paid limited attention to the region below 3 $Å^{-1}$ to avoid possible contamination. The calculation is not a perfect reproduction of the experimental result, but it has sufficient merit in reproducing the general trend. We have also calculated the *sM(s)*

profiles of trimers based on several possible structures, a one-layer structure from several different cuts of crystalline iodine, and a bi-layer structure with a dimer and a 3rd molecule in a different plane. As provided in the supplementary material, none of the profiles can be considered qualitatively acceptable. We therefore conclude that the diffraction profile is predominantly due to iodine dimers.

The lower panel in Fig. 8.1 should correspond to diffraction from larger sized iodine clusters, such as tetramers, pentamers or even hexamers. To identify the structures of these clusters, we first consider the situation of pentamers. We tried to place all five iodine molecules in one layer according to the crystalline structure[5] (light-blue dashed line), and the result is qualitatively unacceptable. Realizing that the most salient feature in the diffraction profile centered at 3.5 Å^{-1}, corresponding to a distance of ~4.3 Å, we then considered pseudo-double layer structures with two iodine molecules in each plane and the fifth adjustable out of either plane. We cut fragments from an iodine single crystal, calculated the diffraction profiles, and compared with the experimental result. The best result from this adjustment is shown by the black line. We can confidently state that the larger iodine clusters sampled in the bottom panel does NOT belong to any single layer structure. Instead, a bi-layer structure must have been formed.

Unlike the case of the smaller clusters, the calculated *sM(s)* profiles for tetramers, pentamers, and hexamers are all similar (see supplementary material), as long as the iodine molecules form bi-layer structures. The pairings from atoms on the outer edges of each cluster do not have repeats, hence their contribution in the overall diffraction profile is overshadowed by those that have many repeats, such as the interlayer

distances between corresponding atoms. The diffraction technique is hence insensitive to the actual size of the iodine cluster under the current conditions. In the following discussion, we choose pentamer as a representation of this cluster group, partly because we have the best success in reproducing the experimental diffraction profile with one particular pentamer structure. We do acknowledge that the experimental data could well be a mixture of clusters with sizes from tetramer to hexamer but with similar structural motifs.

Reverse Fourier transform of the *sM(s)* profile reveals all the unique pairings of the sample. Fig. 8.2 shows the pair correlation functions of the two diffraction profiles obtained from Fig. 8.1. The limited range of *s* values from our image detector requires a large damping factor in the calculation, which not only broadens the profile but also introduces extraneous oscillations in large distances. The estimated uncertainty in the resulting distance is on the order of 0.1 Å. The inset of each panel shows our proposed structures and the numbering schemes. To avoid clumsiness in labeling, all intramolecular distances between the two covalently bonded iodine atoms are labeled "Intra", while only a few intermolecular distances are labeled. The shaded region represents intermolecular pairs such as 3⋯8, 4⋯9 and 5⋯10.

For the case of dimer dominated diffraction, each unique interatomic distance can be more or less resolved under the current conditions, although the fitting is still imperfect. The proposed structure has a distance of 3.65 Å between atoms 1 and 3, and this value is substantially shorter than the sum of the van der Waals distances of two iodine atoms (4.3 Å), but are similar to the in-plane intermolecular distance of 3.5 Å in crystalline iodine.[5] Moreover, all four iodine atoms are in the same plane in

the proposed dimer structure. This result unambiguously confirms the halogen bond between the two iodine molecules.

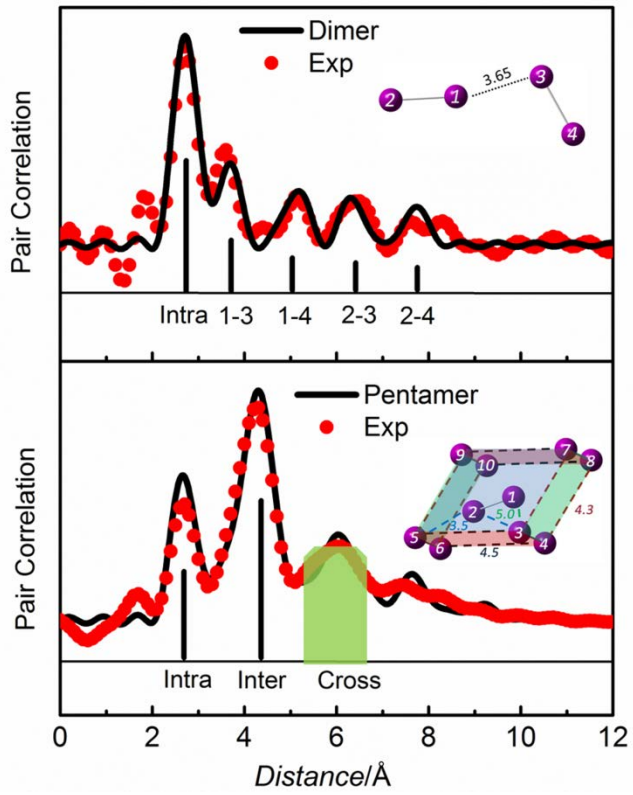

Fig. 8.2. Pair correlation profiles of doped iodine clusters and their proposed structures. The insets show the structures of the clusters and the numbering of the atoms.

For the larger clusters, our experiment is incapable of resolving several unique intermolecular distances, but a few features are still identifiable. The intramolecular distance at 2.67 Å, which has five repeats, is clearly resolved. The next longer distances are the halogen bonds between atoms 2 ⋯ 3 and 2 ⋯ 5 at ~3.5 Å and the van der Waals bonds between atoms 3 ⋯ 6 and 7 ⋯ 10 at 3.85 Å. These distances

have only two repeats each, and hence they contribute to the leading edge of the peak labeled “Inter”. Three major contributions constitute the major feature of the pair correlation profile: the interlayer distance between 2 ⋯ 9, 3 ⋯ 9, and 4 ⋯ 10 at ~4.1 Å has three repeats, the interlayer distance between 3 ⋯ 7 and 4 ⋯ 7 at 4.3 Å has in total seven repeats, and the intralayer distance between 3 ⋯ 5 at 4.5 Å has four repeats. The resulting center of the convoluted peak is therefore at 4.3 Å. Other interlayer and intralayer distances involving atoms across the longer diagonals of the parallelepipeds are in the range longer than 5.6 Å and have fewer repeats, hence they are clustered together in the shaded region.

The current pentamer structure contains two halogen bonds between atoms 2⋯3 and 2⋯5 at ~3.5 Å, while other distances of the parallelepiped of atoms 3⋯5 and 3⋯7 are van der Waals in nature. Attempts to rearrange the 1 – 2 atoms into a more symmetric position stapling the two layers failed to match the current fitting result. The distances of 1⋯3, 1⋯5 and 1⋯9 range from 5.0 to 6.0 Å: these values are less than one Angstrom longer than the intralayer van der Waals distance of 3⋯5 at 4.5 Å. Perhaps the availability of two halogen bonds in the current structure prevails over the more symmetric structure, which offers fewer possibilities of halogen bonds.

Our results demonstrate clear evidence of halogen bonds in iodine dimers formed in superfluid helium droplets. In a near “L” shaped structure, overlapping between the *p* orbitals of the two non-covalently bonded iodine atoms is optimized.[29] In light of the reports on hydrogen bonded molecular clusters in superfluid helium droplets,[12,13] this result is not too surprising. Theoretical efforts in understanding the driving force between the two iodine molecules are daunting, while further calculations on the

interaction between molecular iodine and superfluid helium are even more difficult. We currently are in the process of developing a comprehensive fitting procedure to systematically optimize the atomic structure from a diffraction image. Together with more detailed theoretical calculations, we hope to further elucidate the role of halogen bonds in iodine clusters.

An interesting result is the structure of the larger clusters where instead of a single layer, a bi-layer structure seems to dominate when more than three iodine molecules are present. It is possible that different from bulk crystals, small clusters are more stable in a bi-layer structure, particularly in a superfluid helium environment. Alternatively, the missing one-layer structure might be related to the limited size range sampled by the electron beam. Formation of halogen bonds should be associated with large energy releases, and the formation of a single layer pentamer requires evaporation of many more helium atoms than the formation of a bi-layer cluster. It is possible that within the size range of the droplet beam sampled by the electron gun, only bi-layer structures can survive the evaporative cooling process and maintain the traveling momentum to the diffraction region.[27] Unfortunately, given the insensitivity of the diffraction technique, further experimental confirmation of this speculation is difficult if possible at all.

The present results demonstrate the formation of iodine clusters in superfluid helium droplets. The near-covalent nature is demonstrated in the short intermolecular distance between the two I_2 molecules. For larger clusters, interlayer bonding is van der Waals in nature, while evidence of some intralayer halogen bonding is also present. Electron diffraction of molecules and clusters doped in superfluid helium

droplets is proven a direct structure tool, and in combination with velocity slip, size selective electron diffraction is experimentally feasible.

Acknowledgement

This work is supported by the National Institute of General Medical Sciences (1R01GM101392-01A1) from the National Institutes of Health.

8.4 References

1 G. Cavallo, P. Metrangolo, R. Milani, T. Pilati, A. Priimagi, G. Resnati, and G. Terraneo, Chem. Rev. **116**, 2478 (2016).
2 Q.-N. Zheng, X.-H. Liu, T. Chen, H.-J. Yan, T. Cook, D. Wang, P. J. Stang, and L.-J. Wan, J. Am. Chem.Soc. **137**, 6128 (2015).
3 P. Metrangolo, F. Meyer, T. Pilati, G. Resnati, and G. Terraneo, Angew.Chem. Int. Ed. **47**, 6114 (2008).
4 G. R. H. Desiraju, P. S.; Kloo, L.; Legon, A. C.; Marquardt, R.;Metrangolo, P.; Politzer, P.; Resnati, G.; Rissanen, K. , Pure Appl. Chem. **85**, 1711 (2013).
5 F. van Bolhuis, P. B. Koster, and T. Migchelsen, Acta Cryst. **23**, 90 (1967).
6 P. H. Svensson and L. Kloo, Chem. Rev. **103**, 1649 (2003).
7 A. A. Passchier and N. W. Gregory, J. Phys. Chem. **72**, 2697 (1968).
8 R. J. Magaa and J. S. Lannin, Phys. Rev. B **32**, 3819 (1985).
9 E. Hulkko, T. Kiljunen, T. Kiviniemi, and M. Pettersson, J. Am. Chem.Soc. **131**, 1050 (2009).
10 S. Yang and A. M. Ellis, Chem. Soc. Rev. **42**, 472 (2013).
11 F. Stienkemeier, J. Higgins, C. Callegari, S. I. Kanorsky, W. E. Ernst, and G. Scoles, Z. Phys. D: At., Mol. Clusters **38**, 253 (1996).
12 K. Nauta and R. E. Miller, Science **283**, 1895 (1999).
13 M. N. Slipchenko, B. G. Sartakov, and A. F. Vilesov, J. Chem. Phys. **128**, 134509 (2008).
14 A. Przystawik, S. Goede, T. Doeppner, J. Tiggesbaeumker, and K.-H. Meiwes-Broer, Phys. Rev. A: At., Mol., Opt. Phys. **78**, 021202 (2008).
15 J. P. Toennies and A. F. Vilesov, Angew. Chem., Int. Ed. **43**, 2622 (2004).
16 J. Higgins, C. Callegari, J. Reho, F. Stienkemeier, W. E. Ernst, M. Gutowski, and G. Scoles, J. Phys. Chem. A **102**, 4952 (1998).
17 J. Tiggesbaeumker and F. Stienkemeier, Phys. Chem. Chem. Phys. **9**, 4748 (2007).
18 L. O. Brockway, Rev. Mod. Phys. **8**, 231 (1936).
19 A. H. Zewail, Annu. Rev. Phys. Chem. **57**, 65 (2006).
20 M. Centurion, P. Reckenthaeler, F. Krausz, and E. Fill, J. Mol. Struct. **978**, 141 (2010).
21 C. J. Hensley, J. Yang, and M. Centurion, Phys. Rev. Lett. **109**, 133202 (2012).

[22] M. Maier-Borst, D. B. Cameron, M. Rokni, and J. H. Parks, Phys. Rev. A: At., Mol., Opt. Phys. **59**, R3162 (1999).
[23] J. Zhang, Y. He, W. M. Freund, and W. Kong, J. Phys. Chem. Lett. **5**, 1801 (2014).
[24] J. Zhang, Y. He, and W. Kong, J. Chem. Phys. **144**, 221101 (2016).
[25] Y. He, J. Zhang, and W. Kong, J. Chem. Phys. **145**, 034307 (2016).
[26] Y. He, J. Zhang, Y. Li, W. M. Freund, and W. Kong, Rev. Sci. Instrum. **86**, 084102 (2015).
[27] Y. He, J. Zhang, and W. Kong, J. Chem. Phys. **144**, 084302 (2016).
[28] M. Lewerenz, B. Schilling, and J. P. Toennies, J. Chem. Phys. **102**, 8191 (1995).
[29] C. H. Townes and B. P. Dailey, J. Chem. Phys. **20**, 35 (1952).

Chapter 9 Conclusion

This thesis work is focused on the diffraction component of our ss-EDI project. We are the first group to demonstrate electron diffraction of molecules embedded in superfluid helium droplets, and to address the issue of the helium background in diffraction. For the first time, we demonstrate the feasibility of obtaining diffraction information from species and even their complexes embedded in superfluid helium droplets. These experiments have also offered us a chance to develop a data processing protocol to remove background noise and background signal from helium.

Over the course of this work, we have overcome barriers including the technical details in electron diffraction and sample doping in superfluid helium droplets. Two major actions were taken: (1) the electron beam was improved by mounting a second electromagnetic lens under exit of the electron gun, to produce a more collimated and higher flux electron beam; (2) two facile time of flight components (EI-TOF and MPI-TOF) were installed to systematically characterize the timing profile, size distribution, and doping mechanism of the pulsed helium droplet beam.

The success in improving the behavior of our electron beam and in understanding the behavior of the pulsed droplet beam have enabled us to achieve electron diffraction of neutral molecules doped in helium droplets. In the experiment of ferrocene, by taking advantage of the velocity slip of our pulsed droplet beam, smaller droplets at the front of the droplet beam are heavily doped and selectively detected, and more than 80% of the droplets contain exactly one ferrocene molecule. In the work on CBr_4, the

possibility of doping more than one molecule in a single droplet has been explored. Further experiments using iodine as dopants have revealed the formation of different sized iodine clusters. The diffraction patterns from different sized iodine clusters offer conclusive evidence of halogen bonds in iodine dimers and bi-layer structure of larger iodine clusters.

The success of this thesis work marks a major step forward in making ss-EDI a reality. However, the remaining tasks are equally as daunting: an alignment laser will be introduced during diffraction of ions from an electrospray ionization source. Prior to integrating the two separate “halves” of the apparatus into the ultimate machine, further improvements and control of ion doped droplets are necessary, and demonstrations of the molecular goniometer using ions or neutral molecules are also preferred. The final success of the project will depend on the efforts of future generations of students.